PhD Thesis

Self Interacting Fuzzy Dark Matter and its Observational Implications

submitted in fulfilment of the requirements for the Degree of

Doctor of Philosophy

Milos Indjin

School of Mathematics, Statistics & Physics,

Faculty of Science, Agriculture & Engineering

Newcastle University

Newcastle upon Tyne, United Kingdom

September 2024

Acknowledgements

First and foremost, I would like to thank my supervisors: Dr Gerasimos Rigopoulos, who presented me with the initial opportunity and encouragement to pursue a PhD. He provided me with optimism during the hardest of moments and inspired passion within me for the elegance in mathematics; Professor Nikolaos Proukakis, for teaching me to appreciate and enjoy the finer technical details while still maintaining a dedicated focus to the bigger picture, and for showing that the simplest questions are often the hardest and most important; Dr I-Kang Liu, for fostering my now enormous appreciation for numerics, and for the countless hours of support, regularly into the late hours of the night. To all of you, I have enjoyed every single moment of our fruitful discussions together, and given the chance, I would not change a second; I would only add them.

I extend my deepest gratitude to my parents, Dragan and Sladjana, for their never-ending support in all aspects one could possibly imagine - and more. Without them, none of this would have been possible, and I will forever be grateful to them for the passion and drive they have instilled in me. I also thank my late grandmother, Stanica, for her support and belief in me. I regret that she could not witness my completion of this journey. To my uncle, Ivica, I give my thanks for his interest in my work, and many hours of productive discussion on topics tangentially related to my research. I also thank my uncle, Dragan Bakić, for demonstrating both what true passion towards one's field is, and inspiring me with his exemplary work ethic. To my uncle, Dragan Sarić, I am grateful for the pragmatism he provided, and for supporting my goals in and out of my studies.

I thank my girlfriend, Tara, for her unwavering support and ability to instill a newfound confidence in me during challenging times.

My thanks to all my friends, in all the cities and countries they are found in, for the countless hours of carefree fun, for which we find all too little time for these days. I must thank the friend who has been at my side from the beginning of my journey as an undergraduate, Connor, with whom I have shared long conversations about my research, and who has always been my steadfast supporter. I thank Jack, with whom I lead many discussions on the navigation of postgraduate study, for the gentle guidance he has provided from a different perspective.

To my loving and ever supportive parents,
Dragan & Sladjana

Contents

List of Figures

List of Tables

Abstract

We investigate aspects of Fuzzy Dark Matter (FDM) in both the non-interacting and repulsively self-interacting regimes, critically discussing the role of interactions on virialised profiles, using our findings to fit to galactic rotation curves of a range of dark matter dominated galaxies, thus proposing a way to numerically reconstruct a galaxy from analysing observational curves. Specifically, we firstly analyse the ground state solution of the Gross-Pitaevskii-Poisson equations - the soliton core. A generalised ansatz is formed along with a soliton-specific dimensionless interaction strength. The virial theorem is utilised to explain core dependencies on boson (m) and total mass, and self-interaction (g), and a degeneracy in the pairing of m and g is also uncovered. Moreover, we introduce a Super-Gaussian profile from empirically fitting to numerically generated self-interacting soliton ground states. This profile, joined with a Navarro-Frenk-White (NFW) halo profile, is used to fit self-interacting FDM to observational data of dark matter dominated galaxies, finding the crucial result that a single m and g pair fits all selected galaxies. Thirdly, we present three dimensional (3D) simulation results of self-interacting FDM, and we demonstrate a scheme which allows us to reconstruct density profiles whose inferred rotation curves replicate observational data. In particular, we present a simulated self-interacting FDM halo corresponding to a galaxy for which we have observational data, specifically galaxy UGCA444. We find an elegant form of the core-halo mass relation, depending on the total energy of the system and qualitatively comment on the variation in granule number and size depending on total energy. Next, we analyse the dynamical aspects of the halo. In particular we (i) investigate the effects of m and g on the oscillation frequency of soliton cores; (ii) reveal evidence for a cooling (condensation) process, where the core density grows on time scales longer than the age of the universe; (iii) finally, we undertake a preliminary investigation of the orbital dynamics of test particles in our recreated galaxy, commenting on the velocity dispersion and the implications for the age gradient of stars in disc galaxies.

1

Historical Background and Thesis Overview

1.1 Historical Introduction

In the early to mid 20^{th} century, E. Hubble and M. Humason [4] discovered a large and unexpected dispersion in the velocities of galaxies in their observational data of the Coma cluster. Though this is now considered a groundbreaking discovery, which has since redefined astronomy and cosmology as well as our fundamental understanding of the universe, the initial reaction of the scientific community was one of measured intrigue. It was not until a subsequent deeper analysis by F. Zwicky [5] that the profound nature of the discovery was revealed. By applying the virial theorem [6] to the data obtained by Hubble & Humason, Zwicky derived an estimate for the total mass of the cluster which starkly contrasted theoretical predictions based on observations of the visible matter. This was later followed by multiple analyses of galactic rotation curves [7, 8, 9], which was found to be in tension with theoretical predictions based on assumptions that all matter was visible and baryonic. In the aforementioned literature, astronomers found that rather than demonstrating a gradual drop in velocity with increasing radius, the rotation curves of galaxies were largely flat at larger radii, explicitly suggesting a gap in understanding of either fundamental gravity on large scales, or of the matter from which these galaxies are composed. It is clear to us in hindsight that these two problems are inextricably linked, nevertheless they were studied largely independently at the time. It eventually

became clear that both problems are clearly remedied by an introduction of a 'dark' component of matter that is only coupled to baryonic matter via the gravitational force. In search of this, many academics turned to new solutions outside of the standard model of particle physics to explain the missing mass, and this search continues to be a hot topic to this day.

Supersymmetry predicts a stable, weakly interacting massive particle (WIMP) which would be a strong candidate for dark matter[10], however with the Large Hadron Collider's hitherto failure to demonstrate the existence of supersymmetry, this specific avenue has suffered reduced interest. Neutrinos are considered possible candidates of hot dark matter (HDM)[11] due to their interaction only via gravity and the weak force. Many further approaches and suggestions have been put forth to describe what dark matter (DM) could consist of, however nothing has yet been set in stone. The current leading theory is the cold dark matter (CDM) model[12, 13, 14, 15]. The essence of this theory is that DM does not have a notable random velocity dispersion around the background velocity of the gravitationally bound construct it is found in. The time line of the large scale structure under the CDM paradigm consists of primary collapse of small scale structures which then further merge to form the large scale structure of the universe we see today. This structure formation is labelled a 'hierarchical' formation and differs from the HDM in chronology. In fact, in HDM, large scale structures form via fragmentation from larger gravitationally bound objects into the filaments and clusters visible in the present sky. HDM, unfortunately, fails to explain the smaller scale structure formation in the universe - this requires some variation of CDM or warm dark matter (WDM), a mixture of the two. Despite being the leading theory, CDM still comes with crucial shortcomings at these smaller scales [16, 17, 18], most notable of which are:

- **the cusp-core problem**, originating from the discrepancy between predicted CDM density profiles of smaller galaxies [19], in which the density is a function of radius and rises sharply towards the center of the core, and the implied flat density profile from observational rotation curves which implies a soliton core.

- **the missing satellite problem**, which stems from the abundance of smaller DM haloes that form around larger concentrations of mass within N-body CDM simulations. These prove inconsistent with the number of dwarf galaxies orbiting larger galaxies, such as the Milky Way.

The halo of CDM is typically modelled using the Navarro-Frenk-White (NFW) profile [20], which exhibits an r^{-3} drop in density at outer regions which recreates the flat portion of the velocity curve. However, as mentioned, this profile has a continuous rise in density as $r \to 0$. The reflection of this in the computed velocity profiles is seen in FIG. 1.1. Here, the NFW profile is never able to achieve the necessary linear growth in velocity consequent of a flat inner core

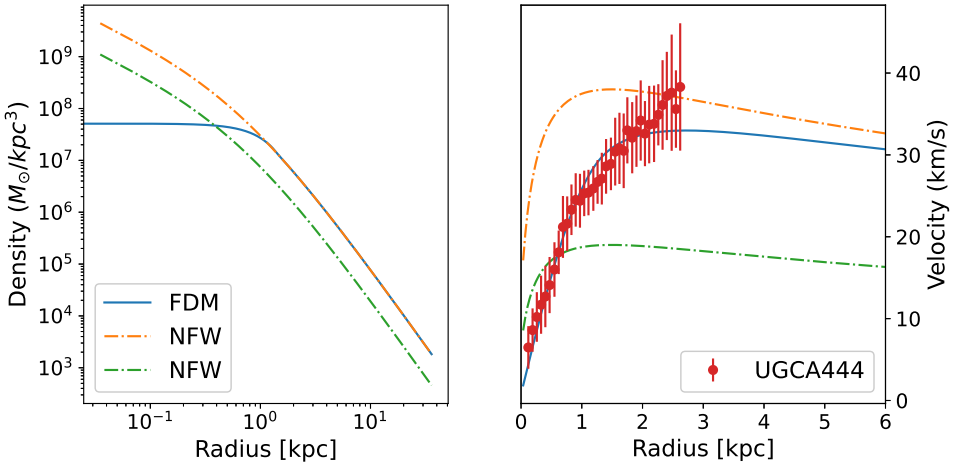

Figure 1.1: (Left) The density profile of two example NFW curves (orange, green) and an example (blue) FDM core-halo profile (later discussed in chapter 3). (Right) The equivalent velocity curves of the profiles from the left plot. Red errorbars correspond to observational data for the galaxy UGCA444, taken from the SPARC database [1].

within the halo. Specifically, the NFW profile is defined as

$$\rho_{\mathrm{NFW}}(r) = \rho_h \left(\frac{r_h}{r}\right)\left(1+\frac{r}{r_h}\right)^{-2}, \tag{1.1}$$

where ρ_h is a density scaling parameter and r_h is the 'scale radius', both varying for different halos.

Modified forms of Newtonian gravity (MOND) have also been put forth as an attempt to explain the behaviours that are a direct consequence of the presence of DM, however these struggle in various different aspects. Instead, a new and emerging idea to regard DM as a cosmic superfluid with coherence lengths on the scales of galaxies, resulting in the formation of galactic sized DM haloes, has been gaining traction. Where CDM has shortcomings and requires the addition of further in depth physics, such as baryonic feedback[21], a newer model has made progress in remedying such issues inherently.

1.2 Fuzzy Dark Matter

Fuzzy dark matter (FDM) has lately emerged as a popular alternative to the conventional cold dark matter (CDM) model. Following the first proposition of an ultralight bosonic dark matter constituent [22], an ultralight particle within the mass range $10^{-22} - 10^{-20}\,\mathrm{eV/c^2}$, leads to a description based not on incoherent particles, but on a single coherent wavefunction, with a

de Broglie wavelength of $\sim \mathcal{O}(1)$ kpc. Numerical simulations [23, 24, 25] have shown that on large scales, FDM replicates the cosmic web structure of cold dark matter, whilst addressing some alleged challenges that CDM faces on galactic scales. This result is best illustrated in FIG. 1 of [23]. Formation and growth of structures in such a dark matter background has been thoroughly investigated recently [26, 27, 28, 29]. The favourable look upon this type of dark matter in recent years has been motivated by the inherent properties which remedy ailments from which the CDM model allegedly suffers [16, 17, 18]. Among these, most notably, is the cusp-core problem[19] which is resolved in FDM since the balance between the quantum pressure and gravitation in FDM naturally forms a core, embedded in a NFW-like halo [30]. Furthermore, some tentative, more direct favourable evidence for FDM may have begun to emerge, see *e.g.* [31]. Scrutiny of this model has become an active area of research - see *e.g.* [32, 33, 34] for recent reviews and references to the literature.

The cores in FDM halos, often termed solitons, exhibit interesting dynamical behaviours. Given non-symmetric initial conditions, the cores formed from gravitational collapse exhibit a random walk within the base of the gravitational potential [35, 36]. Furthermore, scalar field oscillations are observed in numerical simulations [37, 23, 24, 35, 38, 39, 36, 40], and significant advances have been made in understanding the parameter dependence of their frequency [2, 41]. These oscillations manifest in the form of homogeneous radial expansion and contraction of the soliton core, and have been found to send out density waves into the surrounding halo [37]. In such non-symmetrically initialised simulations, the constructive interference of density waves and further stochastic density fluctuations [42, 43] also generate granules with a typical scale of the order of the central soliton core [23, 44, 24]. These granules have been stipulated to be the driving force behind the dynamical heating of stellar streams in the Milky Way [45], whilst density waves have been proposed as potential sources of disk heating [42]. Although the relation and interactions of the solitons to their host halos are very interesting and still to be fully explored, in this thesis we will examine the FDM soliton in isolation, without the backdrop of a complete halo initially. This will provide us with much needed insight into the behaviour of the core under variations of fundamental parameters, to better inform further analysis and discussion in more complex regimes.

Most FDM investigations have considered non-interacting bosons, for which the physical state of the system is described by a Schrödinger equation, coupled to the Poisson equation, in what is known as the Schrödinger-Poisson system of coupled equations (SPE). However, lacking any evidence to the contrary, the addition of particle-particle interactions renders the situation more interesting and dynamically complex – such a set-up, based on contact interactions adding a nonlinear contribution to the Schrödinger equation, has been the subject of many recent

works [2, 41, 46, 47, 48, 49, 50, 51, 52, 53, 54, 55]. Such a regime is governed by the Gross-Pitaevskii-Poisson equations,

$$i\hbar\frac{\partial\psi}{\partial t} = -\frac{-\hbar^2}{2m^2}\nabla^2\psi + mV\psi + g|\psi|^2\psi\,, \tag{1.2}$$

$$\nabla^2 V = 4\pi G|\psi|^2\,, \tag{1.3}$$

where the wavefunction is normalised such that $|\psi|^2$ is defined as the mass density of the system. Here, the self-coupling strength $g = 4\pi\hbar^2 a_s/m^2$ is considered as a short-range two-body contact interaction, which can be effectively associated with the s-wave scattering length a_s. For the remainder of this thesis, we will focus on repulsive self interactions where $g > 0$. We discuss these governing formulae in detail in the next chapter.

Although some works focus on the limiting case when interactions dominate (and the kinetic energy generating the quantum pressure becomes negligible), *e.g.* [56, 57, 58], effort has also been made to obtain general behaviours of self interacting FDM systems [2, 59]. Furthermore, constraints upon the possible strength of self-interactions along with the boson mass have very recently been examined [47, 48, 3, 51, 54] and, as a result, typical values for a repulsive self-coupling of $g \sim (10^{-32} - 10^{-26})\,\mathrm{Jm^3kg^{-1}}$ are usually quoted within the context of interacting FDM literature, with the exact value depending on the chosen boson mass. Even in the lower ranges, such a small self-interaction strength can still lead to clear and notable effects, which could be observationally relevant, with [3] presenting favourable observational evidence for the existence of a non-zero self-coupling. Attractive self interactions are most notably discussed in [49], where their effects are studied in the context of cosmic structure formation and the stability of cosmic filaments. Moreover, although attractive FDM solutions are typically unstable beyond a small range of allowed values, potentially leading to collapse and/or the formation of a black hole [2, 60], recent work [53] highlights the potentially favourable and desired role of attractive interactions in enhancing small-scale structure formation in large simulations of the cosmic web, inspired largely by [49]. Such examples of self interacting FDM would leave observational signatures like an increased number of solitons that form in areas of constructive interference in cosmic filaments, where instabilities are present under the attractive self interaction. Recently there has been a unique suggestion of a time-dependent self interaction, which begins as repulsive in the very early universe and switches to attractive, potentially describing the high rate of structure formation at high redshift [61].

Attempts have been made in literature to reconcile FDM with observational data from rotation curves of galaxies [62, 3, 63, 64, 65], though on many occasions results indicate that a singular boson mass is unable to describe the range of rotation curves obtained from data. This points to a significant issue in non-interacting FDM, that may well be remedied by the

introduction of self interactions which result in different rules for the shapes and sizes of FDM cores [2, 3]. Core-only fitting has demonstrated that a sample of the SPARC catalog [1] is well fit by a Gaussian ansatz for self interacting FDM [3].

With the wealth of new investigation into the possible effects of self interactions on FDM, a lot is left open for further study and exploration. For this reason, inspired by the aforementioned works, we choose to focus on the effects of repulsive self interaction in FDM.

1.3 Thesis Overview

This thesis aims to firstly study the effects of varied boson mass and self interaction strength on the characteristics of isolated soliton cores, both analytically and numerically via reduced 1D spherically symmetric simulations. We employ the knowledge gained here to fit a newly presented ansatz for the soliton core, under the influence of self interactions, to observational data from the SPARC [1] dataset, with the desire to demonstrate that self interactions are critically required to match observational data to theoretical profiles. In particular, we aim to reconstruct inferred observational density profiles in full 3D simulations, and to show that they are stable on relevant timescales and agree with these observational data. Finally, we wish to emphasise the possibility of using this 3D data, that corresponds to observationally inferred dark matter halos, to analyse particular static and dynamic behaviours and characteristics, such as the core-halo mass distribution, the core growth, and the velocity of test particles in static granular halo potentials. Our ultimate aim is to stress the importance and possibility of reconciling theoretical and numerical results for self interacting FDM with tangible, observable effects and data.

Specifically, in chapter 3, we firstly characterize in detail – both analytically and numerically – the effect of repulsive interactions on the size and shape of the underlying virialized solitonic core, building upon earlier work based on a Gaussian solitonic core of some interaction-dependent effective width [2]. By making use of the virialization condition, we derive analytical expressions characterizing the change in shape parameters as a function of interaction strength in the context of the empirical model of solitonic cores [23, 24, 66, 43]. Further introducing a characteristic interaction strength marking the crossover between weakly-interacting and strongly-interacting regimes – defined by equating the interaction energy to the quantum kinetic energy (see also [2, 50, 58]) – we are able to obtain analytical results for appropriately scaled soliton parameters (radius, peak density), cast only in terms of the ratio of the interaction strength to such characteristic value; such results smoothly interpolate between the previously studied non-interacting and strongly-interacting (Thomas-Fermi) limits.

To test the accuracy of our extended analytical predictions, we also perform detailed spherically symmetric numerical simulations of isolated soliton cores generated through the very efficient imaginary time propagation method widely used in cold atom studies [67] (yet scarcely seen in cosmological works [68]). We compare and contrast our virialized solitonic shapes both in the absence and presence of repulsive self-interactions to the Gaussian [2], Thomas-Fermi [2] and empirical [23] profiles, with our findings providing a direct bridge between all such limiting cases.

Moreover, our scaled analytical formulae are numerically confirmed to be independent of the values of the boson mass (m) and total soliton mass (M), at least within the probed ranges $10^{-22}\mathrm{eV/c^2} \leq m \leq 10^{-20}\mathrm{eV/c^2}$ and $10^6 M_\odot \leq M \leq 10^8 M_\odot$. Such an analysis facilitates a critical test of the typically-used empirical profile, and provides a direct relation of the scaling of central core density and soliton width as a function of scaled interaction strength, smoothly interpolating between relevant previous findings.

Our numerical analysis of soliton peak density and width (and later in chapter 6, oscillation frequency) point to the existence of a degeneracy between boson mass and self interaction strength in determining the resulting soliton parameters. We discuss the implications of such findings for uniquely determining both interaction strength and boson mass from potential observational signatures. Through this analysis, we highlight that care is necessary when imposing constraints on the boson mass in FDM, as the addition of a free parameter in the self-interaction strength could significantly widen the allowed parameter space for the boson mass. We thus indicate that strong constraints such as those discussed in [38, 43] should likely be revisited with this in mind.

In chapter 4, we introduce a new profile which exhibits an inherent dependence on our dimensionless, soliton-specific self interaction strength, Γ_g. We term this profile the Super-Gaussian (SG), which is empirically derived from fitting to numerical data from simulated ground state solutions for varying values of g. We join the SG profile to the widely used NFW profile to form a universal bimodal profile, used to map the entirety of a core-halo system. By selecting dim, dark matter dominated galaxies from the SPARC database [1], utilising the same selection criteria as in [3], we form a set of data which will be used for a 5-parameter fit. Through utilising the bimodal profile and exploiting the parameter degeneracy, a grid search is performed across a large 5D parameter space consisting of the soliton parameters (the peak density, boson self interaction, boson mass) and two relevant halo parameters (the halo density parameter and the scale radius). Ultimately, the result of the 5D parameter search for each galaxy is a family of curves, all of which fit within the specific galaxy's errorbars, and each corresponding to a specific pairing of m and g. Reformulating these data points in the $m-g$ parameter space into a density of points via a Gaussian kernel density approximation, we

compute a confidence region which points to a two-dimensional space of m and g parameters which can generate density profiles that fit well to the selected observational data.

Taking the highest confidence point from this space, equating to an optimal m and g pair, we perform another set of best fit density profile generations for the density profiles inferred from observational data [1], and find that the entire chosen data set can be fit well by this pair.

In chapter 5, we introduce the method by which we formulate our initial conditions for 3D FDM simulations. We detail the approach to generating a catalog of values for different total energies, in which the fundamental physical parameters (m, g), as well as the simulation specific parameters (computational box size, total mass) are kept fixed. Additionally, a system specific reference energy is introduced, which is equal to the total energy of the system if it were entirely cooled to the ground state. This is an important reference that we will show is remarkably useful in better understanding the form of the core-halo system. The effects of a variation of total system energy is shown, demonstrating the fact that in the self-interacting regime, a core does not behave as one would expect from analytical models [2]. By fitting the SG profile to the simulation data, we show that instead of increasing only in density while the radius shrinks, the core in fact grows in both radius and density. Making use of our newly defined reference energy, we demonstrate a simple relationship between total system energy and mass distribution between the core and halo, in contrast to the method in current literature [44, 69, 63, 64]. We present qualitatively the variation in granule structure and characteristics as a consequence of this energy variation, also. Finally, we demonstrate that using the machinery built in chapter 4, and the newly developed understanding of the energy of simulated systems, it is possible to recreate the velocity profiles of observational halos by creating a 3D simulation whose 1D density profile is approximately equal to a target density profile, equating to the SG best fit to a given galaxy. The results show that it is possible to recreate an approximate SG-NFW profile which corresponds to an observational galaxy, and that such a profile is stable across observationally relevant timescales.

In chapter 6, we evaluate the oscillation frequency of the core, building upon the early analysis of Chavanis [2], based here not on a Gaussian approximation to the soliton, but on the more accurate empirical profiles for which we explicitly derive a relationship between the peak density, ρ_0, and the soliton oscillation frequency, f – thus supplementing previous related works based solely on numerical fitting [39, 70, 71, 72, 43, 73]. Implementing a perturbative approach on our accurately virialized numerically generated solitons, we obtain accurate numerical predictions for these oscillations which we contrast to our analytical predictions, and simpler previous ones, building on important earlier work on such observables [39, 70, 71, 72, 43, 73]. We then extend our results to include repulsive self interactions by means of implementing a Γ_g

dependence on the shape parameters, as in chapter 3. We find that the simulated core oscillation frequency follows the analytical predictions with a variation in the self interaction strength. Based on this, and the work in chapter 3, we propose a scheme for uniquely identifying both the self-interaction strength and the boson mass by combining information of soliton shape details and oscillation frequency, which could potentially become available in future observational data analysis. Indeed, oscillations perturb the rotational velocity curves significantly within the soliton and in the region immediately adjacent to it [74]. A statistical evaluation of the gravitational heating of galaxies could therefore give a preliminary indication of a relationship between frequency and other soliton parameters.

We then turn to the consideration of non-isolated solitons, embedded in halos which are dynamically propagated. We show that the soliton core grows in density, as previously suggested in [75, 69], as low energy particles from the halo condense onto it, while the halo exhibits a radial growth. The implications this mechanism may have on system stability on time scales relevant to the age of the universe and galactic evolutionary time frames are discussed.

Finally, we study the orbital evolution of test particles placed randomly onto a plane in a static background FDM halo, corresponding to the galaxy UGCA444. We form a preliminary statistical analysis of the velocity dispersion of such test particles, demonstrating that the tangential velocities of test particles can vary greatly at inner galactic radii. The implication on orbital perturbations of test particles owing to the granular structure on the age gradient of stars across the galactic plane is mentioned. We discuss limitations of our method and findings, and propose avenues of future work.

1.4 Statement Regarding Authored Work

The work appearing in this thesis is spread across one existing and multiple in-preparation publications. Specifically, chapter 3 and the first half of chapter 6 are the focus of Indjin M, Liu I K, Proukakis N P and Rigopoulos G, "*Virialized profiles and oscillations of self-interacting fuzzy dark matter solitons*", 2024 Phys. Rev. D **109**(10) 10351 [76]. This work was presented at two conferences, Identification of Dark Matter 2022 (Vienna), where it was the subject of a talk titled "*Core oscillations in fuzzy dark matter*", and at the Balkan Physical Union 11 (Belgrade) where the results were presented in a poster titled "*An analysis of oscillations in fuzzy dark matter cores*". For the latter, I received the award for best poster in the conference section presented on from the European Physical Journal.

Chapter 4 and the final section of chapter 5 compose a paper, Indjin M, Liu I K, Proukakis N P and Rigopoulos G, "*SPARC galaxy rotation curves: numerical halo reconstruction and identification of a non-zero self coupling for fuzzy dark matter*" in preparation [77].

The remainder of chapter 5 constitutes a third paper, Indjin M, Liu I K, Proukakis N P and Rigopoulos G, "*The role of energy in fuzzy dark matter core-halo structures*", in preparation [78].

I have also been involved in another ongoing publication in preparation, Indjin M, Liu I K, Proukakis N P and Rigopoulos G, "*FDM halos with self-interactions: Fuzzy dark matter halos with repulsive self-interactions: field coherence, core and granule size and the vortex network.*", in preparation[1], where I have been involved in active discussions, planning and corroborating numerical results.

All numerical results presented in this thesis and their subsequent analyses are based on algorithms and codes I have developed and authored in Python (simulations, analysis and graphical presentation), Fortran95 (simulations) and MATLAB (analysis and graphical presentation). Simulations were mostly conducted on the Newcastle University ROCKET (CPU) and POWER (GPU) high-performance computing clusters, while some simpler simulations were also ran on a personal laptop computer.

[1]The results of this paper are not included in this thesis.

2

The Gross-Pitaevskii-Poisson Equation

We will, for the remainder of the thesis, model FDM using the GPPE. In the non-interacting regimes we discuss, where $g = 0$, the system reduces to the Schrödinger equation, which has simpler dynamics and behaviours as we will show. Our methods of simulating the systems will always involve a self-consistent computation of the gravitational potential for each timestep, by solving the Poisson equation. An added important consideration is that, as our analysis focuses on already gravitationally bound objects, we proceed in the context of a non-expanding universe. Therefore, all simulations we produce and analyse are conducted in a static, non-expanding space.

2.1 The theoretical model

To arrive at the governing equations for FDM, we first begin from the energy functional

$$E = \int d^3x \left[\frac{\hbar^2}{2m^2} |\nabla\psi|^2 + \frac{1}{2}\frac{g}{m}|\psi|^4 + V(|\psi|^2 - \bar{\rho}) - \frac{1}{8\pi G} V\nabla^2 V \right] \tag{2.1}$$

$$= \int d^3x \mathcal{H}\,, \tag{2.2}$$

The potential term in the energy functional should in fact be $V\left(|\psi|^2 - |\bar{\psi}|^2\right)$. This then leads to us considering the over and under densities in the following potential term on the next page. We require this for consideration of homogeneous distributions to infinity. The integral for the solution to the potential in the case of ρ being constant even at infinity results in a diverging potential in a homogeneous space, which should not be the case! In a homogeneous infinite space, we expect to feel no force in any direction. where $\mathcal{H}$ is the Hamiltonian. Our Lagrangian, in full form, is

$$L = \int d^3x \left\{ \frac{i\hbar}{m}\psi^*\partial_t\psi - \frac{\hbar^2}{2m^2}\left|\nabla\psi\right|^2 - \frac{1}{2}\frac{g}{m}\left|\psi\right|^4 - V\left(|\psi|^2 - \bar{\rho}\right) + \frac{1}{8\pi G}V\nabla^2 V \right\}. \tag{2.3}$$

We now write the following

$$L = \int d^3x\mathcal{L} \tag{2.4}$$

Perturbing the wavefunction according to $\psi^* \to \psi^* + \delta\psi^*$, and keeping only first order terms, yields

$$\delta L = \int d^3x \left\{ \frac{i\hbar}{m}\delta\psi^*\partial_t\psi - \frac{\hbar^2}{2m^2}\nabla\delta\psi^*\nabla\psi - \frac{g}{m}\delta\psi^*\psi^*\psi^2 - V\delta\psi^*\psi \right\}. \tag{2.5}$$

Using the fact that $\delta\psi^*$ is 0 at the boundaries, we can rewrite the second term inside the integral as

$$-\int d^3x\frac{\hbar^2}{2m^2}\nabla\delta\psi^*\nabla\psi = -\frac{\hbar^2}{2m^2}\left\{ \left[\delta\psi^*\nabla\psi\right]_{-\infty}^{\infty} - \int d^3x\delta\psi^*\nabla^2\psi \right\} \tag{2.6}$$

$$= \frac{\hbar^2}{2m^2}\int d^3x\delta\psi^*\nabla^2\psi, \tag{2.7}$$

which means we can now express Eq. (2.5) as

$$\delta L = \int d^3x \left\{ \frac{i\hbar}{m}\delta\psi^*\partial_t\psi + \frac{\hbar^2}{2m^2}\delta\psi^*\nabla^2\psi - \frac{g}{m}\delta\psi^*\psi^*\psi^2 - V\delta\psi^*\psi \right\}. \tag{2.8}$$

Writing the integrand as

$$\frac{\partial\mathcal{L}}{\partial\psi^*} = \frac{i\hbar}{m}\partial_t\psi + \frac{\hbar^2}{2m^2}\nabla^2\psi - \frac{g}{m}\left|\psi\right|^2\psi - V\psi, \tag{2.9}$$

which must be equal to 0, yielding the equation of motion,

$$i\hbar\partial_t\psi = -\frac{\hbar^2}{2m^2}\nabla^2\psi + \frac{g}{m}|\psi|^2\psi + V\psi. \tag{2.10}$$

For the Poisson equation, we vary instead according to $V \to V + \delta V$, giving

$$L + \delta L = \int d^3x \Big\{ \frac{i\hbar}{m}\psi^*\partial_t\psi - \frac{\hbar^2}{2m^2}|\nabla\psi|^2 - \frac{1}{2}\frac{g}{m}|\psi|^4 - (V+\delta V)(|\psi|^2 - \bar{\rho}) + \frac{1}{8\pi G}(V+\delta V)\nabla^2(V+\delta V)\Big\}. \tag{2.11}$$

Keeping only first order terms, again, we arrive at

$$\delta L = \int d^3x \left\{ \delta V \left[-(|\psi|^2 - \bar{\rho}) + \frac{\nabla^2 V}{4\pi G} \right] \right\}. \tag{2.12}$$

Making the same steps as before, and rearranging accordingly, we are left with the Poisson equation,

$$\nabla^2 V = 4\pi G(|\psi|^2 - \bar{\rho}) \,. \tag{2.13}$$

Here, and above, the average mass density, $\bar{\rho}$, has been subtracted to remove the 0-mode as is necessitated in Newtonian gravity [79, 2, 80]. Such an implementation is required if we are to include periodic boundary conditions, as we will be using for our 3D simulations. We will also normalise our wavefunction such that

$$|\psi|^2 = \rho \,, \tag{2.14}$$

giving us the mass density.

By applying the Madelung transformation, $\psi = \sqrt{\rho}\exp(iS)$, and separating real and imaginary parts, we obtain the continuity equation,

$$\frac{\partial\rho}{\partial t} + \nabla\cdot(\rho\mathbf{u}) = 0, \tag{2.15}$$

in which $\mathbf{u} = \hbar\nabla S/m$ and the equation of motion takes the form of the generalised Bernoulli equation,

$$\frac{\partial S}{\partial t} + \frac{1}{2m}(\nabla S)^2 + mV + mg - \frac{\hbar^2}{2m}\frac{\nabla^2\sqrt{\rho}}{\sqrt{\rho}} = 0. \tag{2.16}$$

The last term of Eq. (2.16) is the quantum pressure, which originates from the uncertainty

principle. In fact, in the non-interacting case ($g = 0$), it can be shown that for a system in equilibrium, the repulsion due to the quantum pressure balances the attraction due to gravity [81].

2.1.1 The system energy

The energy functional of the Gross-Pitaevskii equation can be written as

$$\begin{aligned} E &= \int d\mathbf{r} \left[\frac{\hbar^2}{2m^2} |\nabla\psi|^2 + \frac{1}{2} m V |\psi|^2 + \frac{1}{2} g |\psi|^4 \right] \\ &\equiv \Theta + W + U \end{aligned} \tag{2.17}$$

where Θ, W and U are the kinetic energy, the gravitational energy and the interaction energy respectively. As conventional, we can further decompose the kinetic energy into two components - the classical kinetic energy and the quantum kinetic energy,

$$\Theta_C = \frac{1}{2} \int \rho |\mathbf{u}|^2 d^3 r, \tag{2.18}$$

$$\Theta_Q = \frac{\pi\hbar^2}{2m^2} \int \frac{(\nabla\rho)^2}{\rho} r^2 dr. \tag{2.19}$$

An equilibrium solution experiences no time dependence and therefore has no classical kinetic energy, so the system must be virialised even within a static configuration.

2.1.2 Dimensionless GPPE

In order to numerically solve the GPPE we revert to dimensionless form by scaling all physical variables to appropriate values. This is done in terms of a time scale

$$T = (G\rho_{\text{ref}})^{-1/2}, \tag{2.20}$$

characteristic of an object crossing a uniform density configuration of some reference density ρ_{ref} and the corresponding energy and length scales

$$E = N\hbar\sqrt{G\rho_{\text{ref}}} \tag{2.21}$$

$$L = \left(\frac{\hbar^2}{m^2 G \rho_{\text{ref}}} \right)^{1/4} \tag{2.22}$$

for some particle number $N = M/m$. Setting $t = Tt'$ and $\mathbf{r} = L\mathbf{r}'$, the resulting dimensionless GPPE takes the form

$$i\frac{\partial\psi\prime}{\partial t'} = -\frac{\nabla'^2}{2}\psi' + V'\psi' + g'|\psi'|^2\psi' \tag{2.23}$$

and

$$\nabla'^2 V' = 4\pi\left(\frac{\rho_{\rm sys}}{\rho_{\rm ref}}\right)(\rho' - \bar{\rho}'), \tag{2.24}$$

where the interaction strength is written as $g = g'\hbar\sqrt{G\rho_{\rm ref}}/\rho_{\rm sys}$, the gravitational potential as $V = V'\hbar\sqrt{G}\rho_{\rm sys}/m\sqrt{\rho_{\rm ref}}$ and the wavefunction has been scaled to the mean density $\rho_{\rm sys}$ within the computational box through the dimensionless form $\psi' = \psi/\sqrt{\rho_{\rm sys}}$. We choose the mean reference density of the system as $\rho_{\rm ref} = 1.5\times10^3 M_\odot/{\rm kpc}^3$ which is commensurate with the current cosmic density. We will henceforth drop all primes for the sake of simplicity.

2.1.3 Spherically Symmetric Reduction

By making the substitution $\psi \to \phi/r$, we reduce the GPE to

$$i\frac{\partial\phi}{\partial t} = \left(-\frac{1}{2}\frac{\partial^2}{\partial r^2} + V + g\left|\frac{\phi}{r}\right|^2\right)\phi, \tag{2.25}$$

and the Poisson equation will become

$$\frac{\partial^2\mathcal{V}}{\partial r^2} = 4\pi r\rho. \tag{2.26}$$

Note that we no longer have need for the $\bar{\rho}$ term since we do not have periodic boundary conditions. The computational speed up acquired by translating to a spherically symmetric system and using this method is significant and allows for the study of higher mass solitons with larger resolution, where 3D approaches may suffer from a lack of computational power or simply from a lack of memory in being able to store large 3D arrays.

2.2 Numerical Tools

In this thesis, several numerical tools are used: Imaginary time propagation allows us to generate the ground state solution of a configuration while keeping the mass constant through renormalisation; fast fourier transform (FFT) algorithms from precompiled libraries are used to propagate the GPPE numerically and are the most time-efficient and energy-conserving algorithms widely used for this use case; for simpler studies of the soliton with no halo, a spherically symmetric reduction allows for the 3D problem to be reduced 1D, which significantly speeds

up numerical computation and allows for a much higher resolution. All these tools will be thoroughly described and discussed in this section.

2.2.1 Imaginary Time Propagation

Finding the ground state of a set of equations can be a tricky task. For the Schrödinger equation, one can apply a shooting method to reach the ground state solution of a given system [82, 41], however this can be quite cumbersome. A clever and common tool used in the study of cold atoms allows for a simple and elegant numerical method to find the ground state solution of a given system of equations. By propagating an initial state in imaginary time, simply by making the substitution $t \to -it$, one finds that all states are suppressed by exponential decay, the magnitude of which is proportional to the energy at a given level. That is to say, higher energy states are suppressed at an exponentially faster rate than low energy states. Let us consider a time dependent wavefunction, $\Psi(x,t)$, as superposition of eigenstates,

$$\psi(x,t) = \sum_{n=0} \psi_n(x) e^{-iE_n t/\hbar}. \tag{2.27}$$

If we transform $t \to -it$, then the wavefunction is now given by

$$\Psi(x,-it) = \sum_{n=0} \psi_n(x) e^{-E_n t/\hbar}. \tag{2.28}$$

We can factor out the ground state energy, arriving at

$$\Psi(x,-it) = e^{-E_0 t/\hbar}\psi_0 + \sum_{n=1} \psi_n(x) e^{-(E_n - E_0)t/\hbar}. \tag{2.29}$$

It is clear here that as t evolves, the higher energy states decay faster than the ground state. However, in such a method, the particle number and therefore the total mass in the system will decay, also. Therefore, when applying this to numerical methods, it is crucial to perform a renormalisation in each timestep. Every imaginary timestep, we assert that the total mass of the system is equal to some normalised value (typically we use L^3, where L is the length of the computational box). This is a simple and effective way to guarantee that the decay of energy manifests only as a migration of particles from higher energy states into the ground state, while total mass remains conserved. Assuming a solution exists and all numerical stability conditions are met, the total energy of the system will asymptote towards a ground state, and the generated profile is a very good numerical estimate of the true ground state solution of the equations.

2.2.2 The Pseudo-Spectral Method

For simulating the GPPE in 3D, we utilise a pseudo-spectral method known as the kick-drift-kick method, used in [24, 27]. When using this pseudo-spectral method, one must take into account the fact that the kinetic and potential energy operators do not commute. Therefore, to minimise this issue, a split-step method is introduced, whereby a half-step is performed in real space where the potential energy operator is applied, then a full-step in Fourier space is performed to apply the kinetic energy operator, and then another half-step in real space for the potential energy. In such a system, we may write the full evolution as

$$\psi(x, t+dt) \approx e^{\frac{1}{2}(V+g|\psi|^2)dt}\mathcal{F}^{-1}\left\{e^{\frac{-ik^2}{2}dt}\mathcal{F}\left[e^{\frac{1}{2}(V+g|\psi|^2)dt}\psi(x,t)\right]\right\}. \tag{2.30}$$

Here, $\mathcal{F}$ denotes the Fourier transform, and $\mathcal{F}^{-1}$ is the inverse Fourier transform.

To self-consistently solve the Poisson equation, we simply perform a double integration, which in Fourier space is equivalent to a division by k^2. Therefore, we have

$$V = \mathcal{F}^{-1}\left\{\frac{1}{k^2}\mathcal{F}\left[4\pi\frac{\rho_{\text{sys}}}{\rho_{\text{ref}}}\left(\rho - \bar{\rho}\right)\right]\right\}. \tag{2.31}$$

There exists a pertinent stability condition one must consider when approaching this system with a pseudo-spectral method [83, 24]

$$\Delta t \leq \max\left[\frac{1}{6}(\Delta x)^2, \frac{1}{|V|_{\max}}\right] \tag{2.32}$$

where we use dimensionless units and $\hbar = m = 1$. We strictly obey this condition in all cases, even going so far as to include a multiplicative factor in front to reduce it even further. We will discuss the fact that this reduction aids in energy conservation of simulations in chapter 5.

3

The FDM Soliton

A FDM halo consists of two components, a host NFW-like halo which exhibits a $\rho \propto r^{-3}$ profile in the outer regions, and a central soliton core hosted at the base of the gravitational potential. A fundamental assumption we will use throughout–and repeat in several sections for clarity–is that a complete core-halo system is a superposition of a partially populated ground state (the core) and the surrounding excited modes (the halo). Should a system be cooled down entirely, all mass would find itself in a solitonic ground state. It thus follows that the soliton core is a necessary and foundational part of the FDM halo, and is worth studying in detail for a clearer understanding of the whole picture. We begin such a study by formulating a generalised ansatz by way of several crucial assumptions.

In this chapter, we expand on the existing empirical profile found in [23] by endowing 'shape' parameters with a dependence on the self-interaction strength, allowing us to better predict specific soliton parameters, compared to what is known in the literature. We analyse the ranges these shape parameters take for varying self-interaction strengths, allowing us to form an enveloping picture of the soliton's equilibrium state as one dials the interaction strength. Finally, we uncover a new degeneracy in the soliton shape parameters under the influence of self-interactions, which may have profound effects on the observational implications of fuzzy dark matter.

3.1 The ground state solution to the GPPE

3.1.1 A preliminary ansatz

To understand the ground state soliton, we must first assume a generalised form for it so that we can probe the system. To do this, we construct a generalized ansatz, and on physical grounds we anticipate for such a general density profile to depend on the radial coordinate r, and the interaction strength g, only through the dimensionless ratios r/r_c and g/g_*, where g_* is a characteristic interaction strength to be defined later in terms of the self-interaction energy and the quantum pressure. We settle on the form [1]

$$\rho = \rho_0 \, \varphi \left(\frac{r}{r_c}, \Gamma_g \right), \tag{3.1}$$

where

$$\Gamma_g = \frac{g}{g_*}. \tag{3.2}$$

We have chosen Γ_g to avoid confusion with the Gamma function, Γ, which we will make use of extensively in a later section. Following Chavanis [2] we start our analytical studies by reducing the expression for the mass and various system energies in terms of relevant physical variables and appropriate dimensionless integrals, whose values can be calculated based on our generalised ansatz. Specifically we obtain the following expressions:

Total Mass:

$$M = 4\pi \int_0^\infty \rho_0 \, \varphi \left(\frac{r}{r_c}, \Gamma_g \right) r^2 dr, \tag{3.3}$$

$$= \eta(\Gamma_g) \, \left(4\pi \rho_0 r_c^3 \right). \tag{3.4}$$

Moment of Inertia:

$$I = 4\pi \int \rho_0 \, \varphi \left(\frac{r}{r_c}, \Gamma_g \right) r^4 dr, \tag{3.5}$$

$$= \alpha(\Gamma_g) \, \left(M r_c^2 \right). \tag{3.6}$$

[1] See [50] for a general density profile ansatz and [58, 2] for a similar scaled self-interaction strength.

Quantum Kinetic Energy:

$$\Theta_Q = \frac{2\pi\hbar^2}{m^2} \int \left| \frac{\partial}{\partial r} \left[\rho_0 \, \varphi \left(\frac{r}{r_c}, \Gamma_g \right) \right]^{1/2} \right|^2 r^2 \, dr \tag{3.7}$$

$$= \sigma(\Gamma_g) \left(\frac{\hbar^2 M}{m^2 r_c^2} \right). \tag{3.8}$$

Gravitational Energy:

$$W = \frac{8\pi G}{2} \int_0^\infty r M(r) \rho_0 \, \varphi \left(\frac{r}{r_c}, \Gamma_g \right) dr, \tag{3.9}$$

$$= -\nu(\Gamma_g) \left(\frac{GM^2}{r_c} \right). \tag{3.10}$$

Interaction Energy:

$$U = \frac{2\pi g}{m} \int \rho_0^2 \, \varphi^2 \left(\frac{r}{r_c}, \Gamma_g \right) r^2 dr, \tag{3.11}$$

$$= \zeta(\Gamma_g) \left(\frac{M^2 g}{2 m r_c^3} \right). \tag{3.12}$$

In the above expressions, $\eta(\Gamma_g)$, $\alpha(\Gamma_g)$, $\sigma(\Gamma_g)$, $\nu(\Gamma_g)$ and $\zeta(\Gamma_g)$ are parameters depending on the dimensionless interaction strength, obtained from a dimensionless integral directly related to the shape of the density profile of the soliton in the presence of self-interactions. We shall henceforth refer to such parameters as shape parameters [2]. It is crucial to our understanding of the system that we make note of the fact that such shape parameters depend explicitly on the dimensionless self-interaction, Γ_g. This immediately informs us that in the absence of self-interactions, a ground state soliton will have the same dimensionless shape regardless of the boson mass or soliton mass. This is characterised by constant shape parameters in the above formulae. That is to say that when the density and radius is scaled by some characteristic value, solitons will sit on top of each other in a dimensionless density-dimensionless radius plot, and such dimensionless solitons are scaleable to whichever density and radius one may wish. This of course means that numerical simulations can be scaled accordingly with quite some freedom. However, in the presence of self-interactions, the dimensionless soliton is not so easily scalable, and one must take great caution when attempting to do so.

Now that we have explicit formulae for the time-independent energies of the system, we are at a position where we can define Γ_g. As discussed previously, in the absence of self-interactions,

[2] Such parameters were first introduced in the pioneering work of Chavanis [2] who used a Gaussian approximation to the soliton density profile, which we will discuss in detail in a later section.

the quantum pressure term provides the outwardly pressure which maintains soliton structural stability and prevents gravitational collapse. Therefore, the ground state in this case is formed by an equilibrium between the outwards quantum pressure and the inwards gravitational force. With the addition of self-interactions, a new outwards pressure is contributed and three regimes can be identified.

- $U \ll \Theta_Q$: Here, the self-interaction energy is negligible compared to the quantum kinetic energy and the system can be regarded as non-interacting.
- $U \gg \Theta_Q$: Here, the quantum kinetic energy is negligible compared to the repulsive self-interaction energy, and the system is found within the Thomas-Fermi regime, in which the profile is well described by Eq. (3.38).
- $U \sim \Theta_Q$: This is the most complex of the three regimes, as there are few reasonable approximations that can be made to simplify the problem. Here, a complex balance between the quantum pressure and the repulsive self-interaction form a stable core.

In order to define Γ_g, we turn to the complex final case. By equating the quantum kinetic and self-interaction energies, we can obtain a term for the required value of g, which we term g_*. In other words, g_* is the value of the self-interaction strength for which the quantum kinetic and self-interaction energies are equal.

$$U(g = g_*) = \Theta_Q(g = g_*) \tag{3.13}$$

$$\zeta(\Gamma_g = 0) \left(\frac{M^2 g_*}{2mr_c^3}\right) = \sigma(\Gamma_g = 0) \left(\frac{\hbar^2 M}{m^2 r_c^2}\right). \tag{3.14}$$

Rearranging for g_* gives the final form,

$$g_* \equiv \left(\frac{\sigma_0^2}{\zeta_0 \nu_0}\right) \frac{10\hbar^4}{GM^2 m^3}\ . \tag{3.15}$$

Here, we have introduced σ_0, ζ_0 and ν_0, the shape parameters in the absence of self-interactions ($\Gamma_g = g = 0$) to avoid circular logic in the definitions of g_*[3]. With this definition, we may now write the form of Γ_g,

$$\Gamma_g = \left(\frac{\zeta_0 \nu_0}{\sigma_0^2}\right) \frac{GM^2 m^3 g}{10\hbar^4}. \tag{3.16}$$

Upon inspection it becomes clear that Γ_g is a soliton-specific dimensionless interaction strength. To better explain this, let us consider an example: Two isolated solitons of mass M_1 and M_2

[3] In reality, shape parameters are themselves dependent on g_*, therefore they must not be present in the definition of g_*. To bypass this, we instead use the constant values of the shape parameters in the non-interacting limit. This is not so important, as it is merely a factor scaling of the true dimensional importance of the relation.

exist where $M_1 > M_2$, in the presence of repulsive self-interactions mediated by the same real coupling strength, g. Since $\Gamma_g \propto M^2$, soliton M_1 will be exhibiting a greater ratio of $U : \Theta_Q$ than soliton M_2. Therefore, M_1 is further along the scale of self-interaction from non-interacting to Thomas-Fermi than M_1. Depending on the discrepancy between the two masses, one might find that soliton M_1 appears as a self-interacting soliton when the dimensionless shape is analysed, while soliton M_2 is well fit by a profile which assumes no self-interactions. We leave the discussion for different theoretical profiles–and their regions of validity–for a later section of this chapter.

3.1.2 Radius and the Virial Theorem

Given the above discussed ansatz, and the henceforth computed generalised forms of the energies, we can go a few steps further and obtain generalised formulae for the radius of the core by minimising the total energy of the system with respect to the radius. This will allow us to find the stable radius of the ground state, which will be crucial for further analysis. Asserting that the total soliton mass remains constant and that the soliton is isolated in space, we write the total energy as

$$E_t = \Theta_C(t) + \Theta_Q + W + U \tag{3.17}$$

$$= \Theta_C(t) + \sigma(\Gamma_g)\left(\frac{\hbar^2 M}{m^2 r_c^2}\right) - \nu(\Gamma_g)\left(\frac{GM^2}{r_c}\right) + \zeta(\Gamma_g)\left(\frac{M^2 g}{2m r_c^3}\right). \tag{3.18}$$

We assume that the ground state of the system is static and stable, which implies that the first term, the classical kinetic energy, is 0. Therefore, the total energy of the system in a static configuration is given by

$$E_t = \sigma(\Gamma_g)\left(\frac{\hbar^2 M}{m^2 r_c^2}\right) - \nu(\Gamma_g)\left(\frac{GM^2}{r_c}\right) + \zeta(\Gamma_g)\left(\frac{M^2 g}{2m r_c^3}\right). \tag{3.19}$$

Next, we must minimise the energy with respect to the core radius, r_c.

$$\frac{dE_t}{dr_c} = -2\sigma(\Gamma_g)\left(\frac{\hbar^2 M}{m^2 r_c^3}\right) + \nu(\Gamma_g)\left(\frac{GM^2}{r_c^2}\right) - 3\zeta(\Gamma_g)\left(\frac{M^2 g}{2m r_c^4}\right). \tag{3.20}$$

Setting this to 0 and rearranging for r_c gives us the final form of the core radius in the presence of self-interactions,

$$r_c(g) = \frac{\sigma(\Gamma_g)}{\nu(\Gamma_g)}\frac{\hbar^2}{GMm^2}\left(1 + \sqrt{1 + \frac{3}{2}\frac{Gm^3M^2}{\hbar^4}\frac{\zeta(\Gamma_g)\nu(\Gamma_g)}{\sigma^2(\Gamma_g)}\, g}\right). \tag{3.21}$$

The exact same relationship can also be acquired by first considering the virial theorem in the presence of self-interactions, given by

$$2(\Theta_C + \Theta_Q) + W + 3U = 0. \tag{3.22}$$

Once again stating that the configuration is in a steady state, we can remove the time-dependent classical energy and be left with the time-independent components,

$$2\Theta_Q + W + 3U = 0 \tag{3.23}$$

$$2\sigma(\Gamma_g)\left(\frac{\hbar^2 M}{m^2 r_c^2}\right) - \nu(\Gamma_g)\left(\frac{GM^2}{r_c}\right) + 3\zeta(\Gamma_g)\left(\frac{M^2 g}{2m r_c^3}\right) = 0 \tag{3.24}$$

By dividing through by $-r_c$, we retrieve Eq. (3.20) with the LHS set to 0.

The limiting cases

The previous expression for g_* allows us to obtain useful analytical expressions for the leading order dependence on the scaled interaction strength in the weakly and strongly interacting limits: in each such case we simplify the expression of Eq. (3.24) by replacing the Γ_g-dependent shape parameters by the corresponding constant parameters obtained analytically in the limiting cases of zero and strong interactions (Thomas-Fermi).

In the weakly interacting case, we thus introduce

$$r_c^0(g) = \frac{\sigma_0}{\nu_0}\frac{\hbar^2}{GMm^2}\left(1 + \sqrt{1 + \frac{3}{2}\frac{GM^2m^3}{\hbar^4}\frac{\zeta_0\nu_0}{\sigma_0^2}\, g}\right), \tag{3.25}$$

where subscripts 0 are used to denote corresponding shape parameter values at $g = 0$. This can now be rewritten in terms of the dimensionless interaction strength, Γ_g, in the more compact form

$$r_c^0(\Gamma_g) = \frac{r_c^{NI}}{2}\left(1 + \sqrt{1 + 15\Gamma_g}\right), \tag{3.26}$$

where r_c^{NI} describes the non-interacting value given later by Eq. (3.41).

Correspondingly, in the strongly-interacting regime we introduce the notation

$$r_c^{TF}(\Gamma_g) = \frac{r_c^{TF}}{2}\left(1 + \sqrt{1 + 15\,\frac{g_*}{g_*^{TF}}\,\Gamma_g}\right), \tag{3.27}$$

where r_c^{TF} corresponds to the value of r_c in the limit $g \to \infty$, and g_*^{TF} is defined as in Eq. (3.15),

but based on shape parameters evaluated analytically for the Thomas-Fermi profile, i.e.

$$g_*^{TF} \equiv \frac{\sigma_{TF}^2}{\zeta_{TF}\,\nu_{TF}}\,\frac{10\hbar^4}{GM^2m^3}\,. \tag{3.28}$$

The values of the shape parameters corresponding to the two limiting soliton profiles are given in Table 3.1 (columns 4 and 7 respectively for non-interacting and Thomas-Fermi limits).

Similar to the above discussion we define the limiting expressions for the interaction-strength dependence of the peak density, $\rho_0(\Gamma)$, in the non-interacting case; specifically we find

$$\rho_0^0(\Gamma) = \rho_0^{NI}\left(\frac{2}{1+\sqrt{1+15\Gamma_g}}\right)^3, \tag{3.29}$$

which comes from Eq. (3.4) and is also given in Eq. (3.34), whereas in the Thomas-Fermi limit

$$\rho_0^{TF}(\Gamma) = \rho_0^{TF}\left(\frac{2}{1+\sqrt{1+15\,\frac{g_*}{g_*^{TF}}\,\Gamma_g}}\right)^3. \tag{3.30}$$

In each above case, the shape parameters are evaluated at the corresponding limits. We also note here that

$$\frac{g_*}{g_*^{TF}} \simeq 0.546\,. \tag{3.31}$$

Crossover between Weakly- and Strongly-Interacting Regimes

The soliton size in the presence of interactions, $r_c(g)$, increases monotonically with g, always lying between these two limiting curves, i.e. $r_c^0(g) \leq r_c(g) \leq r_c^{TF}(g)$; this will be confirmed by numerical simulations below. Its exact behaviour can be directly extracted from Eq. (3.24) along with a numerical determination of the shape parameters $\sigma(\Gamma_g)$, $\zeta(\Gamma_g)$ and $\nu(\Gamma_g)$ via the more compact relation

$$r_c(\Gamma_g) = \frac{\sigma(\Gamma_g)}{\nu(\Gamma_g)}\frac{\hbar^2}{GMm^2}\left(1+\sqrt{1+15\,\mathcal{C}(\Gamma_g)}\right) \tag{3.32}$$

where we have introduced a generalised dimensionless interaction strength parameter $\mathcal{C}(\Gamma_g)$ which also accounts for interaction-induced shape effects via

$$\mathcal{C}(\Gamma_g) \equiv \left[\frac{\zeta(\Gamma_g)}{\zeta(0)}\,\frac{\nu(\Gamma_g)}{\nu(0)}\,\left(\frac{\sigma^2(\Gamma_g)}{\sigma^2(0)}\right)^{-1}\right]\,\Gamma_g\,. \tag{3.33}$$

Physical Origin	Shape Parameter	Gaussian [Eq. (3.39)]	Empirical [Eq. (3.44)]	Numerical $g = 0$	Numerical $\Gamma_g \in [10^{-5},\ 10^{4}]$	Thomas-Fermi [Eq. (3.38)]
Mass	η	0.4385	0.9347	0.9693 $\pm$0.0231	0.4731 - 1.0270	0.4385
Mom. of Inertia	α	1.5000	3.0009	3.0531 $\pm$0.0578	1.1163 - 3.1435	1.0497
Quant. Kin. Energy	σ	0.7500	0.3919	0.3865 $\pm$0.0038	0.3799 - 1.3053	1.2266
Grav. Energy	ν	0.3989	0.2919	0.3033 $\pm$0.0158	0.2936 - 0.4482	0.4584
Int. Energy	ζ	0.0635	0.0262	0.0247 $\pm$0.0007	0.0235 - 0.0823	0.0896

Table 3.1: Values for the various shape parameters arising from the relevant energy integrals depending on the exact profile shapes: Such values are obtained analytically for the cases of a Gaussian profile (an analysis already performed in Ref. [2] from which the values in the 3^{rd} column are quoted), and evaluated in this work also analytically for the empirical profile of Eq. (3.44) (4^{th} column). These are compared and contrasted to results from the numerical simulations in the non-interacting regime $g = 0$ (5^{th} column), and over a broad range of relevant interaction strengths smoothly interpolating between the non-interacting and strongly-interacting limits, showing the change in the shape parameters as a function of interactions (penultimate column). To highlight the observation that the values of some shape parameters decrease (η, α), while others (σ, ν, ζ) increase with increasing interaction, we depict the limiting high interaction strength values by blue. For comparison, the final column shows the analytically predicted values in the strongly interacting Thomas-Fermi regime, based on the Thomas-Fermi profile of Eq. (3.38). A graphical representation of the dependence of such shape parameters on scaled interaction strength Γ_g is shown in Fig. 3.2.

The corresponding dependence of the central density on interactions is then given by

$$\rho_0(\Gamma_g) = \frac{1}{4\pi\eta(\Gamma_g)} \frac{M}{r_c^3(\Gamma_g)}\,, \tag{3.34}$$

where $\eta(\Gamma)$ can again be determined from numerically obtained soliton profiles.

In section 3.3.2 we perform a detailed numerical study which will confirm the validity of the above semi-analytical formulae. Indeed, we will see below that a numerical determination of the shape parameters, along with Eqs. (3.46) and (3.34), describes the size and central density of a soliton of mass M, made up of bosons of mass m, very well across all values of the self-coupling g from the non-interacting to the strongly interacting regimes.

3.1.3 Possible Soliton Profiles

As discussed, a characteristic feature of the Gross-Pitaevskii-Poisson system is the coherent core-like soliton structure at the centre of the gravitational well of the halo [30, 38, 84, 35]. We discuss below closed form profiles frequently used in the literature to describe the spatial profile of the soliton in various limits.

Firstly, in the absence of self-coupling ($g = 0$), the gravitational attraction is solely balanced by the quantum pressure term. In this limit, the soliton density is usually approximated by the empirical profile [23]

$$\rho = \rho_0 \left(1 + \lambda \left(\frac{r}{r_c}\right)^2\right)^{-8} \tag{3.35}$$

where ρ_0 is the central (peak) core density and r_c represents the core radius, defined as the radius at which $\rho(r_c) = \rho_0/2$: this yields the exact value $\lambda = 2^{1/8} - 1 \approx 0.091$. We note here that while the above profile automatically satisfies the virial theorem $2\Theta_Q + W = 0$, in order to ensure this it is in fact critical to use the exact (as opposed to the approximate) value of λ quoted above (see also subsequent related comments).

We also stress here that ρ_0 and r_c are not independent parameters, and a central density-radius relation has been reported [23, 44, 72, 43, 73] in the form

$$r_c = \left(\frac{\rho_0}{1.9\mathrm{M}_\odot\mathrm{pc}^{-3}}\right)^{-1/4} \left(\frac{m}{10^{-23}\mathrm{eV}}\right)^{-1/2} \mathrm{kpc}\,. \tag{3.36}$$

Such an expression can also be obtained from variational energetic considerations [80].

Secondly, the opposite, strongly-interacting limit, corresponds to a hydrostatic equilibrium in which the gravitational attraction is balanced by repulsive interactions [2]. In this limit, the

solitonic core is instead approximated by a Thomas-Fermi profile [85, 86, 87, 88]

$$\rho_{TF}(r) = \rho_0^{TF} \left(\frac{R_{TF}}{\pi r}\right) \sin\left(\frac{\pi r}{R_{TF}}\right) , \tag{3.37}$$

of characteristic spatial extent R_{TF}.

For consistency with the notation used for the empirical profile, we introduce here the spatial extent, r_c^{TF}, corresponding to the point where the density drops to half its central value, i.e. $\rho_{TF}(r_c^{TF}) = (1/2)\rho_{TF}(r = 0)$, thus yielding

$$\rho_{TF}(r) = \frac{\rho_0^{TF}}{1.895} \frac{r_c^{TF}}{r} \sin\left(1.895 \frac{r}{r_c^{TF}}\right) . \tag{3.38}$$

More generally, but only accounting for global shape features without attention to detailed radial dependence, the soliton can also be approximated by a Gaussian [2]: while only approximate, and a poor description for both the $g = 0$ and $g \to \infty$ limits, such description has two obvious benefits: (i) it facilitates an easy qualitative interpolation across these two limiting cases in the context of an effective interaction-dependent width, and (ii) it is easily amenable to analytical calculations. The form of such a Gaussian is

$$\rho(r) = M \left(\frac{1}{\pi r_c^2}\right)^{3/2} \exp\left(-\frac{r^2}{r_c^2}\right) . \tag{3.39}$$

The different arising density profiles and a comparison with our more accurate numerical results (discussed in Sec. 3.3.1-3.3.2) are shown in Fig. 3.1 across the entire range of interactions, with g_* denoting a characteristic interaction strength, marking an approximate crossover from the non-interacting to the strongly-interacting limits.

We note here that a super-Gaussian core [78], is the first profile suggested (with the exception of [89]) to exhibit a variation in the dimensionless shape of the profile, dependent on the dimensionless self-interaction parameter Γ_g. However, we will leave an in-depth discussion of this profile for the end of the chapter, as it will be a significant focus for later parts of the thesis. We will now focus on the empirical profile, and possible modifications which extend the usability to repulsive self interactions, also.

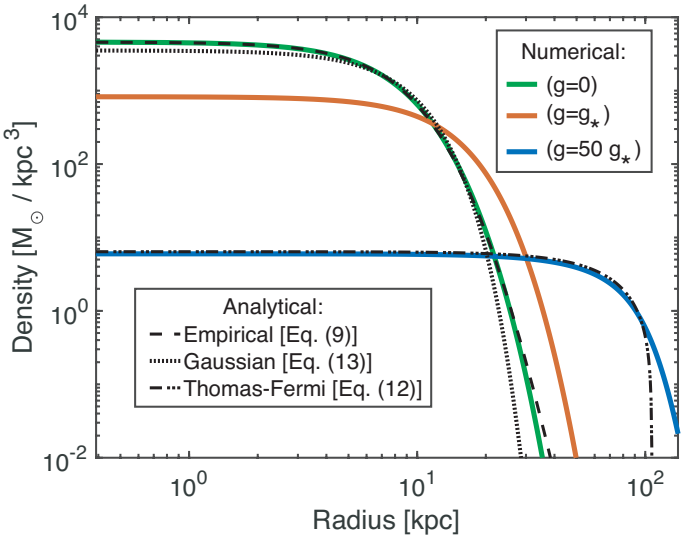

Figure 3.1: Dependence of the shape of density profiles on interaction strength for characteristic examples, and comparison between numerical (generated using imaginary time propagation to find the ground state solution) and analytical predictions in such regimes, with interaction strength increasing from top to bottom curves. Compared to the non-interacting limit (top green line), we also show a profile with self-interactions of an adequate strength (g_*) to impact the properties of the soliton (orange line), and the corresponding profile in the Thomas-Fermi regime of strong self-interactions. The empirical profile is given in Eq. (3.35), the Thomas-Fermi and Gaussian and profiles are respectively defined by Eq. (3.38) and Eq. (3.39). In all cases, the profiles are normalised to $M = 1 \times 10^7\ M_\odot$, and with $m = 2 \times 10^{-22}\ \mathrm{eV/c^2}$. The characteristic interaction strength g_* corresponds to the value marking an approximate crossover from weakly-interacting to strongly-interacting, and is defined in Eq. (3.15) by balancing interaction and quantum kinetic energies – see subsequent discussion in the text.

3.2 The non-interacting empirical profile

The empirical profile [23] is the most widely used and widely accepted profile for a non-interacting soliton.

In the absence of interactions, the Virial theorem between the quantum kinetic and the gravitational energies

$$2\Theta_Q + W = 0 \tag{3.40}$$

can be used, jointly with the above energy expressions to establish a direct relationship between peak density and core radius [2]. We thus obtain from Eqs. (3.8), (3.10) and (3.40) an expression for the soliton radius, r_c in the non-interacting limit, in the form

$$r_c = \frac{2\sigma_0}{\nu_0}\frac{\hbar^2}{GMm^2}\ . \tag{3.41}$$

This can also be simply obtained from setting Γ_g to 0 in Eq. (3.24). Substitution of this into the

earlier reduced expression for the soliton mass Eq. (3.3), provides a relation between r_c and ρ_0, namely

$$r_c = \left(\frac{2\sigma_0\hbar^2}{4\pi\nu_0\eta_0 G m^2}\right)^{1/4} \rho_0^{-1/4}. \tag{3.42}$$

Interestingly, an $r_c \propto \rho_0^{-1/4}$ relationship along with a coefficient of proportionality were numerically obtained from fitting [23, 44] without any explicit reference to virialization. Our present analysis extends such numerically-based results by an analytical derivation of the coefficient of proportionality based on the empirical profile of Eq. (3.35), explicitly showcasing its dependence on a range of physical parameters. A similar, albeit different, relationship was also previously given in [50].

It is now possible to rephrase the equation for soliton mass M in terms of a single parameter only, for example in terms of the peak density ρ_0, in the form

$$M = 4\pi\eta_0 \left(\frac{2\sigma_0\hbar^2}{4\pi\nu_0\eta_0}\right)^{3/4} \rho_0^{1/4}. \tag{3.43}$$

Using this relation, the empirical profile in Eq. (3.35) for the non-interacting limit can be reformulated as

$$\rho(r) = \frac{M}{4\eta_0\pi r_c^3}\left(1+\lambda\left(\frac{r}{r_c}\right)^2\right)^{-8}. \tag{3.44}$$

As the empirical profile provides the best approximation to the ground state of the GPPE in the non-interacting limit, Eqs. (3.41) and (3.44) reveal that, for any given pair of values for the soliton and boson masses (M, m), one can ***ab initio*** generate a virialised soliton profile for the non-interacting case, with shape parameters taken from the empirical profile. Such a $g = 0$ profile is shown in Fig. 3.1, demonstrating the good agreement with the numerical solution of the GPPE discussed in the next section.

3.3 The self-interacting empirical profile

The empirical profile is excellent at describing the soliton in the non-interacting case, but there are modifications which can be applied to extend the possibility of the empirical profile's fit to the self-interacting case. Although the resulting profile is not self-consistent[4], the resulting calculations for the soliton core radius, peak density (and later oscillation frequency) will be shown to agree excellently with data from numerical simulations. By noticing that an increase

[4]We will discuss this in detail in the later sections, though it is worth noting here that the alterred form of the mass formula is not consistent with the true soliton mass. However, it does provide the correct relationship between ρ_0 and r_c.

	η	σ	ν	α	ζ
a	0.4	1.15	0.5	0.3	1.1
b	1.5	1.5	1.7	1.5	1.5

Table 3.2: The fitting constants for Eq. (3.45).

in repulsive self interaction strength results in a change in the dimensionless shape of the numerically simulated soliton, we solely apply modifications to the empirical profile by bestowing a Γ_g dependence onto the otherwise constant shape parameters from the empirical profile.

3.3.1 Soliton shape parameters

Ground states were generated for a range of g values, for several different configurations of m and M. Shape parameter values were extracted from these numerical ground states by computing the various energy components, as well as the mass of the soliton and its moment of inertia. This allowed us to isolate the numerical value of each shape parameter. Such behaviour is shown for all 5 shape parameters (η, σ, ν, α and ζ) in Fig. 3.2. As evident, all such parameters follow a clear monotonic transition from the non-interacting limiting case (leftmost part, green points) to the Thomas-Fermi case (rightmost part), with some of them decreasing (η, α) and others increasing (σ, ν, ζ) with increasing (scaled) interaction strength Γ_g.

Interestingly, we find that the dependence of all such shape parameters on Γ can be excellently fit by a function of the form

$$u(\Gamma) = \frac{u_0 - u_{TF}}{2}\left[1 - \tanh\left(\frac{\log_{10}(\Gamma) - a}{b}\right)\right], \tag{3.45}$$

where u denotes any of these shape parameters, subscripts 0 and TF denote the corresponding analytical values in each regime, and a and b are fitting constants. The specific chosen values of these fitting constants for each shape parameter are given in Table 3.2, and vary slightly for each shape parameter. Nevertheless, in all cases, both a and b are of order unity.

An important comment needs to be made regarding the shape parameter σ, which originates from the quantum pressure. Given that the Thomas-Fermi regime is defined by a negligible quantum pressure, the analytical value computed from the quantum kinetic energy integral for the Thomas-Fermi profile loses meaning. Moreover, the deviation of the numerical values for σ from the fit in Fig. 3.2 for large values of $\Gamma_g > 10^3$, can be attributed to the much steeper decrease of the Thomas-Fermi profile towards a zero value (in stark contrast to the smoother decrease of the numerically generated profiles).

Next, we comment on the validity of the Gaussian approximation for different values of g. As is evident from Fig. 3.2, the Gaussian values taken from Ref. [2] always fall within our

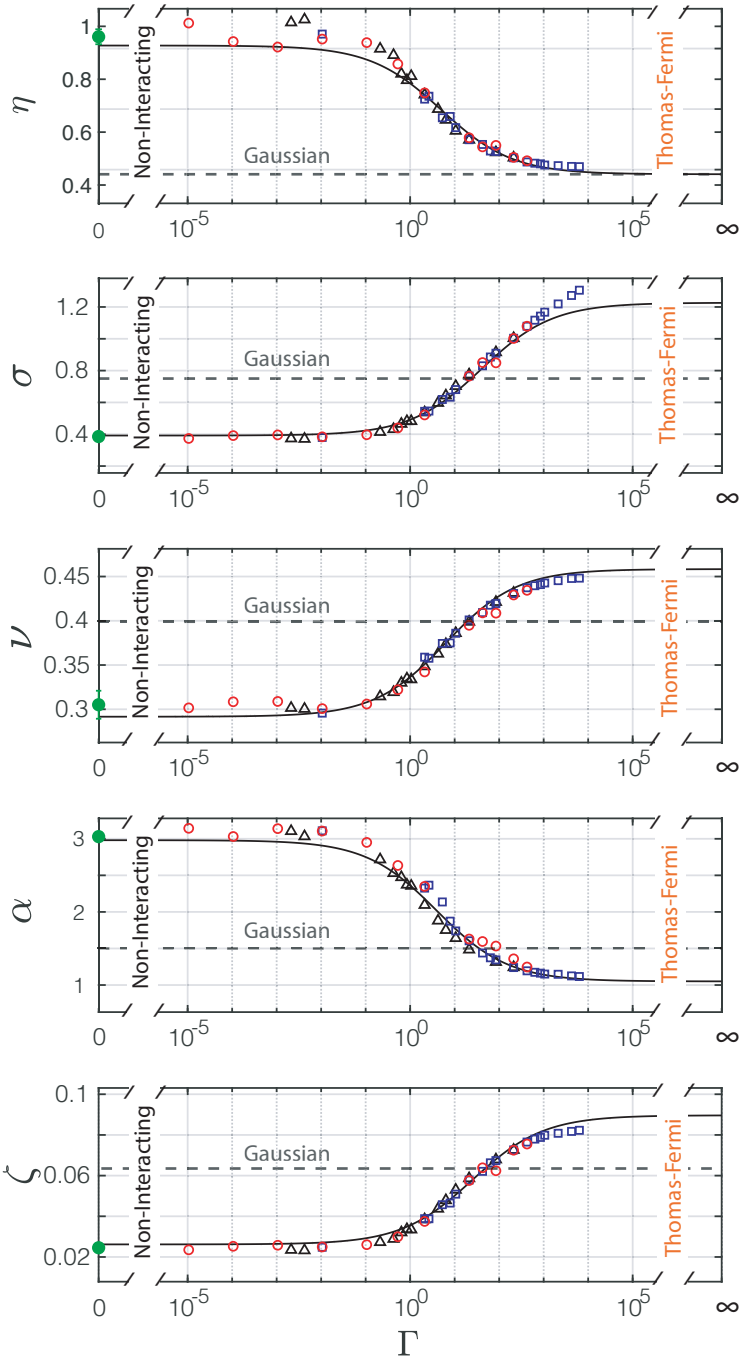

Figure 3.2: Dependence of the value of shape parameters on interaction strength, scaled to the characteristic value g_* defined by Eq. (3.15). Such dependence is reproduced by a two-parameter fit based on Eq. (3.45) which has as limiting cases the non-interacting limit at $\Gamma_g = 0$ (left), and the Thomas-Fermi limit at $\Gamma \to \infty$ (right), whose exact values for each parameter are given in Table 3.1. The corresponding predictions of Ref. [2] based on a Gaussian approximation (reported in Column 3 of Table 3.1) are shown here by the horizontal dashed line. Filled green points at the $g = 0$ line represent the averaged values of the corresponding shape parameters from numerical simulations (see Table 3.1, fifth column).

obtained numerical range: in fact, such points typically lie close to the midpoint between our presented analytical limiting values (except for η where the Gaussian value effectively corresponds to the Thomas-Fermi limit), and, as such, are good approximate values in the crossover regime. Note however that although such values are never off by more than a factor of 3, such analytically convenient choice of values cannot capture the true variable nature of the shape parameters.

3.3.2 Computing Soliton Parameters

Using the shape parameters as defined above, we obtain closer approximations to the soliton parameters: ρ_0, r_c (and the frequency, f, though this will be discussed later). By taking results from our 1D simulations, mentioned in the previous section, we can compare semi-analytical predictions of the parameters to those extracted numerically.

Superimposing numerical data points for 3 different total mass M and soliton mass m combinations (in the range $2\times10^{-22}\,\mathrm{eV/c^2} < m < 2\times10^{-21}\,\mathrm{eV/c^2}$ and $10^7\,\mathrm{M_\odot} < M < 10^9\,\mathrm{M_\odot}$), shown by different symbols/colours, the dependence of scaled peak density and soliton core on Γ_g is shown over the entire probed range of $\Gamma_g \in [4\times10^{-6},\, 3\times10^3]$.

Analytical expressions for these curves can also be obtained as follows: The scaled soliton width dependence on Γ can be obtained through Eq. (4.2) as

$$\frac{r_c(\Gamma_g)}{r_c(0)} = \left(\frac{\sigma(\Gamma_g)}{\sigma_0}\right)\left(\frac{\nu(\Gamma_g)}{\nu_0}\right)^{-1}\left(\frac{1+\sqrt{1+15\,\mathcal{C}(\Gamma_g)}}{2}\right) . \tag{3.46}$$

The corresponding dependence of the peak density can be obtained from Eq. (3.34) via

$$\frac{\rho_0(\Gamma_g)}{\rho_0(0)} = \left(\frac{\eta(\Gamma_g)}{\eta_0}\right)^{-1}\left(\frac{r_c(\Gamma_g)}{r_c(0)}\right)^{-3} . \tag{3.47}$$

Inputting our numerically-evaluated universal shape parameter dependence on Γ_g based on Eq. (3.45) for $\sigma(\Gamma_g)$, $\nu(\Gamma_g)$, $\zeta(\Gamma_g)$, and $\eta(\Gamma_g)$ into the above equations yields the solid black lines in Fig. 3.3(a)-(b): such curves are clearly found to lie directly on top of all our numerical points for different $(M,\, m)$ combinations. To clarify such observations, in each of the two cases we also plot the corresponding fully-analytical weakly-interacting ($r_c^0(\Gamma_g)$, $\rho_0^0(\Gamma_g)$) [solid grey lines] and strongly-interacting (Thomas-Fermi) limits ($r_c^{TF}(\Gamma_g)$, $\rho_0^{TF}(\Gamma_g)$) [dotted orange lines], defined respectively by Eqs. (3.26), (3.29) and (3.27), (3.30). These curves delimit the region where all our data points lie and which we indicate by green shading.

In both cases we clearly see a transition from the non-interacting behaviour for small Γ_g to the Thomas-Fermi behaviour for large Γ_g, with such transition indeed occurring around $\Gamma_g = 1$,

i.e. near the characteristic interaction strength g_* of Eq. (3.15); such value has been highlighted by a vertical dashed red line for easier visualization. To make such transitions between the two limiting cases more transparent, we further highlight the weakly- and strongly-interacting limits in subplots (i) and (iii), respectively found to the left and right of the main plot.

We have thus fully characterized our soliton ansatz of Eq. (3.1) in terms of a universal dependence on the (scaled) interaction strength, with such behaviour obtained semi-analytically (by a combination of analytical expressions combined with the universal dependence of the shape parameters on Γ_g) and confirmed by full numerical simulations.

3.3.3 The degeneracy of the boson mass and self coupling strength

Our preceding analysis for a soliton of fixed total mass M has been conducted under an implicit further assumption of a fixed boson mass m. As anticipated, this has revealed a dependence of static and dynamical properties on the boson interaction parameter g, which enters as a new parameter appearing both implicitly and explicitly in the equations for the soliton radius $r_c(g)$, [Eq. (3.24)], the peak soliton density $\rho_0(g)$ [Eq. (3.34)] and the soliton oscillation frequency $f(g)$ [Eq. (6.16)]. We discuss the oscillation frequency in chapter 6 in depth, while introducing the notion here for completeness.

To explain this, let us focus below on the soliton radius r_c in the absence or presence of interactions, for which we remind the reader of the main functional dependence of the previous expressions (under the assumption of a fixed M). These take the respective forms:
For $g = 0$:

$$r_c(m) = \mathcal{A}_0 \left(\frac{1}{m^2}\right) , \tag{3.48}$$

where $\mathcal{A}_0 = 2(\sigma_0/\nu_0)(\hbar^2/GM)$ depends on the non-interacting shape parameters (and the physical constants $\hbar$, G and constant soliton mass M).
For $g > 0$:

$$r_c(m, \Gamma_g) = \mathcal{A}(\Gamma_g) \left(\frac{1 + \sqrt{1 + 15\mathcal{C}(\Gamma_g)}}{2}\right) \left(\frac{1}{m^2}\right) \tag{3.49}$$

$$= \mathcal{A}(\Gamma_g)\, \bar{\mathcal{C}}(\Gamma) \left(\frac{1}{m^2}\right) , \tag{3.50}$$

where $\mathcal{A}(\Gamma) = 2(\sigma(\Gamma)/\nu(\Gamma))(\hbar^2/GM)$ is defined in terms of the Γ-dependent shape parameters, and for convenience we have also introduced an expression $\bar{\mathcal{C}}(\Gamma) \geq 1$, which has convenient

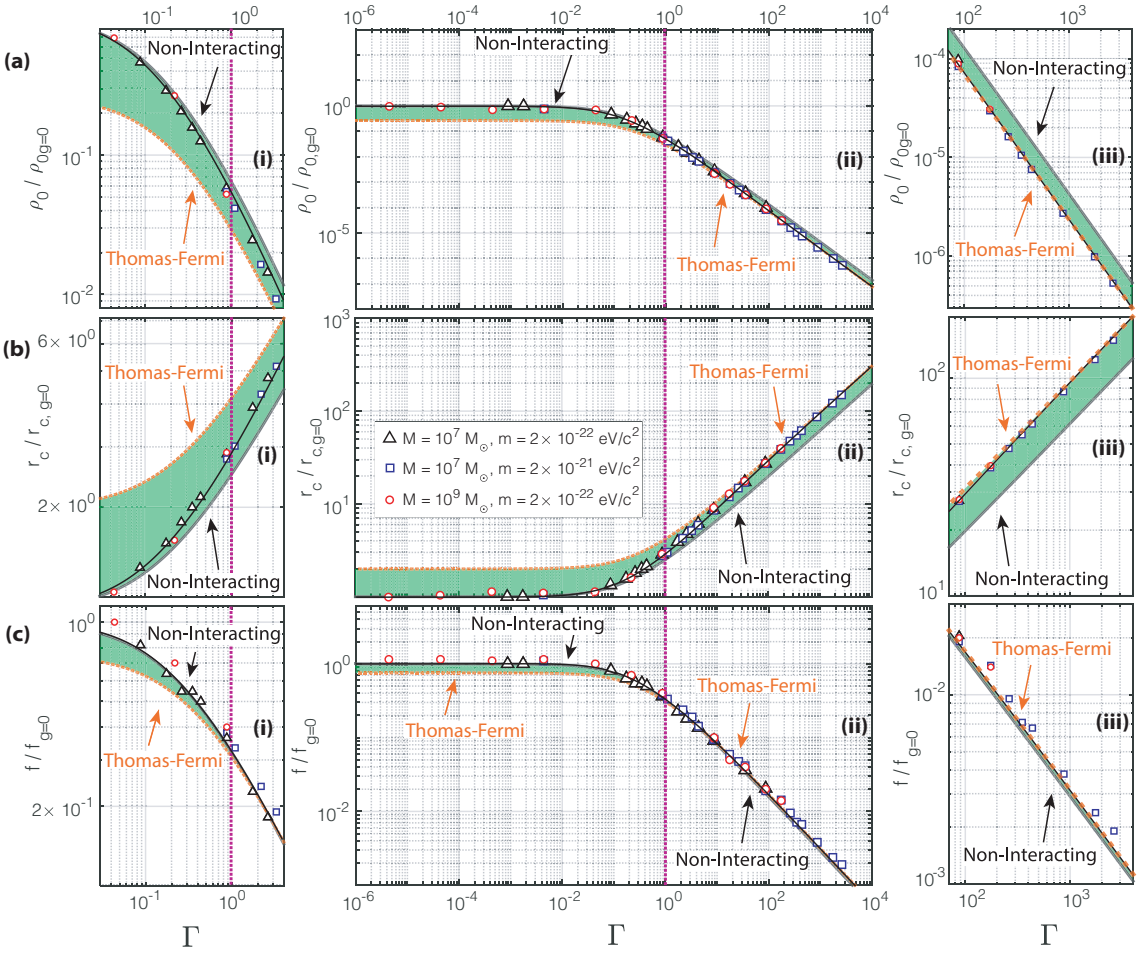

Figure 3.3: Universal dependence of key static and dynamical soliton properties on scaled dimensionless interaction strength. Shown are [from top to bottom] the cases for (a) peak soliton core density, (b) core radius, and (c) is explicitly discussed in chapter 6, and has been included here for the sake of completeness. The core oscillation frequency is shown here, with such quantities scaled to their corresponding non-interacting simulated values, and all self-interactions scaled to the characteristic value g_* from Eq. (3.15). All plots show numerically simulated data for 3 different $(M,\ m)$ combinations and a continuous solid black line obtained from our analytical equations (3.46), (3.47), (6.22) using as input the Γ_g-dependent shape factors shown in Fig. (3.2). Panels (ii) [middle] reveal the entire crossover, with (i) left and (iii) right panels respectively highlighting the weakly-interacting and strongly-interacting limits. The two limiting boundaries of the green channels highlight the range of accessible predicted values, bounded from above and below by the respective characteristic universal curves: specifically, the non-interacting grey line is constructed from Eqs. (3.29), (3.26), (6.22)), with g_* [Eq. (3.15)] computed using the non-interacting shape parameters; moreover, the dashed black Thomas-Fermi line arises from Eqs. (3.29), (3.26), (6.22) with g_* [Eq. (3.15)] calculated instead using the Thomas-Fermi shape parameters. The vertical purple line highlights the characteristic interaction strength value $g = g_*$ (corresponding to $\Gamma_g = 1$). Note that a cross-over between the limiting non-interacting and Thomas-Fermi lines is in fact present in the case of the oscillation frequency [(c)(ii)], despite this being largely obscured by the very narrow accessible channel. We highlight that the excellent fit of our semi-analytical predictions (solid back lines) through all our numerical data demonstrates the importance of the correct incorporation of the universal variation of shape parameters on scaled interaction strength. Remarkably, such an approach accurately predicts the peak density, radius and frequency, even in the transition region between non-interacting and Thomas-Fermi limits.

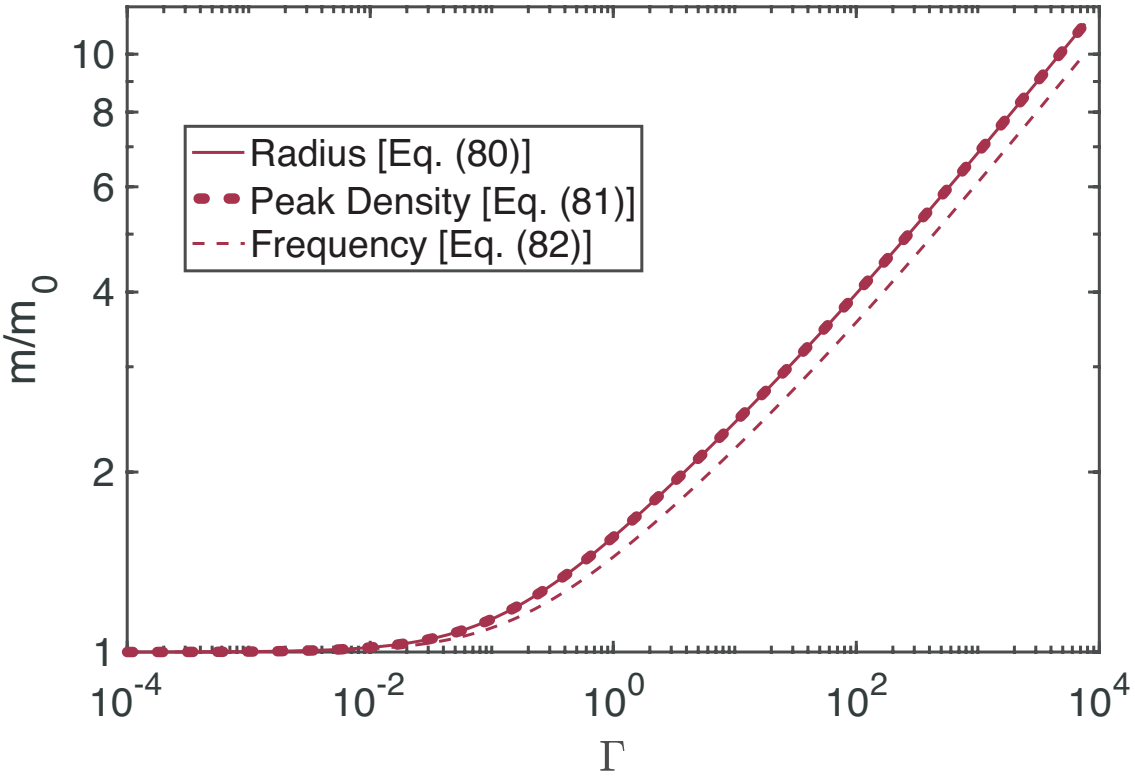

Figure 3.4: The scaled universal $m - \Gamma_g$ curves for which one obtains solitons of constant radius, peak density and oscillation frequency, corresponding to Eq. (3.51), Eq. (3.52) and Eq. (3.53) respectively. Here, m_0 is defined as the boson mass at $\Gamma_g = 0$ for the respective soliton parameters (r_c, f, ρ_0).

limiting cases

$$\bar{\mathcal{C}}(\Gamma = 0) = 1,$$
$$\bar{\mathcal{C}}(\Gamma \to \infty) = \frac{\sqrt{15\mathcal{C}(\Gamma)}}{2}\,.$$

From Eq. (3.49), we see that the inter-dependence of parameters r_c, m and $\Gamma = g/g_*$ implies that it takes a combination of the values of two of these parameters to fix the third one. Given that the main observationally-relevant physical quantities are likely to be the soliton mass M (already assumed as constant in above discussion) and the soliton radius, we shall henceforth assume here a fixed value for the soliton radius $r_c(m, \Gamma) = R_c$, and consider the resulting inter-relation between the boson mass m and the scaled boson self-interaction Γ. Thus by inverting Eq. (3.50), we obtain for each value of R_c the following dependence of m on Γ

$$m(\Gamma) = \frac{1}{R_c^{1/2}} \left[\mathcal{A}(\Gamma)\,\bar{\mathcal{C}}(\Gamma)\right]^{1/2}. \tag{3.51}$$

This expression shows clearly that fixing r_c to the value R_c and varying Γ results in a varying $m(\Gamma)$ curve which becomes a locus of all values of the boson mass and dimensionless self-coupling corresponding to a soliton of fixed radius R_c. The idea of such curves corresponding to parameter values that result in the same soliton radius was first put forward in [90, 50].

The same logic can be independently applied for fixed values of each of the peak density and the frequency [5]. In particular, the corresponding equations defining these degeneracy curves read:
For a fixed peak density, ρ_0,

$$m(\Gamma) = \left(\frac{4\pi}{\rho_0}\right)^{1/6} \left[(\eta(\Gamma)\,\mathcal{A}(\Gamma))^{1/6}\,(\bar{\mathcal{C}}(\Gamma))^{1/2}\right] . \tag{3.52}$$

For fixed frequency, f,

$$m(\Gamma) \;=\; f^{1/3}\,\mathcal{B}(\Gamma)\left(\sqrt{\frac{2\bar{\mathcal{C}}(\Gamma)}{15\mathcal{C}(\Gamma)+2\bar{\mathcal{C}}(\Gamma)}}\,\left(\bar{\mathcal{C}}(\Gamma)\right)^2\right)^{1/3} \tag{3.53}$$

where we have introduced

$$\mathcal{B}(\Gamma) = \frac{\sqrt{\alpha(\Gamma)\sigma^3(\Gamma)}}{\nu^2(\Gamma)}\,\frac{4\sqrt{2}\pi\hbar^3}{G^2M^2}. \tag{3.54}$$

Equations (3.52) and (3.53) determine the loci of all values of m and Γ which result in solitons of the same central density and same oscillation frequency respectively. Once again, we briefly introduce and discuss the oscillation frequency here for completeness, but leave detailed discussion for chapter 6. In all cases, such *degeneracy curves* reduce to their corresponding non-interacting limits when we take $\Gamma = 0$, being consistent with a single viable boson mass value.

Such dependences of the boson mass m on Γ, resulting in (m, Γ) pairs that support solitons of fixed radius, peak density and oscillation frequency, are shown in Fig. 3.4. Note that the boson mass has been scaled by a reference mass $m_0 = m(\Gamma = 0)$ to make the plot universal. In this plot, we see clearly that the curves corresponding to fixed soliton radius[6] and fixed peak density overlap, whereas the scaling for fixed frequency reveals qualitative similarity but is distinctly identifiable.

In the above discussion, the mass has been obtained as a function of the dimensionless interaction strength $\Gamma = g/g_*$ for fixed soliton radius, peak density or oscillation frequency. It can be instructive to reconsider the problem in terms of the relation between the boson

[5] We will discuss the frequency in detail in a later chapter, but for completeness we include the degeneracy relationships and their observational relevance here.

[6] See similar figures 4 and 5 in [50] for the case of solitons of fixed radius.

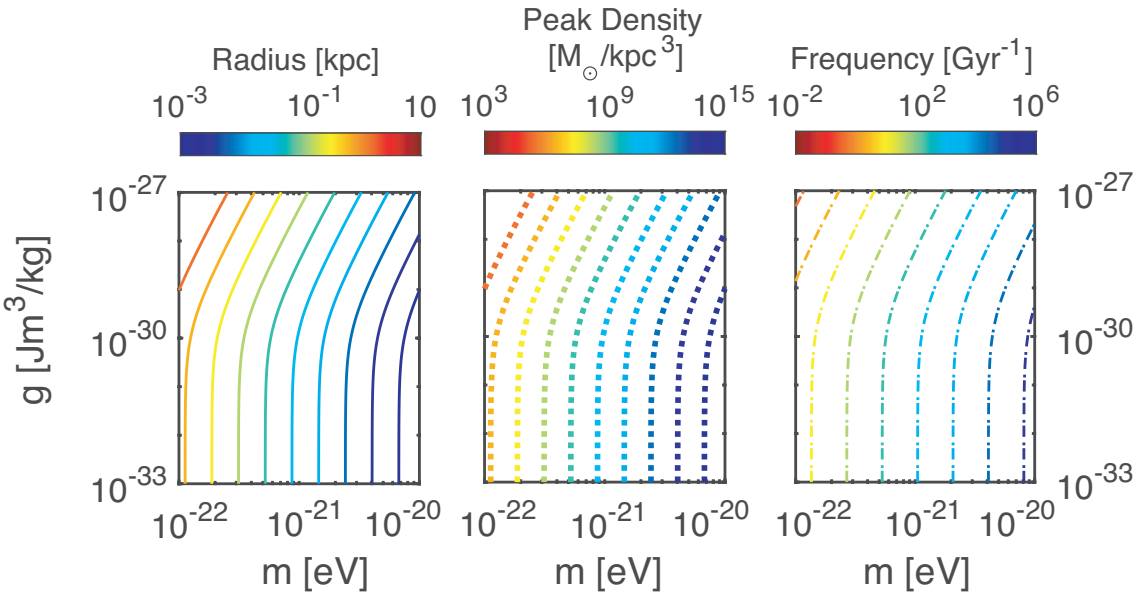

Figure 3.5: Curves of constant radius, peak density and oscillation frequency (the value of which is shown by the colourbars), revealing the allowed parameter space of repulsive self-interaction strength and boson mass based on such chosen parameters. These graphs can be extended towards the heavier boson mass regimes. The figure plotted for a soliton mass $M = 10^8 M_\odot$.

self-interaction strength g, and the boson mass m, for any fixed value of soliton radius, peak density or oscillation frequency, parameterised through a particular value of Γ. This can be done by writing

$$\begin{aligned} g(\Gamma, m) &= \Gamma\, g_*(m) \\ &= \Gamma \left(\frac{10\hbar^4}{GM^2}\right) \left(\frac{\sigma^2(\Gamma)}{\zeta(\Gamma)\nu(\Gamma)}\right) \frac{1}{m^3(\Gamma)}\,, \end{aligned} \tag{3.55}$$

where $m(\Gamma)$ depends on r_c, ρ_0 or f, as given in Eqs. (3.51), (3.52) and (3.53) respectively. Tracing over the parametric variable Γ, and for each fixed value of radius, peak density or frequency, we can thus obtain a parametric relation between g and m. Such dependence is plotted in the three panels of Fig. 3.5, in which the fixed value of each such parameter is represented by a different colour line.

3.3.4 Observational Relevance

For any single soliton with radius r_c and peak density ρ_0, we have explicitly shown that there exists an entire contour line of boson mass and interaction strength pairings that support its

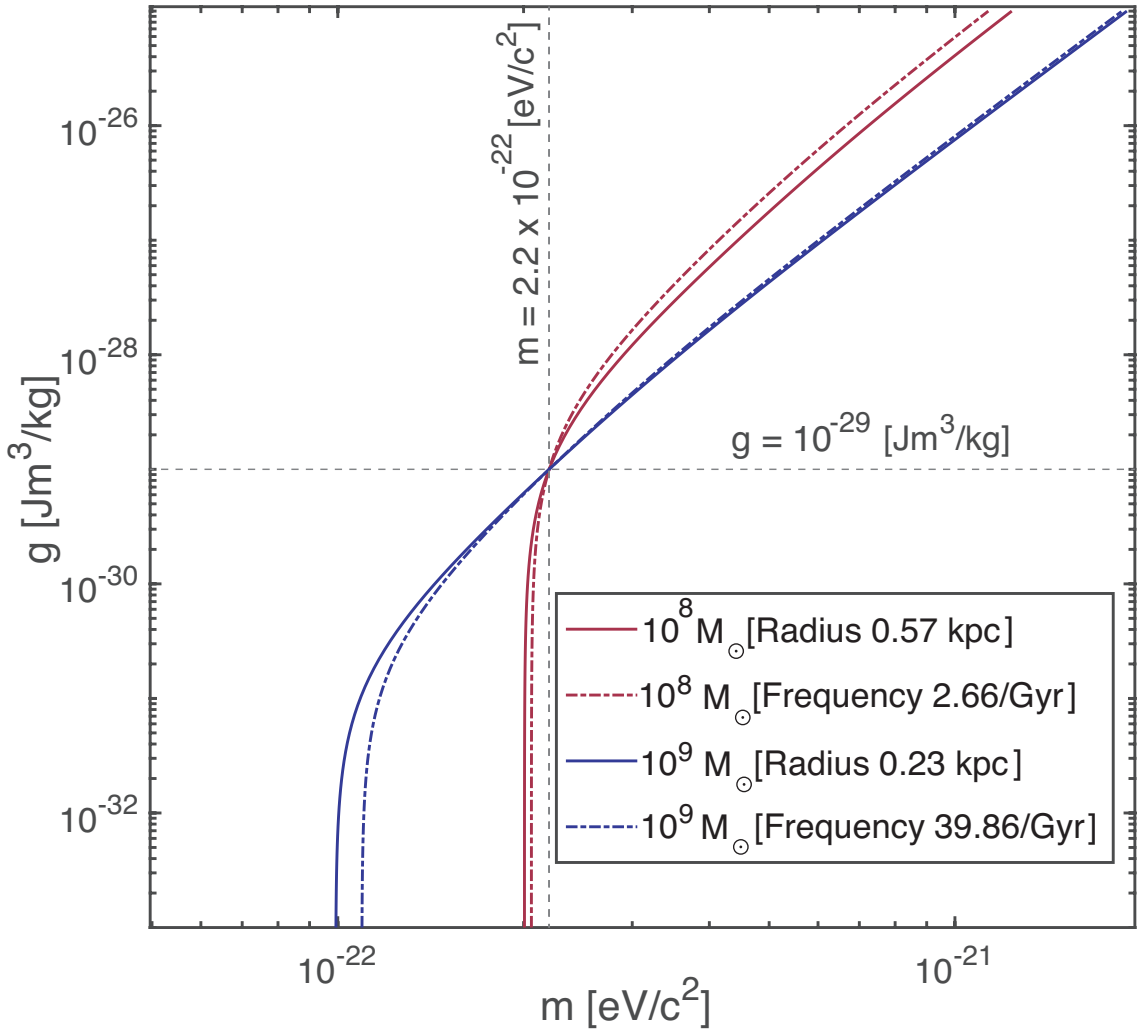

Figure 3.6: Scheme for simultaneous identification of boson self-interaction and mass through the numerical overlap of key soliton $g-m$ degeneracy lines for two different galaxies. Shown are heuristically chosen lines of constant radius (solid) and frequency (dashed) for soliton masses of $M = 10^8 M_\odot$ (red) and $M = 10^9 M_\odot$ (blue). Their overlap points to a unique combination of g and m values for such systems. Here we have chosen to show a $0.57\,\mathrm{kpc}$ radius and an oscillation frequency of $2.66\,\mathrm{Gyr}^{-1}$ for the $10^8 M_\odot$ soliton, whereas the $10^9 M_\odot$ soliton has a $0.23\,\mathrm{kpc}$ radius, and an oscillation frequency of $39.86\,\mathrm{Gyr}^{-1}$. A single underlying FDM model would result in the degeneracy curves from a multitude of solitons with different masses, radii and oscillation frequencies all crossing at the same point (see text).

existence within FDM. This rules out basing any constraints on a high-resolution accurate observation of a singular galactic dark matter object as the degeneracy means that no meaningful limits can be established; instead one can only deduce which contour the object must lie on. However, multiple objects of different total soliton mass will have differing contour lines, where the $g(m)$ gradients are dependent on their total mass. As a result, when one maps the contour lines of several galactic objects onto the same set of appropriately scaled axes, their intersection point will correspond to the true physical value of the boson mass and self-interaction strength which enables the formation of such solitons in our universe.

Fig. 3.6 illustrates this point: First, we consider a specific pair of boson mass and self-interaction strength, $m = 2.2 \times 10^{-22}\,\mathrm{eV/c^2}$ and $g = 10^{-29}\,\mathrm{Jm^3/kg}$ which, for a given soliton mass, will yield a specific set of soliton parameters - the core radius, peak density and oscillation frequency. We then note that any points along the corresponding $m(g)$ degeneracy contour will yield an identical soliton - *i.e.* the resulting solitons are observationally indistinguishable for points chosen anywhere along a single degeneracy contour line for a fixed total mass.

We can now consider two solitons of different mass, chosen as $10^8\,M_\odot$ and $10^9\,M_\odot$, and plot their degeneracy contour lines in the $m - g$ parameter space, along which the radius and frequency remain constant (for fixed total mass). In this specific case, the $10^8\,M_\odot$ soliton has a $0.57\,\mathrm{kpc}$ radius and an oscillation frequency of $2.66\,\mathrm{Gyr}^{-1}$, whereas the $10^9\,M_\odot$ soliton has a $0.23\,\mathrm{kpc}$ radius, and an oscillation frequency of $39.86\,\mathrm{Gyr}^{-1}$. These values were chosen heuristically for the purpose of illustrating clearly how the information of the true boson mass and interaction strength may be extracted from the contour lines. The location of the intersect of these contour lines is the true boson mass and self-interaction strength which accommodates both of these solitons to exist in space. Once again, in our case the intersect values were arbitrarily chosen as an initialisation requirement. In a universe where the dark matter is fuzzy and described by a single scalar field, all degeneracy curves corresponding to candidate observed solitons must cross at the same point (within observational error bars) which would represent the single universal value for the mass m and self-coupling g that correspond to our universe.

The existence of the aforementioned degeneracy could have an impact on current constraints on the boson mass which are likely to change if the parameter space is extended to include g.[7] Indeed, various limitations have been placed upon the allowed range of the boson mass by probing both cosmological scales *e.g.* [49, 91], as well as singular astronomical objects such as the star cluster orbiting the centre of Eridanus II [38, 43] or rotation curves and stellar kinematics [92, 93, 94, 65]. Furthermore, [95] finds a correlation between the core oscillation

[7] Although the relative ranges of m and Γ exhibited in fig. 3.4 may imply that existing constraints on the boson mass will not be shifted by orders of magnitude, it is still the case that including the self-coupling may be relevant.

and the oscillation of gas, which would further be affected by self-interaction and would prove a likely observational signature. All these works, apart form [49], do not include a self-interaction and in some cases clear differences between theoretical fits and observational data were identified [94], while in others it was further evident that a single boson mass could not adequately fit theoretical curves to observational data [92, 65]. On the other hand, [3] reports that a non-zero value of the self-coupling, along with a single boson mass, can fit the rotation curves of the dark matter dominated galaxies in the SPARC database, providing for the first time positive support for FDM solitons with a non-zero value of the self-interaction from rotation curves. The degeneracies discussed here would be relevant for all the above studies which make inferences about the boson mass.[8] Clearly, all of the above are very preliminary observational investigations but provide strong motivation for precise, quantitative analysis of the model [76]. Steps have been taken to incorporate baryons into these models [72, 98], which would likely add an additional layer of complexity.

The method of identifying intersections of degeneracy curves shown in FIG. 3.6 lends itself well to possible constraints on self interacting FDM through study of observational data. We will make use of this developed machinery to highlight that there exists a favourable region in the $m-g$ parameter space that lends itself well to generating theoretical core-halo systems that fit well to observational data in the following chapter.

[8] In this work we discussed parameter degeneracies related to the compact FDM solitons. Similar degeneracies can also exist on cosmological scales for FDM overdensity power spectra, see [96] which analyses a linearized hydrodynamical version of the hybrid condensate particle model of [97].

4

Observational Comparisons to Theoretical and Numerical Rotation Curves

In literature, various attempts have been made to fit FDM velocity profiles to inferred observational rotation curves from telescope data. For full fits including both the core and halo [63, 64, 65] a non-interacting bimodal profile is typically used; specifically, for non-interacting fits, a marriage of the soliton core profile [23] for the central core and the NFW profile [20] for the halo. Unfortunately across various pieces of literature, the estimations of the boson mass from observational rotation curves of galaxies are in tension with each other, and studies across multiple galaxies find that a single value of m cannot explain the variety of curves from individual surveys [65]. Results for the boson mass which accurately recreate fits to observational data generally lie in the range $10^{-23} - 10^{-20}$ eV/c^2, though in [65] a single boson mass is attributed only to one galaxy. Such tensions are most likely owed to the fact that dark matter cores have radii commonly of order $\sim$ kpc, while their total core mass varies significantly.

This is not possible given the non-interacting regime of FDM where the radius depends strongly on the total core mass, $r_c \sim 1/M_c^2$. Previous surveys of observational curves considering non-interacting FDM have identified core masses that vary across an entire order of magnitude [3], while their radius remains approximately the same. In the non-interacting

paradigm, one would expect from theory that the core radius will vary by an order of 10^2. Therefore, it becomes clear that one must introduce self interactions to limit the effects of the core mass on the radius. There is, unfortunately, limited literature and attention on this topic. One work [3] has specifically aimed to fit a Gaussian core with self-interactions to the inferred core region of the velocity profiles from the SPARC [1] database, by first selecting the dark matter dominated galaxies and then isolating the inner points to fit the core. This allowed them to obtain a convergence to a single value of m and g that fits the observational data by means of a χ^2 fit. However, in many cases, this only involves fitting to the inner-most parts of the velocity profile and leaves many data-points unused in the halo region. Furthermore, the Gaussian profile's dimensionless shape is invariant to changes in the local scaled strength of self interactions, and the computation for the peak density can give values that deviate significantly from numerical solutions of the ground state, particularly in the cases of strong self interactions.

To remedy these points, we first introduce a novel profile termed the Super-Gaussian (SG). This profile exhibits dependence on Γ_g inherently, and is therefore a natural choice for ansatz to describe a self interacting soliton core. We consider the case of the bimodal SG-NFW profile where the transfer from the inner profile to the outer occurs at the transition radius, r_t. The rules for this transition have been set out in the following section and are crucial for the formation of physically stable and relevant density profiles with no artificial discontinuities and cut-offs of the core profile.

This chapter, therefore, provides a novel profile for fitting to a fuzzy dark matter core, ranging continuously from the non-interacting limit, to the strongly interacting limit. We derive the necessary computations for the shape parameters, and provide a unique recipe for which one may apply a bimodal fit using this novel profile in tandem with the NFW profile to observational data. We thus utilise the degeneracy uncovered in the previous chapter to formulate our results in the form of a heatmap, which strongly implies the necessity for repulsive self-interactions if fuzzy dark matter is to explain *all* the observational data chosen from the dataset.

4.1 The SG Profile

It has been made clear in the previous chapter that a profile with a shape-dependency on Γ_g is needed to more accurately describe a self interacting soliton. Therefore, we now consider a Super-Gaussian (SG) of the form

$$\rho_{\rm SG}(r) = \rho_0(\Gamma_g) \exp\left[-\ln 2 \left(\frac{r}{r_c(\Gamma_g)}\right)^{\Upsilon(\Gamma_g)}\right], \tag{4.1}$$

where Υ is some function of Γ_g that defines the power of the SG, and therefore the dimensionless shape. We now write the self-interacting radius relation again for convenience,

$$r_c(\Gamma) = \frac{\sigma(\Gamma)}{\nu(\Gamma)} \frac{\hbar^2}{GMm^2} \left(1 + \sqrt{1 + 15\,\mathcal{C}(\Gamma)}\right) \tag{4.2}$$

and note that the equation for the total mass, acquired from integrating the density, rearranged for ρ_0 is

$$\rho_0(\Gamma_g) = \frac{1}{4\pi\eta(\Gamma_g)} \frac{M}{r_c^3(\Gamma_g)}. \tag{4.3}$$

Knowing the above formulae, we can derive the analytical forms of the SG shape parameters by computing the relevant energy integrals, as done in Table 3.1 of chapter 3 for the Gaussian, Empirical and Thomas-Fermi profiles. To solve the energy integrals using the SG profile, the following identity must be used:

$$\int_0^\infty e^{-u^\ell} u^m du = \frac{1}{\ell} \Gamma\left(\frac{m+1}{\ell}\right), \tag{4.4}$$

where Γ is the gamma function (not to be confused with Γ_g). The solutions to the mass, energy and moment of inertia integrals are presented below. The mass of the profile is

$$M = 4\pi\rho_0 r_c^3 \eta_{\text{SG}}(\Gamma_g) \tag{4.5}$$

$$\text{where} \quad \eta_{\text{SG}}(\Gamma_g) = \left(\frac{1}{\ln 2}\right)^{3/\Upsilon(\Gamma_g)} \frac{1}{\Upsilon(\Gamma_g)} \Gamma\left(\frac{3}{\Upsilon(\Gamma_g)}\right). \tag{4.6}$$

The quantum kinetic energy of the SG system is

$$\Theta_Q = \sigma_{\text{SG}}(\Gamma_g) \frac{\hbar^2 M}{m^2 r_c^2} \tag{4.7}$$

$$\text{where} \quad \sigma_{\text{SG}}(\Gamma_g) = \frac{\Upsilon(\Gamma_g)^2 (\ln 2)^{2/\Upsilon(\Gamma_g)}}{8} \frac{\Gamma\left(\frac{2\Upsilon(\Gamma_g)+1}{\Upsilon(\Gamma_g)}\right)}{\Gamma\left(\frac{3}{\Upsilon(\Gamma_g)}\right)}. \tag{4.8}$$

The gravitational energy is

$$W = -\nu_{\text{SG}}(\Gamma_g) \frac{GM^2}{r_c} \tag{4.9}$$

$$\text{where} \quad \nu_{\text{SG}} = \frac{1}{2\eta^2 \Upsilon(\Gamma_g)^2 (\ln 2)^{5/\Upsilon(\Gamma_g)}} \Gamma\left(\frac{5}{\Upsilon(\Gamma_g)}\right) B\left(\frac{1}{2}; \frac{2}{\Upsilon(\Gamma_g)}; \frac{3}{\Upsilon(\Gamma_g)}\right) \tag{4.10}$$

The interaction energy is

$$U = \zeta_{\mathrm{SG}}(\Gamma_g)\frac{gM^2}{2mr_c^3} \tag{4.11}$$

$$\text{where } \zeta_{\mathrm{SG}}(\Gamma_g) = \frac{1}{\Upsilon(\Gamma_g)(\ln 2)^{3/\Upsilon(\Gamma_g)}}\left(\frac{1}{2}\right)^{3/\Upsilon(\Gamma_g)-1}\Gamma\left(\frac{3}{\Upsilon(\Gamma_g)}\right)\frac{1}{8\pi\eta_{\mathrm{SG}}^2}. \tag{4.12}$$

Finally, the moment of inertia is

$$I = \alpha_{\mathrm{SG}}(\Gamma_g)Mr_c^2 \tag{4.13}$$

$$\text{where } \alpha_{\mathrm{SG}}(\Gamma_g) = \frac{1}{\Upsilon(\Gamma_g)\eta_{\mathrm{SG}}(\Gamma_g)(\ln 2)^{5/\Upsilon(\Gamma_g)}}\Gamma\left(\frac{5}{\Upsilon(\Gamma_g)}\right). \tag{4.14}$$

With the knowledge of the above analytical forms of the shape parameters, given a chosen boson and soliton mass, and a value of $\Upsilon(\Gamma_g)$, we can ***ab initio*** compute ρ_0 and r_c.

To develop an understanding of $\Upsilon(\Gamma_g)$, we rely on numerical computations of the soliton ground state via imaginary time propagation. We consider solitons of constant total mass ($2\times10^7 M_\odot$) and boson mass ($2\times10^{-22}\mathrm{eV/c^2}$), and varying repulsive self interaction strength ($5\times10^{-28}\mathrm{Jm^3/kg} \leq g \leq 2\times10^{-22}\mathrm{Jm^3/kg}$). This is done by initiating a spherically symmetric simulation with an initial Gaussian shape, with an arbitrarily chosen radius and a fixed total mass. These initial states are propagated in imaginary time, as detailed in Sec. 2.2.1. The final result is a dynamically stable solution which corresponds to the ground state solution for the chosen total mass, boson mass and self interaction strength. These final states are then used as fitting basis to engineer a relationship between $\Upsilon(\Gamma_g)$ and Γ_g.

Primarily, we must obtain a value of $\Upsilon(0)$, for the $g=0$ case, due to the fact that we define g_* using the non-interacting shape parameters. Given this value, we can analytically compute all the shape parameters for the SG ($\eta_{0,\mathrm{SG}}, \sigma_{0,\mathrm{SG}}, \nu_{0,\mathrm{SG}}, \alpha_{0,\mathrm{SG}}, \zeta_{0,\mathrm{SG}}$) in the non-interacting limit, which in turn allows us to compute the peak density and core radius in this limit. By performing a χ^2 fit of generated SG profiles, as detailed above, with Υ as the free parameter, we find that a value of $\Upsilon(0) = 1.62$ produces the most promising fit of the SG to the numerical ground state solution of the non-interacting soliton. Armed with the knowledge of the shape parameter values in the non-interacting limit for the SG profile, which in turn tells us $g_{*,\mathrm{SG}}$, we can proceed to compute Γ_g, and therefore the peak density and radii, of all further cases in the interacting regime. We select a range of repulsive interaction strength g, such that the probed dimensionless interaction strength equates to a $0 \leq \Gamma_g \leq 4\times10^4$, which should comfortably cover the entire span from the non-interacting limit to the Thomas-Fermi limit.

By performing a χ^2 fit on each profile, we thus obtain a range of $\Upsilon(\Gamma_g)$ values which are fit

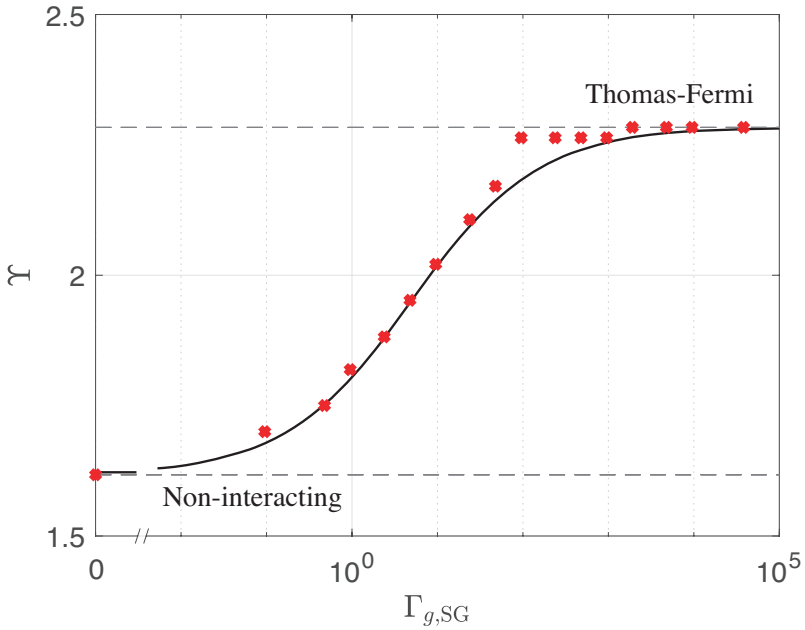

Figure 4.1: The curve of best fit, given by Eq. (4.15) (black) which fits best to numerical values for Υ (red), across a range of self interaction strengths, from non-interacting to deeply within the Thomas-Fermi regime.

well by the equation

$$\Upsilon(\Gamma_g) = \frac{\Upsilon_0 + \Upsilon_{TF}}{2} + \frac{\Upsilon_{TF} - \Upsilon_0}{2} \tanh\left(\frac{\log_{10}\Gamma_g - a}{b}\right). \tag{4.15}$$

Here, both a and b are of order unity as evident in FIG. 4.1, with $a = 0.6$ and $b = 1.5$.

FIG. 4.2 shows the results of overlaying the best SG fit over the ground state generated data. Though the fit does indeed become progressively worse towards the Thomas-Fermi regime, it is most accurate in the range $0.5 \leq \Gamma_g \leq 100$. This is the relevant range for the SPARC [1] observational data which we consider, as will be shown later. Even in the Thomas-Fermi regime, the peak density as well as the profile within $r < r_c$ are both well fit by the SG. It is clear that the SG profile provides an excellent fit in the non-interacting regime, and smoothly transitions into self interacting. It maps the parameters of the Thomas-Fermi profile (ρ_0, r_c) well, and replicates the flat shape of the inner part of the core, while remaining self consistent throughout.

Using all the above information, we have formed the basis for the generation of any arbitrary soliton profile given inputs m, M and g. This profile not only demonstrates an accurate variation in the relationship between r_c and ρ_0 as one traverses from the non-interacting regime to the Thomas-Fermi regime, but also critically exhibits a necessary change in the dimensionless soliton shape which depends on the input parameters parametrically through the dimensionless

self interaction parameter Γ_g. Although the tail of the SG soliton is unable to recreate the steep drop seen in numerically generated ground states found deep within the Thomas-Fermi regime, the inner part of the core is even in these cases mapped well.

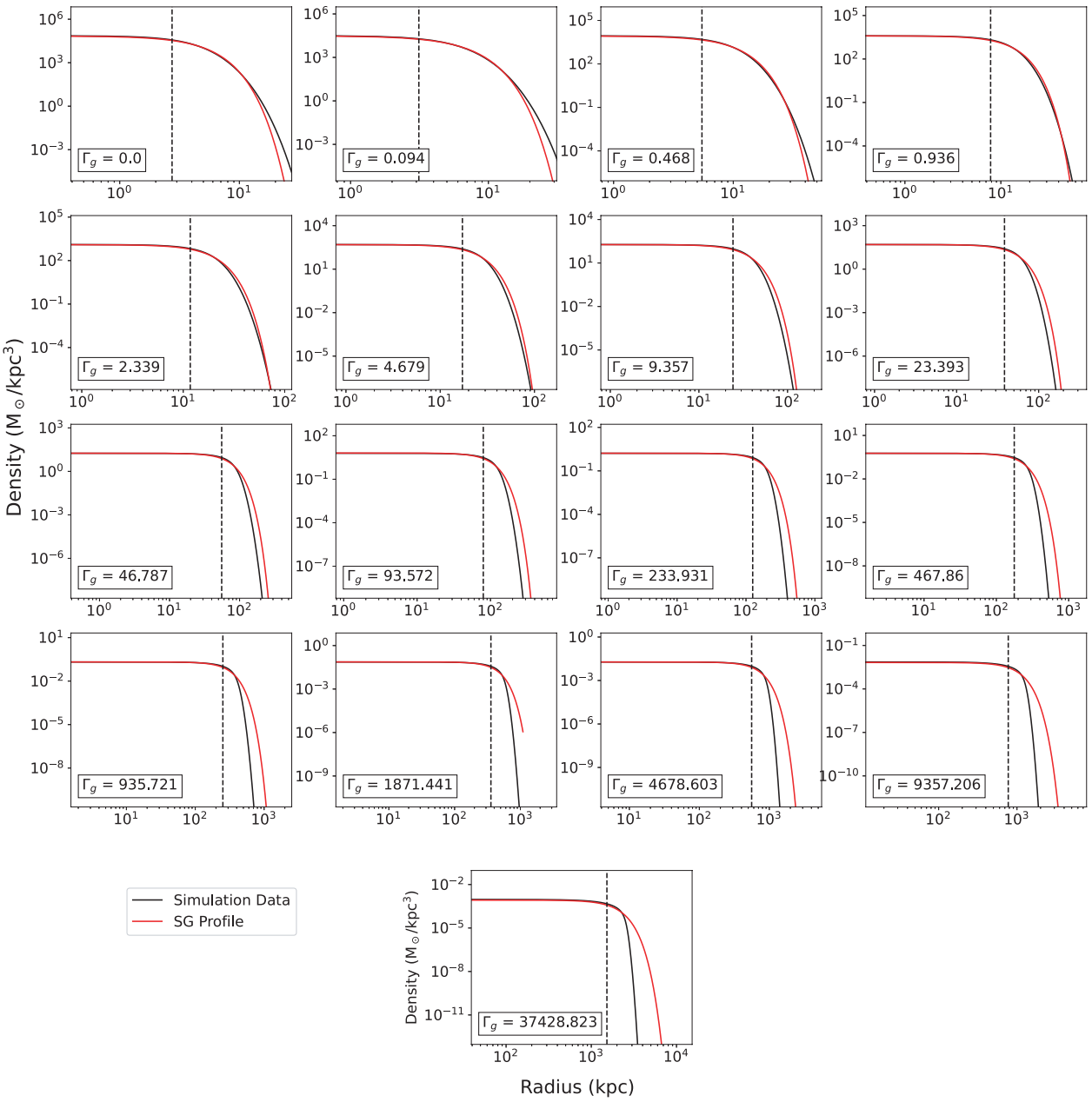

Figure 4.2: The SG profile fits (red) for each numerically generated ground state (black), obtained through imaginary time propagation for a variety of different dimensionless self interaction strengths. The black dotted line represents the core radius, r_c of our SG fit.

4.2 The SG-NFW Profile

The SG profile introduced in the previous chapter is a reliable profile that accurately models the core's transition from non-interacting to Thomas-Fermi as one increases the self-interaction strength. The halo, on the other hand, is historically modelled accurately using the NFW profile [20]. To formulate a bimodal profile with a smooth switch from the SG core to the NFW halo, we must characterise a transition radius at which this transfer will occur, which we henceforth refer to as r_t. Let us first introduce the NFW profile fully as

$$\rho_{\text{NFW}} = \rho_h \left(\frac{r_h}{r}\right) \left[1 + \frac{r}{r_h}\right]^{-2}, \tag{4.16}$$

where ρ_h and r_h are free parameters. The latter we will refer to as the *NFW scale radius*, and the former will be expressed in terms of other parameters in the next section. The full form of our bimodal SG-NFW profile is

$$\rho(r) = \Theta(r - r_t)\rho_{\text{SG}} + \Theta(r_t - r)\rho_{\text{NFW}}, \tag{4.17}$$

where Θ is the Heaviside step function. There is nothing inherently present in the above definitions which enforces that the transition between one profile to the other is continuous, though this is a necessity for a physically relevant profile.

4.2.1 The Continuity Condition

We impose the *continuity condition* on the profiles by asserting that the density at r_t for both the SG and the NFW profiles must be equal. That is to say,

$$\rho_h \left(\frac{r_h}{r_t}\right) \left[1 + \frac{r_t}{r_h}\right]^{-2} = \rho_0 \exp\left(-\ln 2 \left(\frac{r_t}{r_c}\right)^{\Upsilon}\right). \tag{4.18}$$

Rearranging the above for ρ_h removes a degree of freedom in the NFW halo, and yields the expression

$$\rho_h = \rho_0 \exp\left(-\ln 2 \left(\frac{r_t}{r_c}\right)^{\Upsilon}\right) \left(\frac{r_t}{r_h}\right) \left[1 + \frac{r_t}{r_h}\right]^{2}. \tag{4.19}$$

In doing so, we leave a single free parameter in the NFW profile, which in physical terms would likely be characterised by the energy of the system. Given that a larger r_h value results in a puffier halo which decreases to a $\rho \propto r^{-3}$ trend further from the centre, one might assume that r_h must somehow scale with energy, and that a more positive energy results in a larger r_h, though this is entirely speculative. However, if one knows the total mass of a system, and the

approximate mass of the core, then r_h loses the status of free parameter, as it is bound by the total mass of the system.

4.2.2 The Gradient Condition

Equally importantly as the continuity condition, one must consider another physically relevant aspect of the transition between profiles. In formulating the aforementioned bimodal profile, we have made the assertion that the soliton core is the ground state of the system, and that it must exist embedded inside a halo. In other words, the core is the ground state and the halo is an atmosphere of excited modes – the system cannot be bounded if there is no core present. By having a transition at r_t using the Heaviside step function, it mathematically seems that the transition is instantaneous and that the core 'vanishes' at this radius, however this is not acceptable in physical terms. Instead, the 1D core density profile will submerge below the NFW 'surface' at r_t. This tells us that the density profile for the ***halo*** is not explicitly the NFW profile, but rather

$$\rho_{\text{halo}}(r > r_t) = \rho_{\text{NFW}}(r > r_t) - \rho_{\text{SG}}(r > r_t). \tag{4.20}$$

This is due to the embedded core's contribution to the total density profile. For this to be fulfilled, we require that $\rho_{\text{SG}}(r > r_t) < \rho_{\text{NFW}}(r > r_t)$. If this condition is not met, then the profile of the core will be artificially cut off by the enforced transition to the NFW profile at r_t, resulting in a non-physical solution. Therefore, in addition to the continuity condition we create a necessary relationship between the radial derivatives of the profiles, enforcing

$$\left| \left[\frac{\partial \rho_{\text{SG}}}{\partial r} \right]_{r=r_t} \right| \geq \left[\frac{\partial \rho_{\text{NFW}}}{\partial r} \right]_{r=r_t}. \tag{4.21}$$

Following some rearrangement, and substituting the continuity condition in for ρ_h, we arrive at

$$r_c^{\Upsilon(\Gamma_g)} \leq \Upsilon(\Gamma_g) \ln 2 \frac{r_h + r_t}{r_h + 3r_t} r_t^{\Upsilon(\Gamma_g)}. \tag{4.22}$$

There exist three approximate limiting cases that we can consider here; $r_h \gg r_t$, $r_h \ll r_t$ and $r_h \approx r_t$. In this order, the resulting inequalities can be written as

$$r_h \gg r_t \quad : \quad r_t \geq \left(\frac{1}{\Upsilon(\Gamma_g) \ln 2} \right)^{1/\Upsilon(\Gamma_g)} r_c, \tag{4.23}$$

$$r_h \ll r_t \quad : \quad r_t \geq \left(\frac{3}{\Upsilon(\Gamma_g) \ln 2} \right)^{1/\Upsilon(\Gamma_g)} r_c, \tag{4.24}$$

$$r_h \approx r_t \quad : \quad r_t \geq \left(\frac{2}{\Upsilon(\Gamma_g) \ln 2} \right)^{1/\Upsilon(\Gamma_g)} r_c. \tag{4.25}$$

Given that in the limit $\Gamma_g \to 0, \Upsilon_0 = 1.62$, and in the Thomas-Fermi limit we have $\Upsilon_{\text{TF}} = 2.28$, the consequences on the multiplicative factor between r_c and r_t can be found in Table 4.1.

//	$r_h \gg r_t$	$r_h \ll r_t$	$r_h \approx r_t$
Υ_0	$r_t = 0.93 r_c$	$r_t = 1.83 r_c$	$r_t = 1.43 r_c$
Υ_{TF}	$r_t = 0.82 r_c$	$r_t = 1.32 r_c$	$r_t = 1.11 r_c$

Table 4.1: Results for the ranges that the ratio between r_h/r_c can take, depending on whether the SG-NFW profile is in the non-interacting regime, the interacting regime or the Thomas-Fermi regime, also dependent on the comparable size of r_h in relation to r_t.

Now that we are aware of both necessary conditions to create a physically meaningful approximate profile for self-interacting FDM, we may proceed with an analysis of the SPARC [1] dataset.

4.3 SPARC Dataset

The SPARC dataset [1] consists of 175 galaxies with varying stellar masses and levels of surface brightness. For our study, we follow the same selection of galaxies as [3], which focuses on 17 bulgeless galaxies dominated by dark matter. For the sake of simplicity, we assume that all mass in these galaxies is dark matter, though this is something that must be carefully reconsidered in future work.

Given the significance of the errorbars within the dataset, it is important to acknowledge that multiple possible curves may fit a single set of data corresponding to one galaxy - there is a range of possible density profiles which infer a velocity curve that fits the data well, sitting within the errorbars. Therefore we will assume that there exists a range of possible core and total halo masses which yield rotation curves that are consistent with observation.

To generate a fair selection criteria for our fitting, we first consider the distance of the caps of the error bars from the central points. The rotation curve data from the SPARC data set

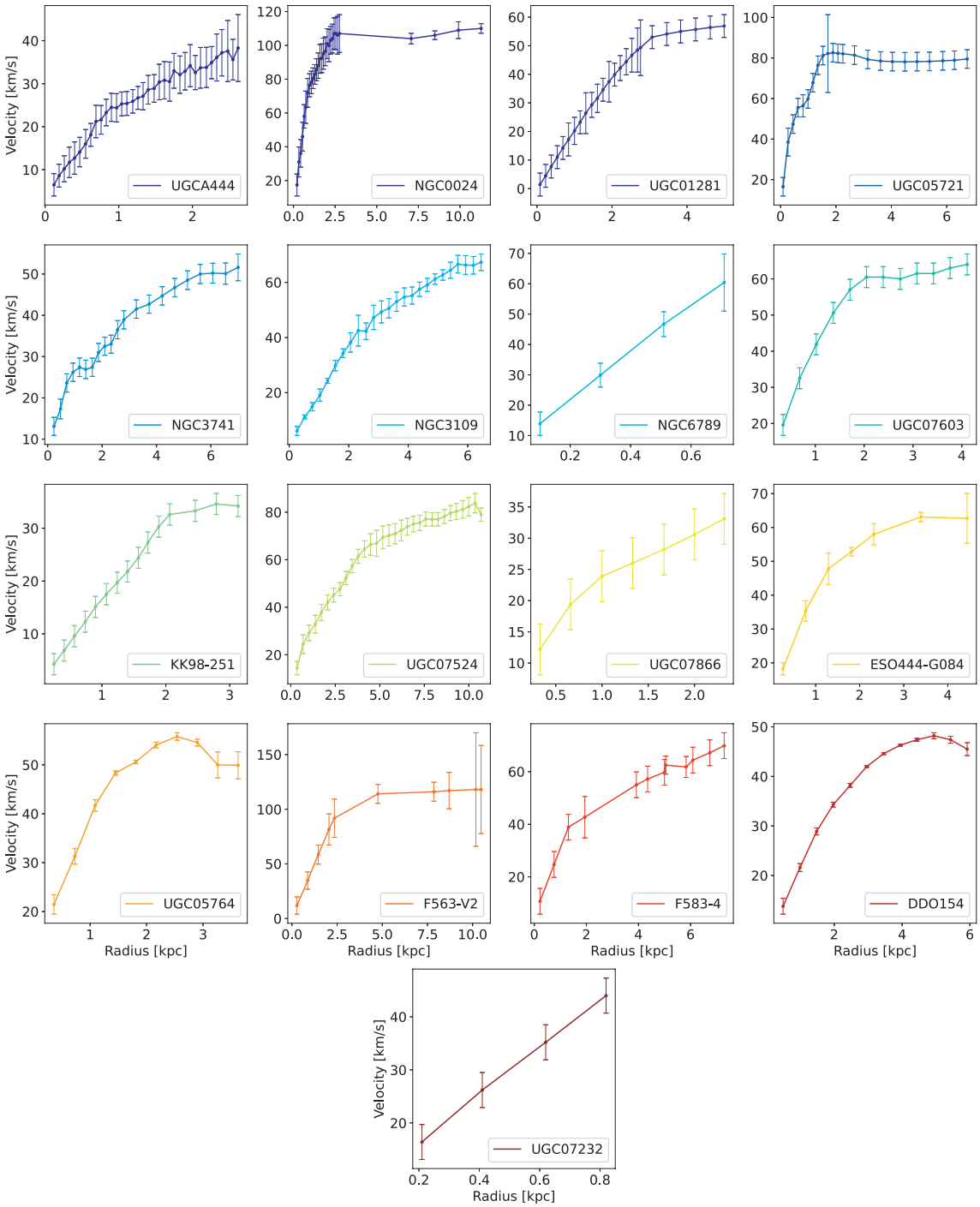

Figure 4.3: The observational data of the radial velocity curves taken from the galaxies chosen from the SPARC catalog, plotted with observational error bars. It is clear here that some galaxies have data points with minimal errorbars, while others have a much larger margin of error.

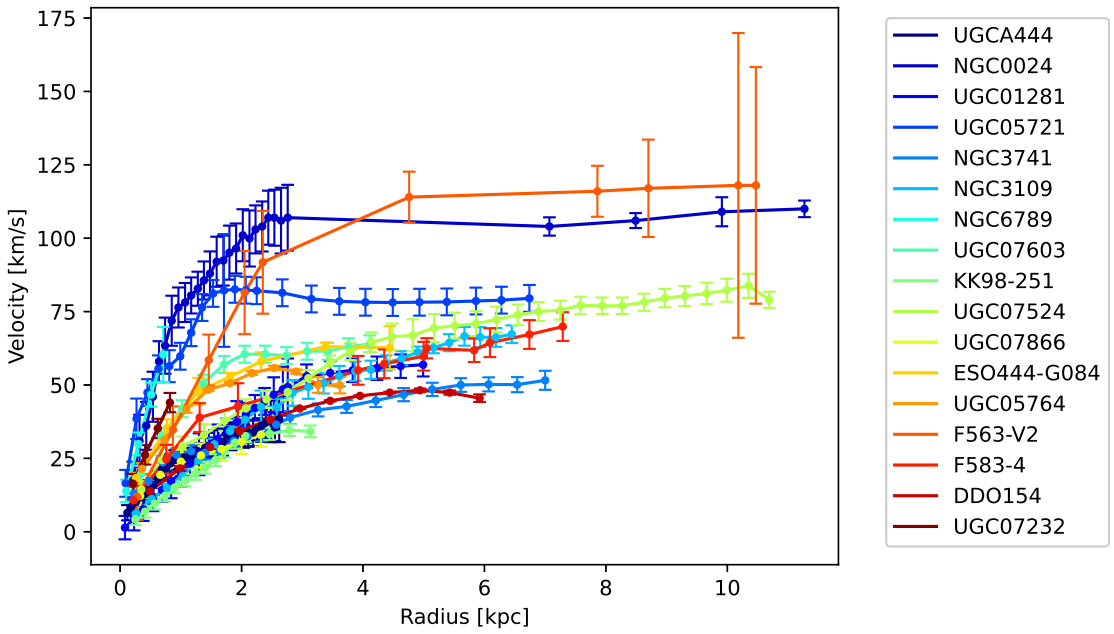

Figure 4.4: As in FIG. 4.3, all the selected galaxies from the SPARC catalog are plotted here on the same set of axes to show the variety of radii to which galaxies are sampled, as well as the range in maximum velocities across them.

is given as data points with a symmetric error, $(v_{\text{mid}} \pm v_{\text{err}})$. We compute the χ^2 between the values $v_{\text{mid}} + v_{\text{err}}$ and v for each galaxy to obtain a critical value of χ^2 which we deem acceptable for any subsequent fits to the data. Here, v_{mid} is the velocity of each data point, and v_{err} is the size of the error in the data. That is to say that for a given galaxy our maximum tolerable value for χ^2, giving us fits which are acceptable, is defined by

$$\chi^2_{\text{galaxy}} = \sum \frac{(v_{\text{mid}} - [v_{\text{mid}} + v_{\text{err}}])^2}{v_{\text{mid}}} = \sum \frac{(v_{\text{err}})^2}{v_{\text{mid}}} \tag{4.26}$$

In this case, we are stating that any curve which has a lower χ^2 value than the aggregate error of the observation is an adequate fit for further analysis. We term this 'Rule 1'.

However, in some cases data has negligible error bars, even if theoretical fitting curves which fit well exist, a good example being the galaxy DDO154 (see FIG. 4.5). In this case, one would need a *perfect* fit in order to be selected by Rule 1. Given the approximate nature of our method, this is impossible. In such cases, we instead refer to a secondary rule to select our acceptable curves: fitting curves which have a χ^2 value of less than $2\chi^2_{\text{min}}$ are selected, where $2\chi^2_{\text{min}}$ is the minimum χ^2 value we obtain across all attempted fits for a particular galaxy (so for any combination of parameters within our 5D parameter space). Therefore, to maintain

consistency and remove bias, we introduce a bimodal selection criteria where the maximum allowed χ^2 value is either:

- (*Rule 1:*) The computed χ^2 between the true midpoints and the error bars, χ^2_{err}
- (*Rule 2:*) Twice the minimum computed χ^2 value across all fits ($2\chi^2_{\text{min}}$).

Therefore, our selection criteria is given by

$$\chi_{\text{allowed}} = \begin{cases} \chi^2_{\text{err}} & \text{if } \chi^2_{\text{min}} < \chi^2_{\text{err}} \\ \\ 2\chi^2_{\text{min}} & \text{if } \chi^2_{\text{min}} > \chi^2_{\text{err}} \end{cases} . \tag{4.27}$$

Though *Rule 2* may seem somewhat arbitrary, it produces results which fit well, and we will soon show that *Rule 1* is utilised in almost all cases, while *Rule 2* only takes the larger value of χ^2 in the case of specific galaxies with very small errorbars. The insets within Fig. 4.5 shows this methodology for two galaxies, DDO154 and UGCA444 and is discussed further in the next section.

Finally, in our analysis we simplistically only consider the total radial velocity of the galaxies. Within this thesis, we do not consider the effect of baryonic components, as we aim to conduct a simplistic primary investigation into the validity of self interacting FDM and how it fares in observational comparisons. The chosen galaxies are low-luminosity galaxies dominated by dark matter, so such an assumption is valid at this level of study. A more complete study incorporating possible effects of coupling to baryonic matter falls outside the scope of this thesis, although we would not expect the inclusion of baryonic matter to have a significant effect for the particular galaxies studied here.

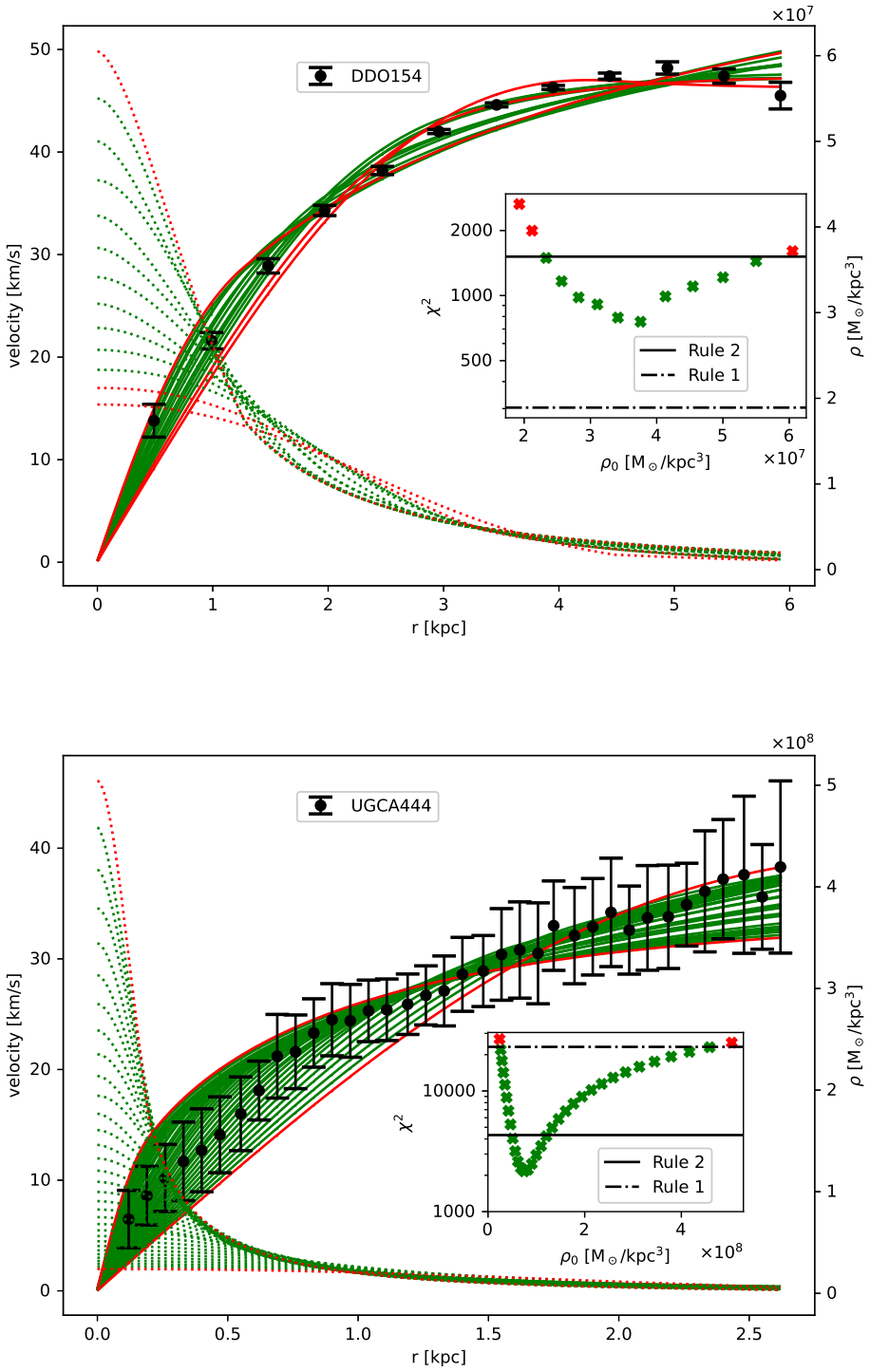

Figure 4.5: Two different galaxies (DDO154, UGCA444) demonstrating - (Main Plot) Left Axis: The observational velocity curve data with error bars (black points) plotted alongside the generated SG+NFW velocity curves (green/red lines). Curves which obey the selection rules are green, while the plotted red lines to not satisfy our selection criterion in Eq. (4.27). Right Axis: The density curves which form the aforementioned velocity curves, plotted as dotted lines. (Inset Plot) The computed values of χ^2 for the SG+NFW curves. The dash-dotted horizontal line shows the maximum χ^2 according to Rule 1, the solid horizontal line shows the maximum χ^2 value according to Rule 2, with green points corresponding to data fits passing our identified selection criterion.

4.4 Fitting Algorithm

4.4.1 Initial family of curves

It is important to reiterate the necessary parameters to ***ab initio*** generate a SG-NFW profile of a purely dark matter halo. For the definition of the core, in the absence of a halo, there are three necessary input parameters - the core mass M_c, the boson mass m and the self interaction strength g. With these, we can compute the core radius, r_c. The halo is then defined by a further two parameters, r_t, r_h. Using the gradient condition, we have already expressed a strict lower limit for r_t, while still expecting it to be of the order of r_c. Using these criteria, we significantly narrow the search range for these parameters. However, for r_h, one would consider that it is limited by the core-halo mass relation [25, 99, 100, 101], but due to the existing tension [99] in this relation we instead choose to leave r_h as a completely free parameter. Additionally, we also know that M_c can be expressed in terms of ρ_0, r_c and Γ_g, so we will choose ρ_0 as our free parameter here, as we can obtain an approximate initial guess for ρ_0 from the first data point of the velocity curve, as explained below in Eq. (4.28).

Summarised, the five necessary input parameters to generate a SG-NFW profile are: ρ_0, m, Γ_g, r_t, r_h. The method by which we fit is as follows:

- We guess an initial peak density according to

$$\rho_0^{\text{guess}} = \frac{1}{r_0^2}\frac{\partial}{\partial r}\left[\frac{r_0 v_0^2}{4\pi G}\right], \tag{4.28}$$

  where r_0 is the radius of the first observational velocity data point, and v_0 its velocity. This allows us to use the first observational point as an indicator for the approximate peak density, around which we will perform our grid-search. For each iteration, we fix this for our search across the remaining four parameters.

- Our range of boson masses across which we search is $10^{-23}\text{eV/c}^2 \leq m \leq 10^{-20}\text{eV/c}^2$. For each iteration of ρ_0, we fix this for our search across the remaining three parameters.

- The range of Γ_g we search across is $0 \leq \Gamma_g \leq 10^5$, which allows us to sample from the non-interacting regime into the Thomas-Fermi regime. For each iteration of ρ_0, m, we fix this for our search across the remaining two parameters.

- The transition radius has a lower limit as previously discussed, while the upper limit we place is $r_t \leq 3r_c$. A larger transition radius would only ever occur in isolated cores or

very low energy halos, which is not the case in this dataset.[1] These criteria define our search limits for r_t. For each iteration of of ρ_0, m, Γ_g, we fix this for our search across the remaining parameter.

- We regard r_h as a free parameter with a large range and a low resolution, finding that it has little impact on the final form of the velocity profiles at the radius ranges within which we have data. This will be discussed in more detail when we come to simulating the fitting profiles in chapter 5.

We begin our process for each galaxy by taking an initial guess for ρ_0 as detailed in the first step. This parameter is fixed, while we span the 4-dimensional parameter space for an ***ab initio*** density profile that provides the optimal inferred velocity curve. This curve is then attributed to the ρ_0 value and saved. We then multiply the ρ_0 value by a factor of 1.2, and repeat the process, traversing the ρ_0 parameter space. If the resulting χ^2 value of each iteration of this process is lower than the current minimum value for any ρ_0, we proceed to search in this direction of the ρ_0 parameter space. If, however, the resulting χ^2 value is greater, we instead return to the ρ_0 which provided the minimum current value of χ^2, and go in the other direction of the parameter space, dividing by 1.2. We do this until we have found the minimum χ^2 value. At this point, we then proceed to span the remaining ρ_0 space until we obtain χ^2 values which surpass whichever is larger of ***Rule 1*** or ***Rule 2***.[2]

Examples are illustrated in the insets of FIG. 4.5: Our fitting algorithm obtains multiple best fit curves, each one corresponding to a 'parent' ρ_0 value. Let us discuss the limiting curves for DDO154 first. At $\rho_0 \approx 6 \times 10^7 M_\odot/\text{kpc}^3$, we see that the best-fit curve has a χ^2 value greater than that which is allowed by Rule 2. Similarly, this is seen at $\rho_0 \approx 2 \times 10^7 M_\odot/\text{kpc}^3$. For UGCA444, at $\rho_0 \approx 5 \times 10^8 M_\odot/\text{kpc}^3$, the best-fit curve has a χ^2 value greater than what is allowed by Rule 1, as does the data point at $\rho_0 = 0.2 \times 10^8 M_\odot/\text{kpc}^3$. Therefore, for both cases with both galaxies, we no longer continue to search in either of these directions in the ρ_0 parameter space, and these limiting values (and all subsequent values outside the selection criteria) are also omitted from further analysis. On the other hand, all allowed points which pass the selection criteria are clearly plotted in green, and are found under the larger of the two horizontal lines.

After completely spanning the entire 5-dimensional space for each galaxy and omitting results beyond our allowed selection criteria, we are left with multiple parameter sets which

[1] The impact of the energy on the core-halo relation is discussed, simulated and analysed in detail in the next chapter.

[2] An initial verification that the span across the ρ_0 space is large enough is important to assert the completeness of the data, confirming that the boundaries of the selection zone on both sides of the χ^2 minimum are spanned by the fitting data, as can be seen in the insets of Fig. 4.5

correspond to density curves with different soliton (and total) masses, whose inferred velocity curves fit well to observational data. We visualise two cases in Fig. 4.5 - DDO154 and UGCA444.

4.4.2 Exploiting parameter degeneracies

We have previously shown that a soliton core of fixed total mass and some fixed pair of ρ_0 and r_c can exist as a result of a range of m and g pairs, where the choice of (m, g) pair affects the dimensionless shape of the soliton at $r < r_c$ and $r > r_c$; the peak density and the half-maximum have the same coordinates in the (ρ, r) space and remain fixed. We can exploit this to extrapolate additional results that will *also* fit to the observational data, using the fact that each generated profile belongs to a degeneracy curve.

For each galaxy, we consider the set of the profiles which are allowed according to our selection criteria, and assume the core-region is well fit by any set of m and g parameters along the degeneracy curve to which the initial profiles belong. Specifically, we compute the degeneracy curve according to

$$m(\Gamma_g) = \left[\frac{\sigma}{\nu\eta}\frac{\hbar^2}{4\pi G\rho_0 r_c^4}\left(1+\sqrt{1+15\frac{\sigma_0^2\zeta\nu}{\sigma^2\zeta_0\nu_0}\Gamma_g}\right)\right]^{1/2} \tag{4.29}$$

where ρ_0 and r_c are the values obtained from the fit. We can freely go between g and Γ_g using the formula for g_* in Eq. (3.15). We find in most cases that boson masses across $1-3$ orders of magnitude are allowed for each galaxy, with Γ_g changing accordingly. For consistency, we only take results where $0 \leq \Gamma_g \leq 10^5$ to remain within our initial search range. However, in some cases, a large change in the shape of the core as a result of travelling along a degeneracy curve in the $m-g$ parameter space can significantly alter the outer regions of the velocity curve. Therefore, for each velocity profile generated by the parameter combination of m and g for each discretised point on the degeneracy curve, we compute the corresponding χ^2 value between itself and observational data, and verify it too obeys the selection rules for the galaxy in question.

The result is a stack of curves in different $m-g$ planes, where each plane corresponds to a different core peak density, which can be parameterised through the soliton mass. This can be described as a 3 dimensional space consisting of (ρ_0, m, g). An illustration of this is visible in FIG. 4.6, in which we show that individual $m-g$ curves can be projected onto a single plane. This single plane hosts all the possible $m-g$ points which fit well to any of the given SPARC galaxies. By projecting all fitting curves from all galaxies onto a single plane, we are left with a 2D space in which all points correspond to a boson mass and self interaction strength pair which can be used to construct at least one core-halo profile whose

inferred velocity curve fits well to the observational data. Importantly, we note here that the more intersecting degeneracy curves are located at a point, the more likely the corresponding $m - g$ pair is able to reconstruct multiple core-halo profiles, each of which match to a different galaxy. FIG. 4.6 shows a qualitative projection of three curves and how they may appear on the projection plane. In reality, there are many curves per galaxy with clear favourable $m - g$ zones in the plane. Therefore, it is now crucial to identify the region in the $m - g$ plane which most agrees with observational data.

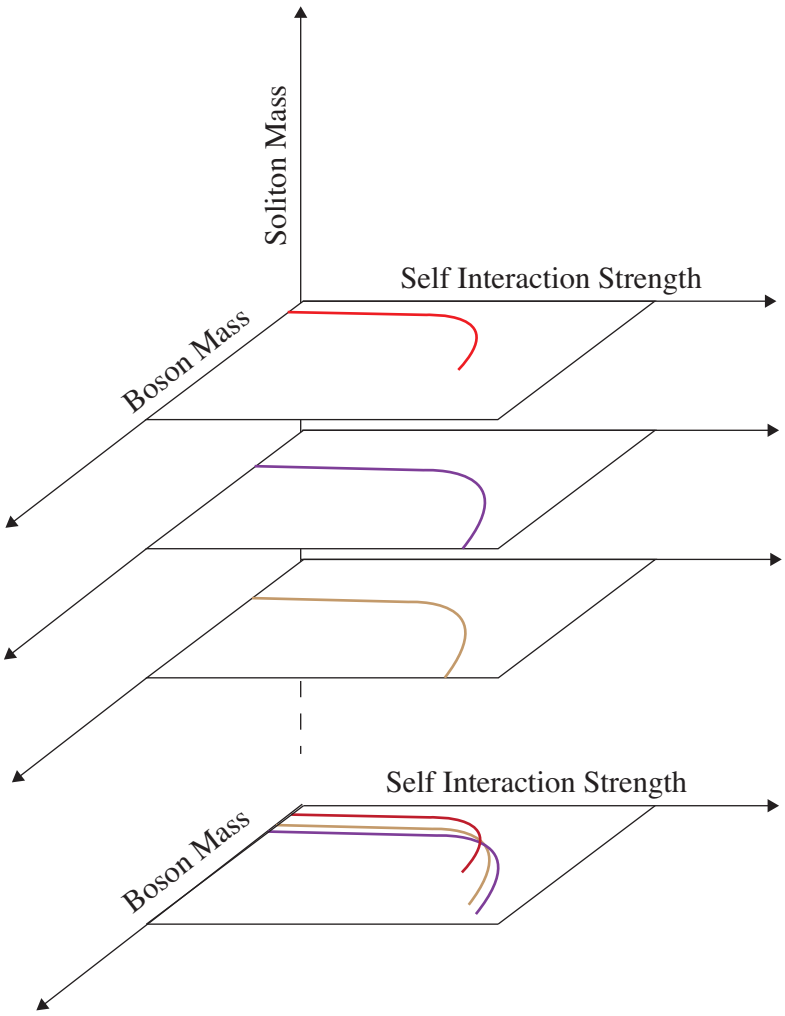

Figure 4.6: A qualitative demonstration of how individual curves on $m - g$ planes, corresponding to different soliton masses, can be projected onto a single plane to identify all the possible boson mass-self interaction strength pairs which fit well to a given galaxy in the SPARC database. Each curve corresponds to a different peak density curve which fits to one galaxy, for which a range of m and g return the very same ρ_0 and r_c. For each galaxy, a set of such planes exist which can later be collapsed into a singular plot.

When all $m - g$ degeneracy curves are compiled onto a single plane, we convert the data to a density-of-points representation by applying a normalised Gaussian kernel density estimation (KDE). This converts each data point to a value which reflects the density and adjacency of neighbouring points in the $m - g$ space. The information of the point density is reflected in a colour gradient, resulting in a heat map. The density value at a $m - g$ location of the heat map can be interpreted as the likelihood of such a pair fitting well to the complete set of 17 galaxies. We may say that the maximum point in the heat map indicates the locus of the greatest bundling of points corresponding to well-fitting SG-NFW curves, and therefore indicates the highest probability that parameter pairs at this location will yield profiles that are of interest for further testing with additional data.

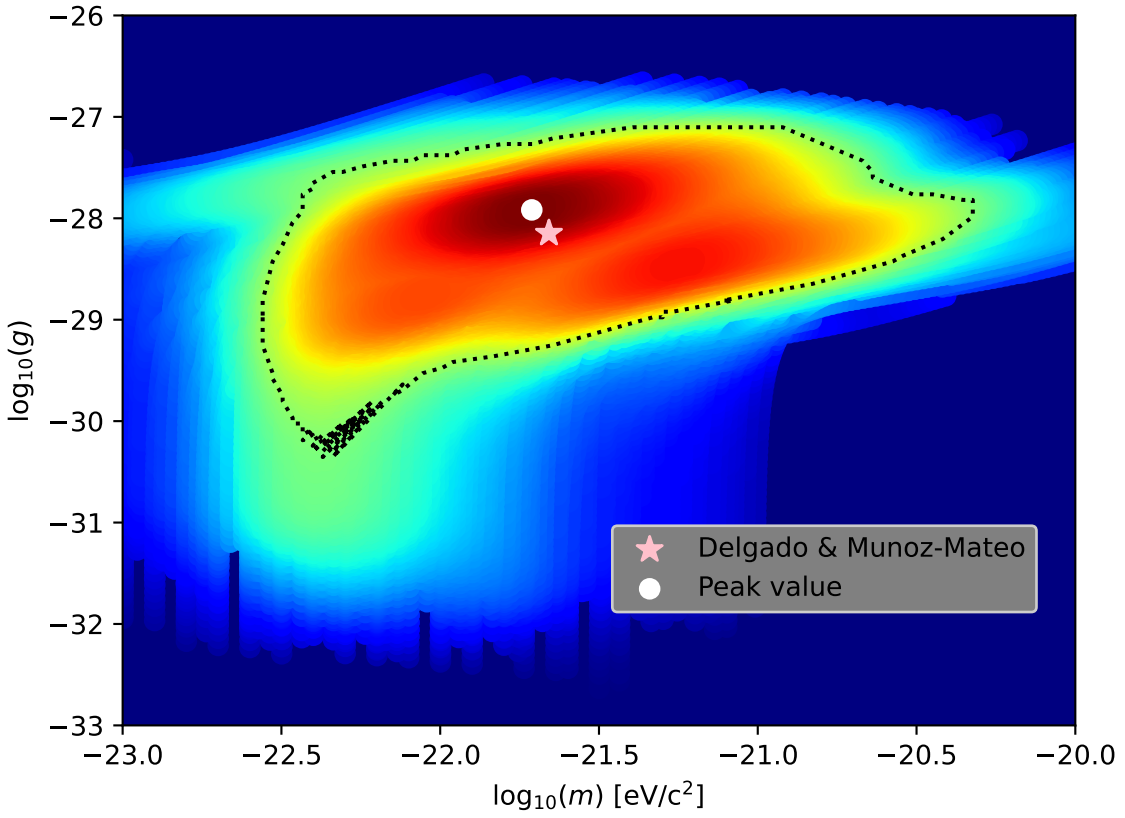

Figure 4.7: A qualitative demonstration of how individual curves on $m - g$ planes, corresponding to different soliton masses, can be projected onto a single plane to identify all the possible boson mass-self interaction strength pairs which fit well to a given galaxy in the SPARC database. A background grid of data points has been overlaid with 0 values corresponding to dark blue colour for aesthetic purposes. There are no natural data points in this filled region. The white point represents the peak point in this work, while the pink point represents the $m - g$ pair obtained in [3].

This heat map is displayed in FIG. 4.7. The white circle indicates the peak location, corresponding to $m = 1.94 \times 10^{-22}$ eV/c^2 and $g = 1.21 \times 10^{-28}$ Jm^3/kg, while the pink star represents the $m - g$ pairing found in [3] from their Gaussian fitting to the cores of these galaxies. Finally, the dotted black line indicates the density values which correspond to half the value of the peak density of points (white point); this is used as an indication for the region in the $m - g$ space which corresponds to well-fitting SG-NFW curves. If the heatmap point-values were well-fit by a 2D Gaussian distribution, this would equate to the 1σ boundary. It is interesting to note the level of agreement between our results and those of [3], demonstrating the robustness of the approach and the clear suggestion by two separate methods and fitting profiles that self-interaction is necessary if we wish for FDM to fit to this particular observational dataset.

4.4.3 Final Fit

In order to indicate our arising fit to the rotation curves for all 17 SPARC galaxies, we fix m and g to the optimally selected (m, g) pair value given by the peak (white circle in FIG. 4.7) of the heat map - $m = 1.94 \times 10^{-22}$ eV/c^2 and $g = 1.21 \times 10^{-28}$ Jm^3/kg. We then increase the resolution of the grid search for the remaining parameters, noting that we only have to search over the remaining three parameters, ρ_0, r_t and r_h. We obtain the optimal density profiles and their resultant velocity curves by finding the minimum χ^2, and plot them with their relevant observational datasets in FIG. 4.8.

It is important now to clarify that r_h is chosen to obtain the best possible fit, however a broad range of r_h values still produce velocity curves that sit within the confines of the errorbars.

We note that in *all* cases, the magnitudes of the velocity are correct. Some galaxies, for example UGC05721 and F583-4, are fit almost perfect aside from minor oscillatory behaviours in the data. However, some best fit velocity curves have notable deviations from the observational data for some galaxies, *e.g.* UGC01281, NGC3109 and KK98-251. We therefore arrive at the following conclusion: using the semi-analytical SG-NFW profile to fit the entire range of data for our selected galaxies from the SPARC catalog, we obtain a unique construction of m and g values which fit remarkably well to almost all but a few galaxies. Even these less positive cases, the SG-NFW profile still follow both the approximate shape and the magnitude of velocity of the observational data.

A natural next step, lying beyond the scope of this thesis, would be to introduce baryonic components to the velocity curves from the observational data, while simultaneously conducting a deeper analysis into the validity of the observational data. For example, are all galaxies well isolated in the sky? Are they uniformly rotating or are they passing through a denser medium

in which case the rotational data may be skewed?[3] Answering these questions and conducting a more detailed analysis of the results, as well as expanding to further catalogs will likely yield a more complete conclusion regarding the validity of self-interacting FDM. Importantly, we note that previous attempts in literature to fit non-interacting FDM to observational data have encountered similar issues. In particular, a single boson mass will not allow the formation of core-halo pairs which fit well to multiple galaxies, particularly in the instance of the SPARC dataset [65]. That is to say, a different boson mass is required for each galaxy within the context of the original (non-interacting) FDM. Importantly, we have shown here that the introduction of self-interactions removes such an issue.

Furthermore, we have pointed not only towards a single set of values of m and g which are appropriate, but rather to an entire confidence region which is worth considering for further work. This should guide investigations on the topic by providing a narrower search zone in which to probe the systems and observational data.

[3] According to [102], NGC3109 is a warped galaxy owing to a previous interaction with the Antlia Dwarf galaxy in the past. Similarly, [103] states that UGC01281 is also likely warped.

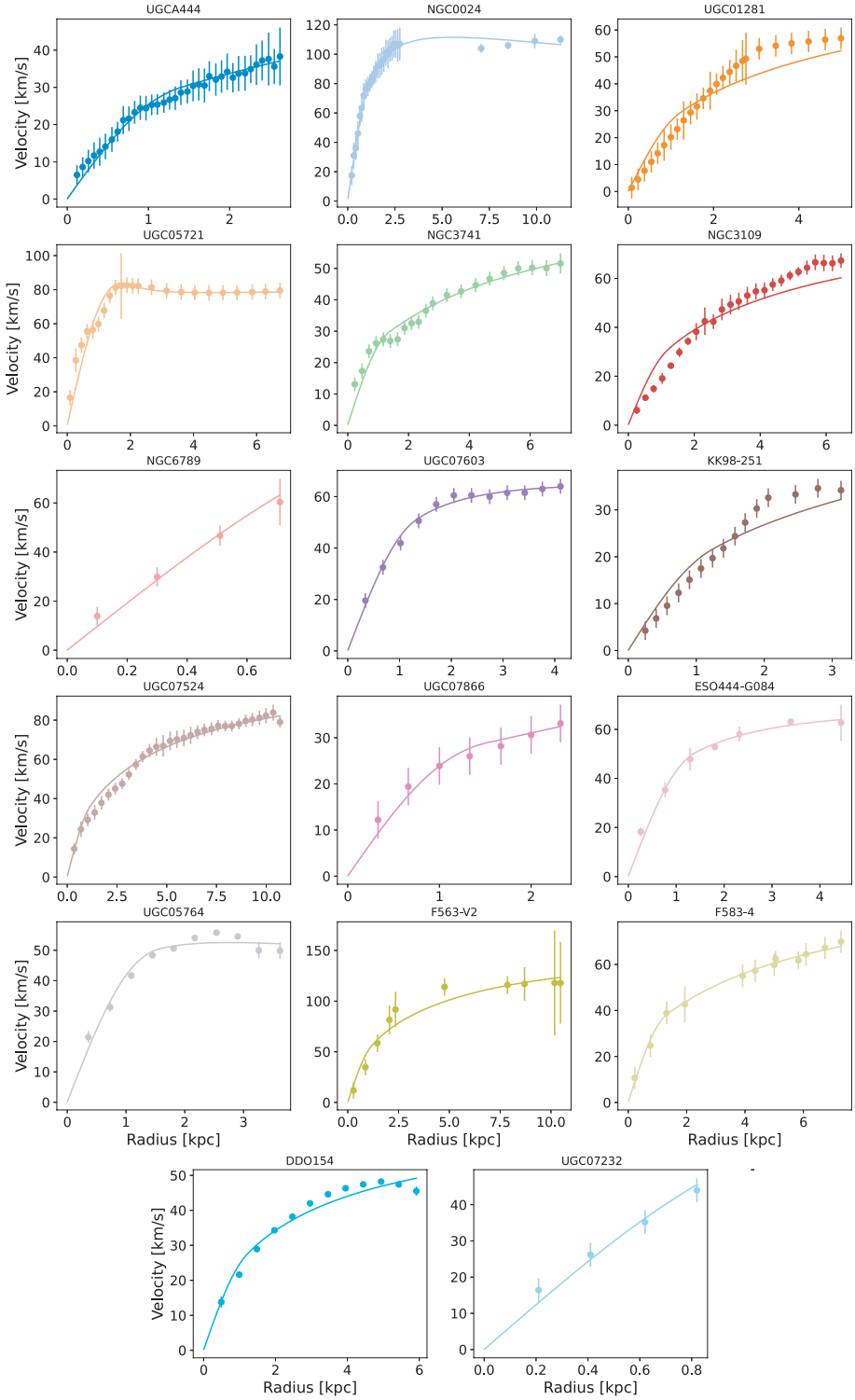

Figure 4.8: The final fitting results using our optimally identified values of FIG. 4.7, namely $m = 1.94 \times 10^{-22}$ eV/c^2 and $g = 1.21 \times 10^{-28}$ for each individual galaxy from our selection within the SPARC catalog.

5

Simulated Solitons and Halos

Thus far, only one piece of literature has targeted the reconstruction of known galaxies via the attempted replication of observational signatures [69]. This is an avenue which could lead to a renaissance of new FDM observational signatures to search for in our Universe.

In this chapter, we will develop a deeper understanding of the characteristics of a self interacting FDM core-halo system. We will then make use of this, as well as tools developed in chapters 3 and 4 to numerically reconstruct a target density profile whose inferred velocity curve agrees well with observational data. To do this, we make use of our optimal (m, g) pair from the previous chapter, as well as the extrapolation of the 1D best fit density profiles for the specific galaxy UGCA444. We choose our optimal boson mass and self interaction strength from FIG. 4.7. Following this, one of our primary assumptions when reconstructing a target profile is that the total energy of the system is the moderating factor of the distribution of mass between the core and the halo. That is to say, the total energy of the system is what defines the core-halo relation for a chosen m and g. The effects of the periodic box are briefly explored in this chapter, a concept that has been studied extensively in [104].

Therefore, for the first time in the literature, this chapter presents a method to dynamically reconstruct 3D target core-halo systems which correspond directly to fits to observational data. The importance of the total energy of the system, with respect to the total system ground state energy, is discussed and the implications on the final state are emphasised. Particularly, an

in-depth investigation from dynamical simulations on the distribution of mass between core and halo is presented, with an elegant and simple formula empirically stated which expresses the effects of energy on this mass allocation.

5.1 Simulation Set-Up

5.1.1 Initial Conditions

To simulate target core-halo systems of a desired total energy, we must have some element of control over the initial configurations of the simulation. To do this, we consider multiple Gaussian spheres of equal radii, allocated randomly within a cube which is centred within the large computational box. The Gaussians are placed such that the final centre of mass is the approximate centre of the computational box. We choose a smaller cube such that the Gaussian spheres are a good distance away from the computational box boundary, minimising unwanted effects from the periodic boundary conditions. This cube typically takes sides of length $\leq 0.75L$, where L is the length of the large computational box, an example of this computational cube is seen as the white square in FIG. 5.1. The radius of these Gaussian spheres is predetermined in the initial condition set-up, as is the total mass of the system. A catalog of such initial conditions is then generated and the energy of each is analysed. We select an initial condition from the catalog corresponding to the target energies we wish to have for our simulation, as we do not have direct control over the energy of the system without imaginary time propagation, which itself can lead to lack of control of other aspects.

To control the total energy of the system without artificially inducing a velocity vector field over the box, which may lead to instability and significant shifting of the final centre of mass from the centre of the box closer to one of the periodic boundaries, we instead control the radius of the initial Gaussian spheres by tuning two parameters: the radius per sphere and the size of the inner cube within which we put the Gaussians. An increase in Gaussian radius serves to reduce the total energy of the system, as it results in less compressed cores which exhibit less of an outwards pressure via the self-interaction and quantum pressure. On the other hand, a smaller inner computational cube makes the mass more localised, which results in a more negative total energy. However, given our assumption that the total energy is the relevant parameter for the configuration, we do not need to consider the allocations of positive energies among the components (quantum kinetic, self interacting). Instead, we regard all positive contributions to the energy as a single entity, expecting the energy to redistribute among all components adequately as we propagate the system.

This gives us a firm handle on the range of energies that will be generated by the catalog, but smaller and more subtle differences must be achieved through random generation and differing

initial configurations of the placement of Gaussian spheres. This is a quick numerical process and a large catalog can be generated and analysed rapidly with little computational resources. An alternative to this system is the stacking of eigenmodes to reach a target halo [75, 84]. Although this method takes significantly longer to generate the final system, it gives better control of the final parameters of the halo, despite the fact that the final equilibrium solutions, once dynamically propagated, appear to be unstable and will change dynamically via growth of the core. The approach of stacking eigenmodes (or similar) is taken by [75, 84, ?].

5.1.2 Reference Ground State Energy

As mentioned previously in this thesis, our fundamental assumption when constructing FDM core-halo systems is that the system is simply a superposition of ground and excited states. Taking a core-halo system and cooling it completely down will yield a singular soliton, which is the reference ground state we will discuss from here onwards, whose energy we term E_0. We compute this reference soliton using the SG profile, where our input mass is the total mass of the system, and analytically calculate the energies Θ_Q, W, U, noting that the soliton is in equilibrium and has no classical kinetic energy.

Turning back to the core-halo system, we know that it must have a total negative energy ranging between the ground state energy of the reference soliton, $E = E_0$, and $E = 0$ in order to remain bounded.

To verify the validity of our simulations, we must consider both the conservation of mass and the conservation of energy. In all our simulations, mass conservation is confirmed within one part in 10^7, though at first glance, energy conservation proves troublesome. For low energy simulations in which the system is close to the ground state configuration, total energy drift is minimal and kept below 1%. However, for simulations in which the various energy components collude in such a way that the total energy is close to 0 (high energy halos), the dimensionless simulation energy drift can be in excess of 50% across the whole simulated timeline of the age of the universe. To examine the effects of this energy drift, we take an initial condition and propagate it with four various multiplicative factors of the timestep which is otherwise computer from Eq. (2.32). For the main simulation presented in section 5.6, the multiplicative factor we use is 0.1, such that the timestep is equal to $0.1\Delta t$, with Δt computed as mentioned from Eq. (2.32). For this investigation, however, we choose the factors $(0.01, 0.025, 0.05, 0.1)\Delta t$, covering an adequate variety of timestep scaling. The results are as expected and can be found in FIG. 5.3, with $0.1\Delta t$ corresponding to an approximately 10% energy drift across 4 Gyr, and the smaller timesteps corresponding to a reduction in energy drift. However, an important question to answer here is what are the effects of such an energy drift? We know the drift

comes from numerical error in the summation of very large numbers[1], but we must verify the effects on the density profile since it is the density profile that we study for the remainder of this chapter, and the following one. The results are conclusive and shown in FIG. 5.3 (right), where even an energy drift difference of a factor of 10 still yields the exact same time averaged density profile across 4 Gyr. For this reason, we maintain the usage of larger timesteps to allow for the generation of a larger catalog of numerical results with the knowledge that the numerical side effects of such a timestep are, at most, negligible for the data we wish to analyse.

We henceforth scale energies typically by the ground state reference energy E_0, unless explicitly stated otherwise. This means that all energy changes are computed by referring to the reference ground state energy, E_0, of the system. Therefore, our energy drift is computed as

$$\Delta E = \frac{|E_{\text{init}} - E_{\text{fin}}|}{E_0}, \tag{5.1}$$

where E_{init} is the initial energy of the system upon generation of the initial condition, and E_{fin} is the final energy of the system. We frame the energy in terms of the ground state reference energy due to the belief that E/E_0 is the important parameter in all cases.

To consider the effects of the boundary condition on the final configuration of the system, we look at our energy scaling relation which we repeat here for convenience,

$$E_{\text{ref}} = \frac{N\hbar\sqrt{(G\rho_{\text{ref}})}}{L'^3} \tag{5.2}$$

where L' is the dimensionless length of the side of the computational box. Therefore, as we increase the length of the computational box, we increase the magnitude of E_0/E_{ref}. This allows a larger zone of E-space to be probed before our system becomes unbounded and the total energy crosses above 0. In fact, one can say that with a larger box, we increase the resolution of the energy range between $E_{\text{G,ref}}$ and $E = 0$. If we are to consider this from a physical standpoint rather than a purely mathematical one, we can consider the fact that for the same distribution of mass, a larger computational box with periodic boundary conditions will allow for the mass to spread out to a larger radius while the system continues to remains bounded. Since the increase of energy serves to increase the puffiness of the halo, and therefore the radius to which non-negligible densities extend, while decreasing the mass of the core, it becomes clear that one requires a larger computational box to probe higher energy configurations without the artificial effects of the enclosure of the boundaries leading to a positive total energy.

[1]The absolute magnitude of the individual energy components is approximately 2 orders of magnitude larger than the total energy of the system.

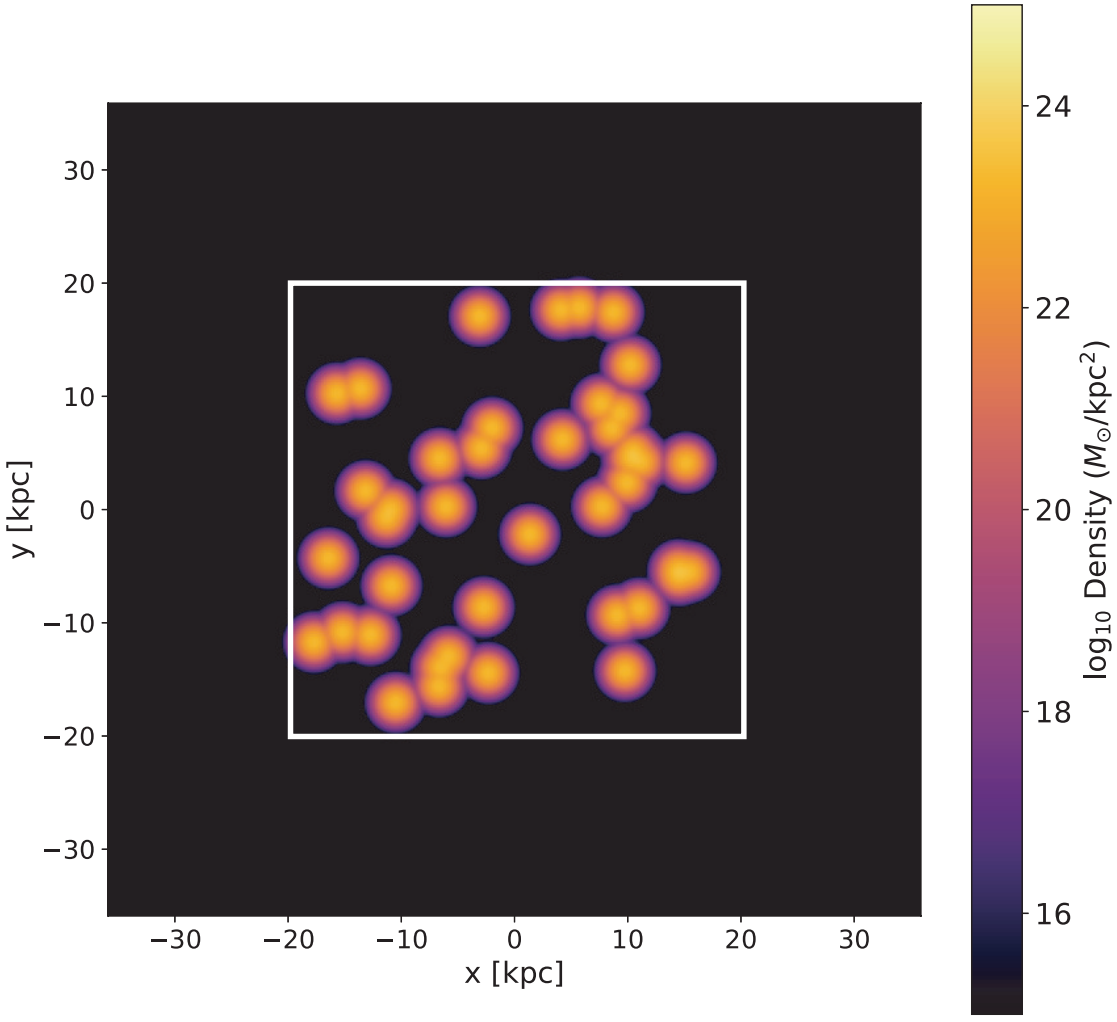

Figure 5.1: An integrated projection plot of the whole computational box, showing the initial conditions of a 3D simulation. A number of Gaussians are initiated in such a way that the centre of mass is in the middle of the box, and such that the total energy of the system is approximately the energy we desire. The smaller cube, shown in white, defines the domain within which we place Gaussians to avoid interference from the periodic boundary conditions when the simulation is propagated dynamically.

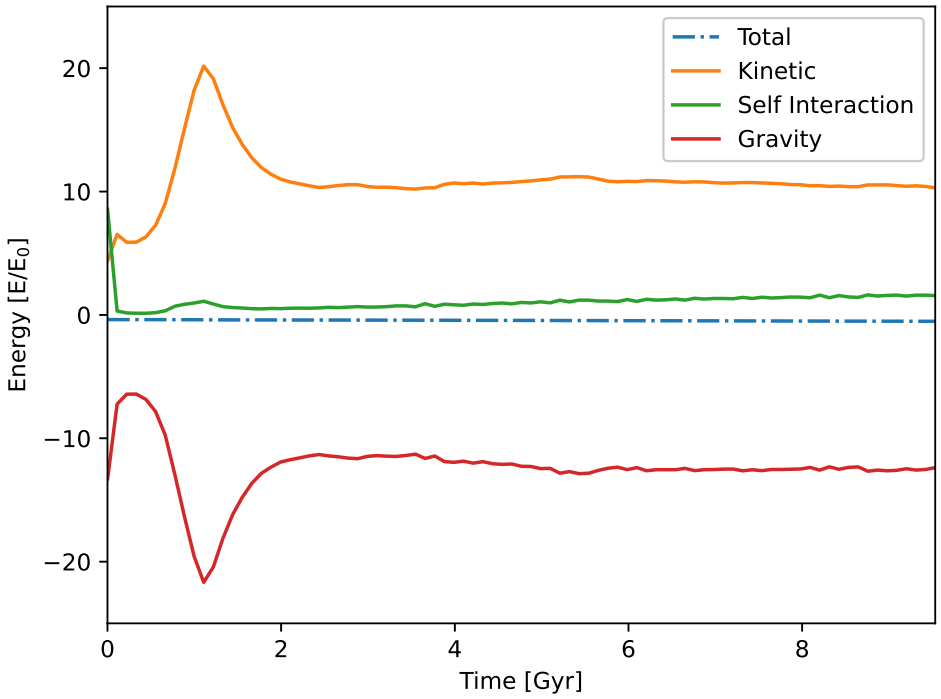

Figure 5.2: The various energy components for the propagation of the system seen in Fig. 5.1. The peak in energy components represents the initial collapse, followed by the formation of the core-halo structure shortly after. Energy is scaled by the reference ground state energy, E_0, and the total energy is conserved within the system.

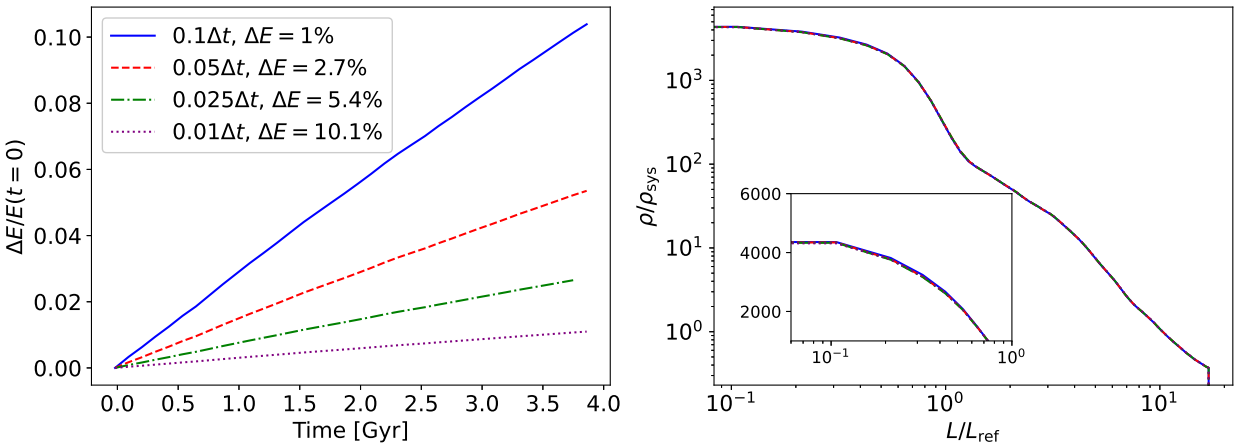

Figure 5.3: (Left) The energy drift for simulations with the same initial conditions, but propagated with various timesteps. Δt in this case is computed from the stability condition in Eq. (2.32) in chapter 2. (Right) The time averaged density profiles across all 4 Gyr for the four profiles. The inset shows a zoom in of the core to highlight that the profiles are identical on any relevant scale.

5.2 Analysing Simulation Results

Our system uses several initial Gaussians with radius smaller than their desired equilibrium. The outwards pressure from the self interaction and quantum pressure of these compressed Gaussians provides us the positive components of energy necessary, which later convert to classical kinetic energy. Since we are reliant on such a method to introduce positive components of energy, rather than applying classical kinetic energy via a phase initially, we cannot consider relevant the total simulation time. This is due to the fact that these initial conditions are not alike to cosmological initial conditions, and times taken for soliton formation and initial halo evolution and stabilisation will differ greatly from what may be physically relevant in our Universe. For this reason, we may only realistically refer to timescales once a stable halo and core has already formed. However, there is one crucial factor that we find in our simulations; the core continues to grow at timescales significantly longer than the age of the universe, as seen in other relevant pieces of work [75, 69]; this will be discussed in detail in chapter 6, and we will present repercussions, evidence, analysis and discussion for the next chapter where we explore dynamical evolution of FDM halos.

The 1D Profile

In order to convert our results to data that is comparable and relevant to observational data, we instead wish to refer to the 1D radial density profile, and the resultant velocity curve. To do this, it is first necessary to assert that the peak density, and therefore the centre of the symmetrical core, is found in the middle of the computational box. Since it is unlikely that this is generally the case, we always take advantage of the periodic boundary conditions to roll the background grid's position to place the peak density at $\mathbf{r} = (0, 0, 0)$. This essentially means that the grid 'follows' the core as it conducts a random walk, and that our zero-point is always the peak of the core. We then take the average density value at each spherical shell from $r = 0$ to $r = L$, where L is the size of the computational box. The resultant profile is a shell-averaged radial density profile which 'forgets' aspects of granularity within the halo.[2] An example of a snapshot of a 3D simulation, and the corresponding radial profile from this timestep, is given in FIG. 5.4. The granularity is evident in the integrated projection (left), while it is clear that most effects are averaged out in the radial profile (right). Some wave-like effects are still noticeable in the radial profile, though they are insignificant in comparison to the true granularity of the 3D profile. Another important fact to note is that the corners of the computational box are not taken into account as being part of the halo. Specifically, to largest radial shell of our shell averaged profile

[2] We note that these are crucial aspects of the FDM paradigm, and therefore will be discussed in-depth in the next chapter with a specific emphasis on their effects on the velocity of test particles. They will also be shown in brief in a later section within this chapter, though no quantitative analysis has been conducted.

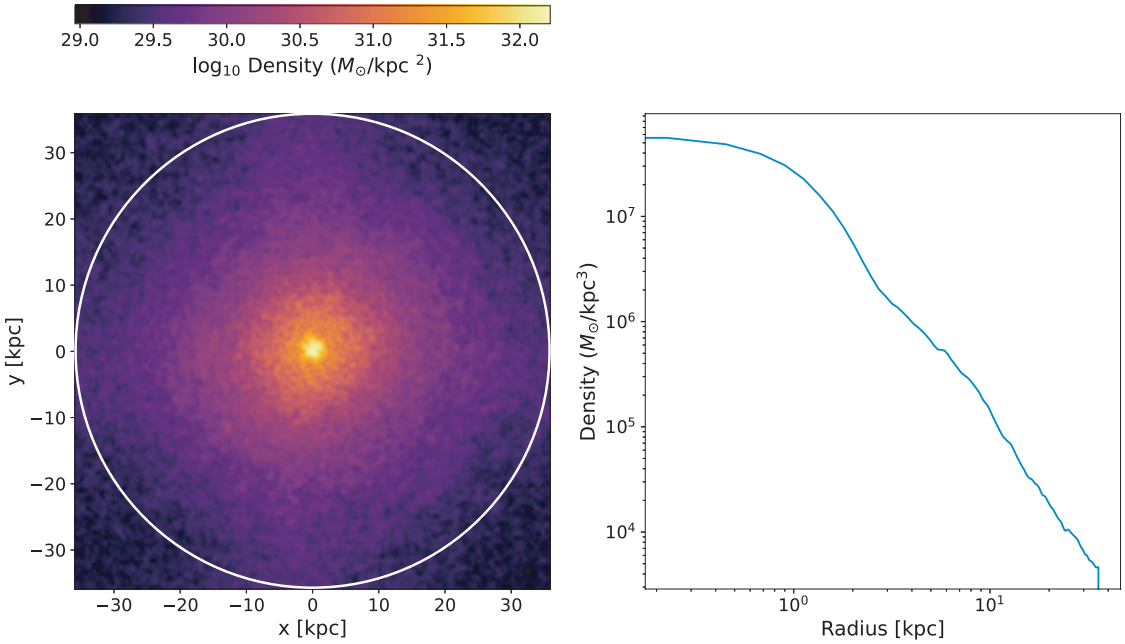

Figure 5.4: (Left) A 2D projection plot, integrated along the z-axis, of a snapshot from an arbitrarily chosen 3D simulation. Here, the total mass of the simulation is 240 M_{ref}. A clear, definable core is seen in the centre, embedded within the FDM halo with its signature granularity clearly evident. (Right) The 1D radial density profile, taken from the shell averaged density at each radius. It is important to note that the corners of the box, which are not included in the sphere (depicted here as a white circle in 2D), are not captured in this 1D profile.

does not include the corners of the computational box. This sphere is represented by a white circle in FIG. 5.4. Mass that arrives here is ignored for further analysis, and therefore the total mass of the halo will always be less than or equal to the mass of the entire computational box. In fact, in the next chapter, we will discuss how mass is ejected into this region as a form of system cooling.

The radial profile always shows a distinct and ordered core which then transitions into an NFW-like profile. This profile can be well fit by the SG-NFW profiles discussed in the previous chapter. To retrieve a velocity curve from a 1D density profile, we compute

$$v(r) = \sqrt{\frac{GM(r)}{r}}, \tag{5.3}$$

in which M is a spherically symmetric mass distribution and $M(r)$ is the spherical integral of the density up to radius r, giving us the mass enclosed within this shell.

5.3 Core-Halo Relationship

We continue under the hypothesis that for a fixed boson mass and self interaction strength, the only governing parameter which defines the allocation of a system's mass between the core and the halo is the total energy of the system. The distribution of this energy among corresponding components is presumed to be unimportant, as we expect the final state of the system at $t = \infty$ to be virialised, which–given energy and mass conservation–pins the energy distribution among the components. We choose to forego this assumption regarding virialisation due to the dynamical evolution of the core on long time scales, as discussed in the next chapter.

We select a boson mass-self interaction pair, based on our identification in chapter 4, of $m = 1.94 \times 10^{-22}$ eV/c^2 and $g = 1.21 \times 10^{-28}$ Jm^3/kg. We choose a computational box with sides of length $L = 34L_{\text{ref}}$, and $M = 240M_{\text{ref}}$. The aforementioned parameters remain fixed for the duration of this section. By varying the initial Gaussian size, number and distribution, we obtain a catalog of initial conditions with varying total energies to study the effects of the energy of the system. As mentioned in section 5.1.2, our energy space is limited by computational box size. We therefore probe the space $E_0 \leq E \leq -10^{-3}$ in dimensionless simulation energy, selecting initial conditions from our catalog that span this range fully. Here, E_0 is the reference ground state energy of the system if it were cooled completely, as defined previously.

Each initial condition is propagated to $40T_{\text{ref}}$, (which corresponds to approximately 20 Gyr). For each simulation, we record the time at which the largest spike in the energy components occurs, and regard this as the main collision time of the Gaussians, as well as the initial formation of the soliton. We then select 2 T_{ref} after this time as our initial 'equilibrium' time [3]. The density profiles from the initial equilibrium time to the final snapshot are time averaged, and the resultant time averaged velocity is computed for each simulation.

The results of this are plotted in FIG 5.5, where one can see a clear decrease in the ratio between core and halo mass as the energy of the system is increased. At the lowest energy, approximately all the mass is in the core, and this final core is approximately the ground state solution for a core of mass $M_{\text{core}} = M$. Interestingly, we find that for the entire energy range, a clear and definitive sharp peak is visible in the velocity curve, after which the velocity continuously decreases. Naturally, for lower energy states in which the core is more pronounced, the decrease in velocity from the peak to the outer radii is more substantial. Most importantly, in none of these cases does the velocity continue to grow beyond the core. Therefore, within the limits of our tested time-averaged 'equilibrated' data, one can say that the velocity **must**

[3] We bring to the readers attention once again that the system never truly reaches equilibrium, and that the core continues to grow. Therefore, we emphasise that the equilibrium we refer to here is not a true equilibrium, but on the timescales we consider–and those relevant to our Universe–we are able to consider it as such. That is to say, the core has formed, as has the halo. The core will nevertheless exhibit growth, as later discussed.

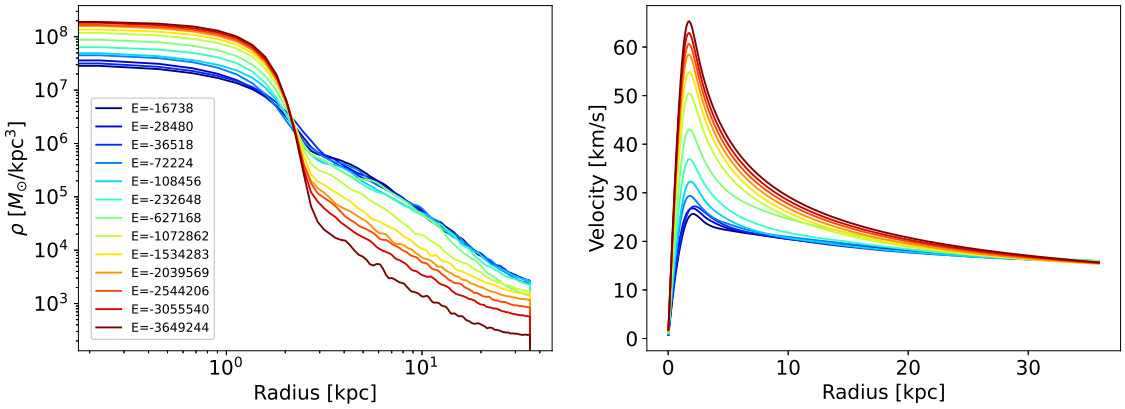

Figure 5.5: (Left) The 1D shell-averaged density plots of 3D simulations composed of particles of the same mass and interaction strength, and the same total mass within the computational box. Total energy is varied across simulations and is given in units of E_ref from Eq. (5.2), showing an increase in core mass with a decrease in energy, while the halo loses mass to compensate. (Right) The corresponding velocity profiles for the former. A sharper peak is visible for velocity curves that are computed from higher mass cores, while this peak is less noticeable in higher energy systems with a lighter core and heavier halo.

continuously decrease after the peak value. In fact, we can approximately identify this velocity peak in the range between $2.16\,r_c \leq r_{v,max} \leq 2.16\,r_h$, assuming $r_h > r_c$ [92].

For each simulation's time averaged profile, we perform the same bimodal fit as in Chapter 4, utilising the SG-NFW profile. From this, we obtain a good approximation of the core mass, without the need to propagate the system for longer time periods to collect enough data to compute the Penrose-Onsager mode [80]. These fitting results are found in FIG. 5.6.

5.3.1 Mass and Radius of the Core

It is important here to note that a simulation with lower energy creates a core of greater mass. Therefore, for this section, our use of energy as the independent parameter in the investigation can be interchangeably parameterised as a variation in the core mass, instead.

From our derived equation for the radius–see Eq. (4.2)–with static shape parameters rather than ones that depend on Γ_g, we expect the radius to decrease to accompany an increase in total core mass up to a limiting value in the Thomas-Fermi limit, if m and g remain fixed. That is to say, in a universe with a specific m and g pairing, heavier cores are smaller than lighter cores unless the core in question is in the Thomas-Fermi regime, in which case the radius becomes independent of any further addition of mass. However, in the regime of non-constant shape parameters–where they depend on Γ_g–we find an interesting alternative: the radius will in fact increase very subtly as the core mass is increased. This is of course due to

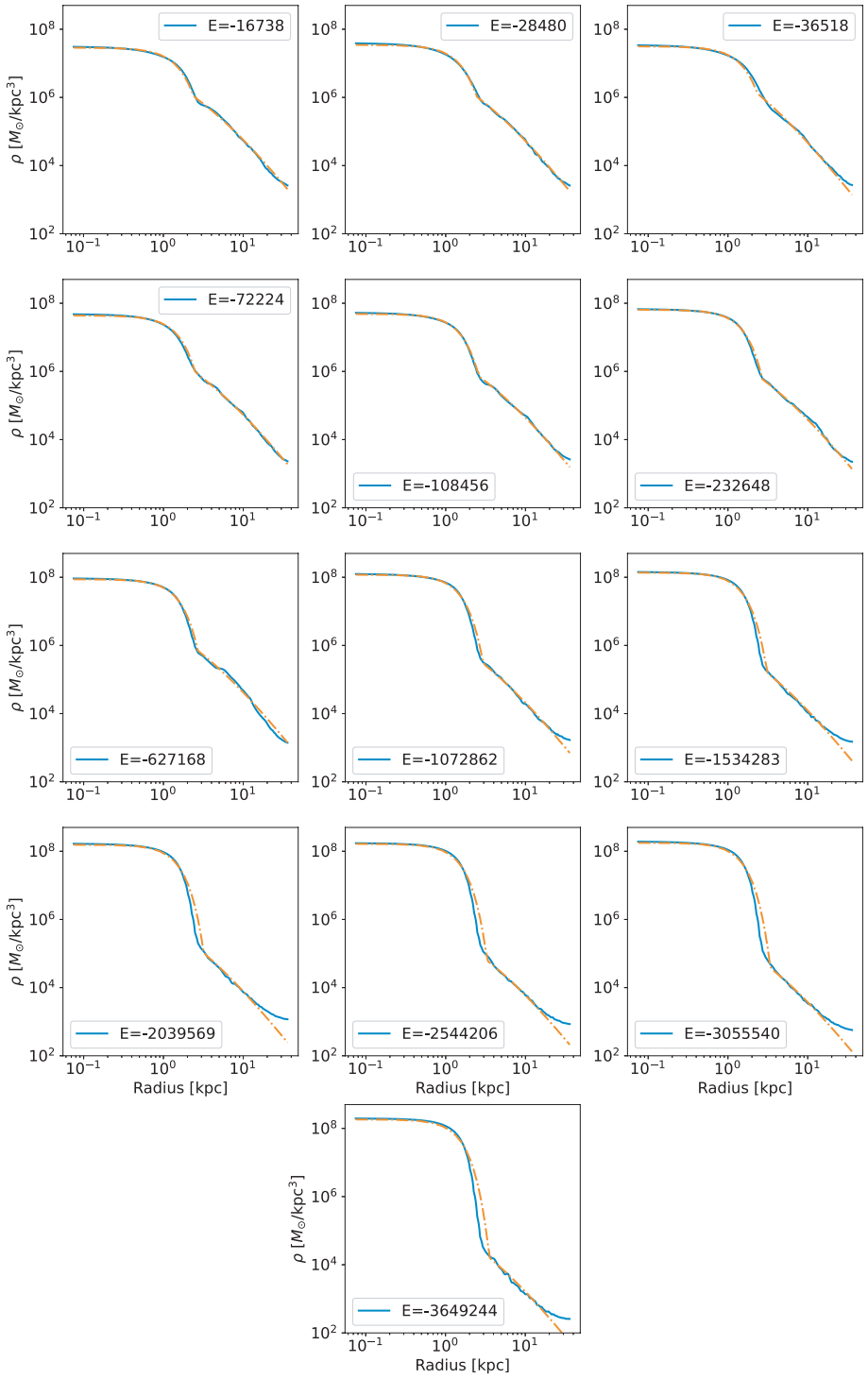

Figure 5.6: The SG-NFW fits (orange dash-dotted lines) for each simulation (solid blue lines) of varied energy. All energy here is given in units of E_{ref}, as in Eq. (5.2). Across all simulations, the boson mass, self interaction strength, total mass and computational box size are kept constant. The fits are generally excellent across the entire range of probed energies, however the SG-NFW profile does not fit as well at very low energy due to the fact that in this regime, Γ_g is much greater than in the low-core mass, higher energy case. This is because the SG profile does not quite replicate the sharp drop in density at the outer regions of a very strongly interacting core, but we still have excellent agreement with numerical data in the inner regions, as well as the halo.

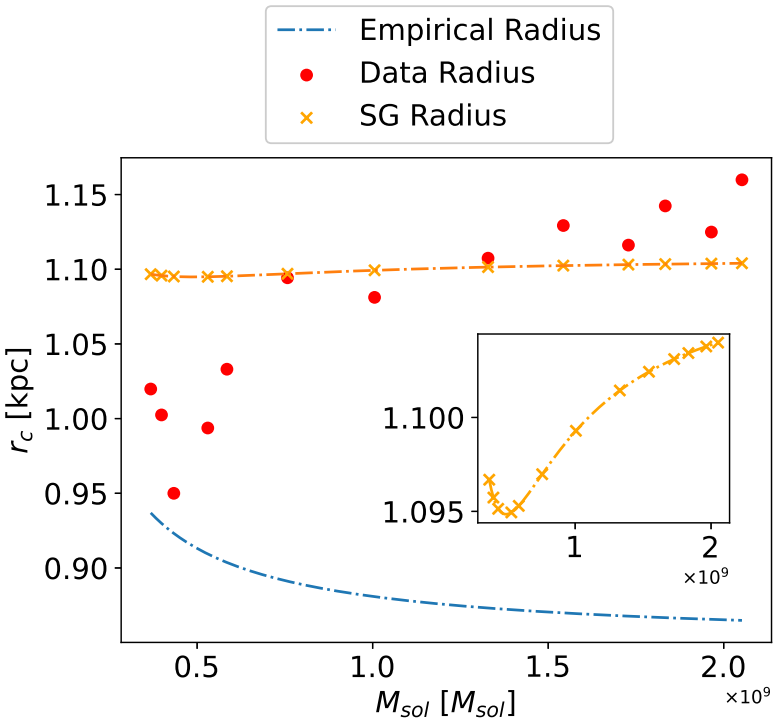

Figure 5.7: The lines show the expected radii for cores of a given mass, assuming our chosen values of m and g. The empirical profile (blue), and its rules, anticipate a drop in radius with an increase of mass, approaching an asymptotic value at which the Thomas-Fermi regime takes hold and radius becomes independent of mass. The SG profile (orange) instead demonstrates a very small dip in radius, and then a continual increase up to another asymptotic value. Radial fits based on the data (orange markers) are also plotted. The change predicted by the SG analysis are, however, negligible on an observationally relevant scale. The numerical data on the other hand demonstrate a clear growth in radius corresponding to an increase in core mass.

the varying nature of the dimensionless shape of the system, wherein the steepness of the core's tail rapidly grows with an increase in self interaction strength, and so the radius must increase to accommodate the additional mass. Therefore, this growth manifests in the Γ_g dependence of the shape parameters. Our analysis of simulation data finds, in fact, that the growth in core radius with an increase in mass is significantly more drastic than predicted by the SG. These results are outlined in FIG. 5.7; the blue line indicates the expectation for the radius to decrease as the mass grows, owing to the formula for the radius in the absence of Γ_g-dependent shape parameters as in Eq. (3.41) and [2]. The data points from simulation, however, increase by more than 15% across the spanned range, demonstrating a clear trend in growth. Further results are needed to reach meaningful conclusions, including results from solitons of wider mass ranges, different boson masses and different self interaction strengths, the preliminary data hints at

the fact that the increase in localised dimensionless interaction strength, Γ_g, dominates the radius relationship over the gravitational aspect from increasing the mass. That is to say, the repulsive pressure dominates over the gravitational attraction in the inner core, and the result is an increase in radius owing to an increase in soliton-specific dimensionless interaction strength from the increasing of the soliton mass. From the formula for g_*, given in Eq. (3.15), an increase in soliton mass decreases g_*. Therefore, if g is constant, as is the case across these simulations, then higher mass solitons are found further along the range between non-interacting to the Thomas-Fermi regime, as they would correspond to a higher dimensionless ratio of $g/g_* = \Gamma_g$. Given precise measurements of the velocity profiles of galaxies of various mass, if a behaviour such as this is discovered where an increase in core mass corresponds to an increase in core size[4], it would be a major point for self-interacting FDM.

5.3.2 Core-Halo Mass

For clarity, our underlying assumption for the relevance of the core is repeated here: we assume that any FDM core-halo system is a superposition of excited states around the core. In the event of the complete removal of energy such that the entirety of the system is in the ground state, a solitary core would remain. Excitations to this ground state systematically build a halo around a core which decreases in mass as the halo increases in mass. However, chronologically in reality, one does not expect to begin with a ground state which is then excited systematically, but rather a chaotic collision and gravitational collapse leads to an automatic formation of the final state. Nevertheless, the pathway to the final state is not relevant for this analysis to hold, and one may regard it as the former case for simplicity. With this in mind, it is clear that the ground state distribution and energy of the entire system is crucial; we will make use of E_0, which is the ground state energy of the core that would exist if the entire system in question is at minimum energy rather than in an excited state. Concretely, for a given 3D simulation of mass M_{total}, some distribution of the mass will be in the soliton, M_{sol}, and some will be in the halo, M_h, where $M_h = M_{\text{total}} - M_{\text{sol}}$. A soliton of mass M_0, and its energy, E_0, describe the case when $M_h = 0$, and $M_{\text{sol}} = M_{\text{total}}$. As before, we ignore the mass in the corners of the box.

Taking the simulations in FIG 5.6, we compute the total energy of the each simulation and scale it using the ground state reference scaling energy E_0. We compute E_0 using the SG shape parameters for a given m and g, and considering the total mass of the spherical integral to be the mass of this SG. This can be expressed as

$$E_0 = \Theta_{Q,0} + W_0 + U_0, \tag{5.4}$$

[4]We remind the reader here that an alternative would be for the core to shrink while the density increases.

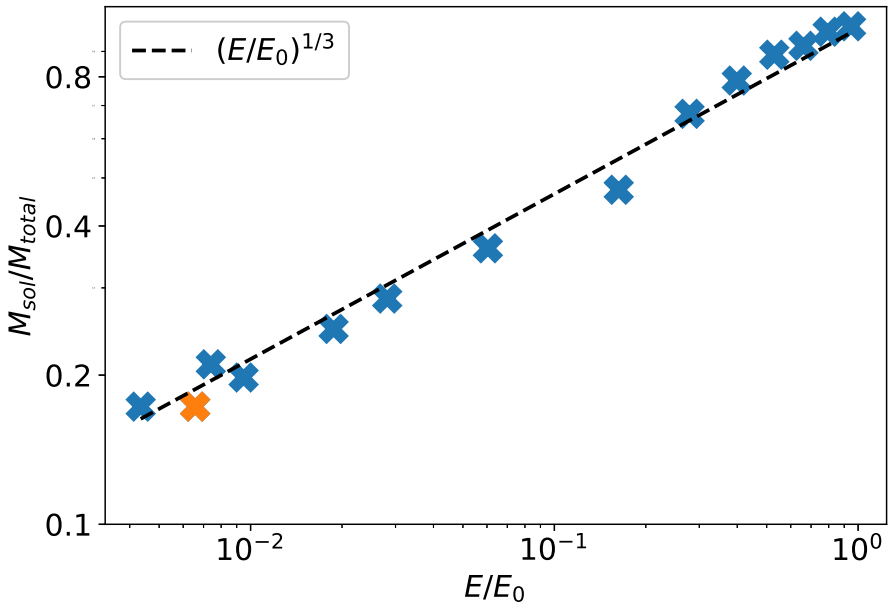

Figure 5.8: For our simulated systems, we show here the relationship between $M_{\rm sol}/M_{\rm total}$ and E/E_0 for each core-halo. The blue data points are all corresponding to the data in FIG. 5.5. The orange data point corresponds to a simulation of $M = 500M_{\rm ref}$ and is the simulation that is used in the final section of the chapter to recreate the galaxy UGCA444. We include it here to show that it is consistent with our expectations.

where there is no classical kinetic energy due to the fact that the hypothetical ground state solution is static. As mentioned in the previous section, the core mass is taken by fitting a SG+NFW profile, and taking the SG parameters from the fit only, ignoring r_t and r_h.[5] We then plot the fraction of mass in the core against the scaled energy, obtaining a clear relationship:

$$\frac{M_{\rm sol}}{M_{\rm total}} = \left(\frac{E}{E_0}\right)^{1/3}. \tag{5.5}$$

These results can be seen plotted in FIG. 5.8. It is more useful in our case to reframe this as a function $E(M_{\rm sol}/M_{\rm total})$, given that we have an approximation for the distribution of mass between the core and the halo from our fitting of observational data. Thus in future work, if one wishes to recreate observational halos, the ratio of the core mass to halo mass can be computed for a best fit profile, and used as a guide for what the total energy of the simulation

[5]This is equivalent to replacing the transition radius parameter in the fit to be infinite, such that the Heaviside step-function returns only the Super-Gaussian.

should be. This can be expressed as

$$E = \left(\frac{M_{\text{sol}}}{M_{\text{total}}}\right)^3 \cdot E_0 \,, \tag{5.6}$$

where both M_{sol} and M_{total} can be obtained from approximate fits to data, while E_0 can be computed easily using the parameters for the best fit. This formation of the relation will allow us to take observational results, fit their extracted and corresponding spatial profiles using the SG-NFW profile, and then make use of these parameters to compute the energy necessary to replicate the galaxy in simulation. Indeed the results are independent of boson mass, self interaction strength and total mass as these parameters are scaled out, nevertheless it would still be necessary in future work to confirm these results for a broad range of parameter space through direct simulations. We have also included a data point for a simulation where $M = 500 M_{\text{ref}}$ to show that it sits on the trend line in FIG. 5.8 (orange data point). We do note that the minimum value of Γ_g in these simulations is $\Gamma_g = 6.5$, meaning all data (with computed range $6.5 \leq \Gamma_g \leq 207$) correspond to self-interacting FDM, and no data point reaches the weakly/non-interacting regime. A further, and very relevant, piece of work would be to map this transition into non-interacting by either simulating even higher energy systems, to obtain cores which are lighter and therefore will have a smaller value of Γ_g, or to generally tune down the universal g value of the simulations to map this transition.

5.4 Granules in FDM Halos

Though we do not conduct an in-depth study of the granular structure of self-interacting FDM halos, we may perform a qualitative analysis instead. We select one snapshot from each 3D simulation shown in FIG. 5.5, that occur approximately 2 Gyr after the spike in the energy components, indicating the collapse. For each of these simulations, we have computed the time-averaged, shell-averaged 1D radial profile. From this, we compute the equivalent 3D profile simply by extending the radial density data to three dimensions, assuming perfect spherical symmetry. We then subtract this time averaged, shell averaged 3D density profile from the corresponding snapshot to show the regions of over- and under-densities. The results are plotted in FIG. 5.9, and we stress again that these results are qualitative and simply aim to show how the size and quantity of granules varies as one changes the structure of the core-halo system. Indeed, for simulations where most, and almost all, of the mass is in the core, granules are negligible as they are very low density compared to the inner core region. The plotted results show the over and under densities, therefore granules on the outside are of lower density than granules closer to the centre of the halo, due to the fact that the average

background density of the halo is higher in the centre. An interesting factor to note is that for high energy halos, where the majority of the mass is not found in the core, granules are of larger size and smaller in number. On the other hand, the lower the density of the halo in comparison to the core, the greater the number of granules and smaller their size.

Importantly, this implies that granules do in fact follow the same trend in core size, as a core in the absence of self interactions. That is to say, granules obey the rule for non-interacting cores, which is that an increase in mass results in a decrease in radius. This could likely be attributed to the fact that granules are of significantly lower density than the core, and therefore the effective local Γ_g value for each individual granule is low enough to be considered non-interacting. This warrants further and much deeper investigation, though these preliminary results suggest interesting behaviour and a decoupling between the size of granules and the size of the core.

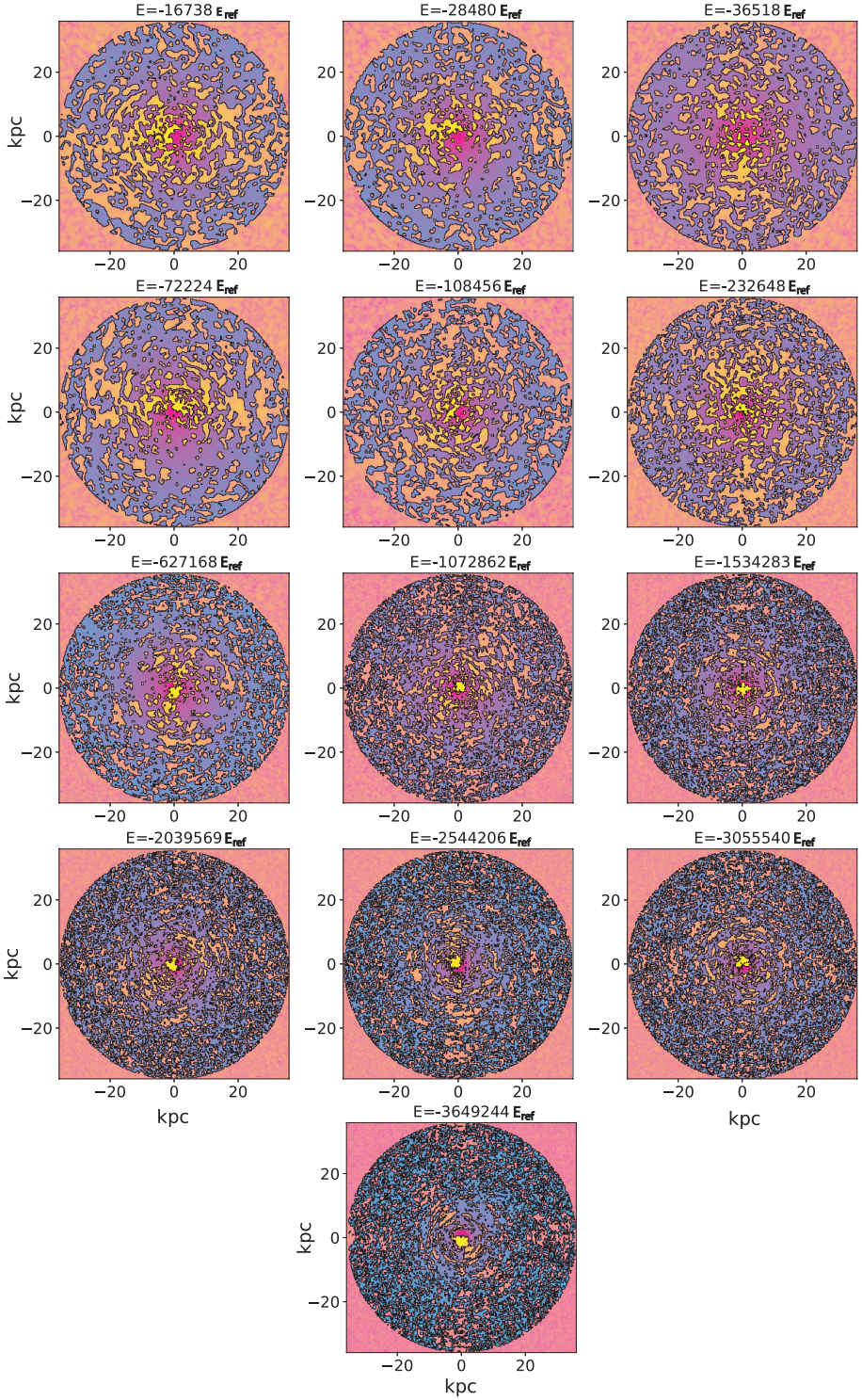

Figure 5.9: Slice plots of the simulation of the $x = 0$ plane for snapshots of the 3D simulation, that occur approximately 2 Gyr after the initial collapse. All data is plotted qualitatively to show the regions, sizes and numbers of over and underdensities. Overdensities are orange, while underdensities are blue.

5.5 Simulation and Analysis of Real Halos

From our observational analysis and fitting in the previous chapter, it is clear that most halos have a very light core in relation to their host halo. Therefore, following the assumption that the total energy of the system is the defining factor of the configuration of the core-halo system, we expect that the total energy of the system will be very close to 0. This is reaffirmed by the consideration that all FDM structures with positive energy shed excess high-energy matter, leaving a barely bounded core-halo structure with a quantifiable total energy close to, but less than, 0. We thus know to search for initial conditions with high energy. This, of course, requires the assumption that these halos are isolated in the sky, rather than entangled in a cosmic web of dark matter. This assumption is bold and likely does not hold, but it allows us to simplify the situation and arrive at well defined initial conditions to numerically generate a core-halo visualisation purely from analysis of observational data (such as rotation curves).

To compute the desired total mass, we extrapolate our ideal SG-NFW fitting profile from the previous chapter to our desired computational box length. Integrating the fitting profile yields a desired target mass for the spherical profile. However, given the fact that the computational domain is a cube, we must also account for matter which will fly to the corners and will not be azimuthally averaged to form the final radial profile. With this in mind, it would seem the right thing to do to select a small range of masses greater than the one computed from the integration of the fitting profile, and propagate them in parallel to select the best final result.

There exists several factors that we must consider thoroughly. Firstly, we must know if the dark matter density profile will evolve significantly in comparison to orbital time of stars. For this reason, we will consider multiple snapshots across a range of time to verify that the profile is stable and can indeed correspond to astronomical observations.

The second factor to carefully consider is the continuous growth of the central core density on a timescale greater than the age of the Universe. This has significant implications for the state of galaxies when we observe them, if FDM is found to be the solution to the dark matter problem; the growth of cores for such a length of time implies that galaxies as we observe them today are unlikely to be in equilibrium, and are still significantly evolving.

In fact, we will discuss below the consideration that the absence of a sharp peak in the velocity curves of many galaxies suggests that, in our simplified model and given our chosen m and g are correct for our Universe, the galaxies are still observed early in their evolutionary timeline, and a clear and definable transition from core to halo has not yet formed. This is likely due to the presence of significant perturbations and oscillations in the profiles from non-equilibrated mass found in outer regions of the halo. However, these assumptions are based on the simulations obtained from a specific pairing of m and g, and it is possible that for a set-up

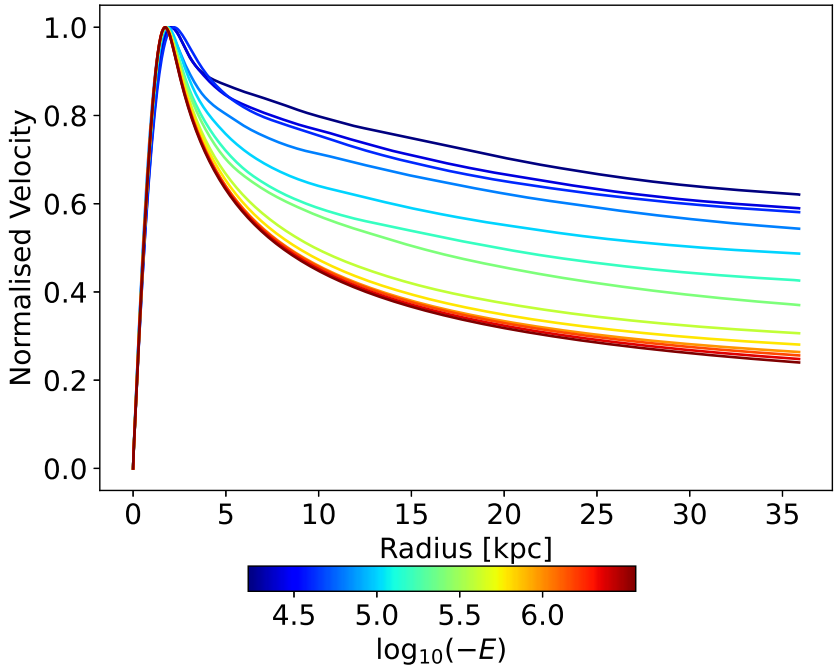

Figure 5.10: An image of the velocity profiles from each simulation shown in FIG. 5.5. The velocities are normalised according to the peak value in each case to show how the drop from the peak velocity to the velocity at the outer regions increases as the energy of the system decreases.

with weaker self-interactions, resulting in cores which are not in, or close to, the Thomas-Fermi regime, that these transitions from core to halo are less pronounced. This, too, would result in a less well-defined and less sharp peak in the velocity profile of the core-halo. In the Thomas-Fermi regime, the outer region of the core exhibits a steep drop with a sudden transition into the NFW profile. In a weakly interacting setting, the outer regions of the core do not exhibit such a large negative gradient, and the transition into the halo is more subtle.

Furthermore, with increased computational resources, one would be able to probe regions of even higher energy for the same fixed mass, which may also contribute to bringing these velocity curves from data closer to those seen in observation.

Another remark is that while we cannot recreate this growth in velocity after the transition simply here in these 1D shell averaged profiles, it is possible that the granular effects which are not present here contribute to this behaviour.

It is also possible that the addition of baryons would remedy this issue, though we will not include any discussion of this and leave this for possible future work.

5.5.1 The core-to-halo transition

FIG. 5.5 showed the velocity curves for halos of different energies, whose raidal density profiles were shown in FIG. 5.6. To highlight the existence of a local maximum near the edge of the solitonic core, we repeat such velocity profiles in FIG. 5.10, but now scaled by the peak velocity to better highlight the behaviour of such peaks. It is clear that higher energy profiles display a smaller and less pronounced peak in comparison to the outer region, but within the extent of these simulations, we do not observe any further growth of the velocity beyond the transition from the core to the halo. This is a clear and important feature that is present in multiple galaxies from the observational catalog. For example, in FIG. 4.3, UGCA444 and NGC3109 both exhibit a consistent increase in velocity beyond the core-halo transition. From FIG. 5.10, it is clear that a stable, equilibrium solution within our tested domain of parameters will not exhibit this.

Consider however instead the case of a system in which the halo has not yet reached approximate equilibrium. In such a case, there is still a considerable level of gravitational collapse occurring in the halo, resulting in larger over-densities. Over the course of billions of years, the velocity profile still shows notable variation beyond the core-halo transition region, despite the fact that the core forms immediately and does not experience substantial growth in observationally relevant timescales. This change is clearly illustrated in FIG. 5.11, where over the course of 4 Gyr, the velocity curve changes from a smooth, peakless transition between core to halo at early time (where the velocity curve exhibits growth after this transition as seen in the blue curve), into a state where the maximum value is at the transition, at which point the velocity only decreases at later time. It is important here to note that the times within FIG. 5.11 are relative to the initial collapse and formation of the core. It is not necessarily meaningful to consider the time it takes for a soliton to form from the initial conditions, nor the time required for the equilibrium to occur due to the fact that the initial conditions we generate in a computational box are not representative of those that occurred in the early Universe. This can be considered as a toy model which aims to show that the final state of a self-interacting FDM core-halo system, with these specific parameters, must not yet be in equilibrium if it is to exhibit the features seen in observational velocity curve data. This is at least what our analysis shows in the absence of baryons, and also within our computational limitations.

As a result, in order to recreate the effect of continuous growth of the velocity curve beyond the transition from core to halo seen in some observational data, we propose to consider snapshots at earlier times before the system has fully reached an approximate equilibrium.

This sounds plausible, on the grounds that in our Universe, there is no clear evidence to suggest that the dark matter of galaxies has necessarily reached equilibrium, as we do not have explicit knowledge of the initial density distribution of the system before collapse. It is entirely

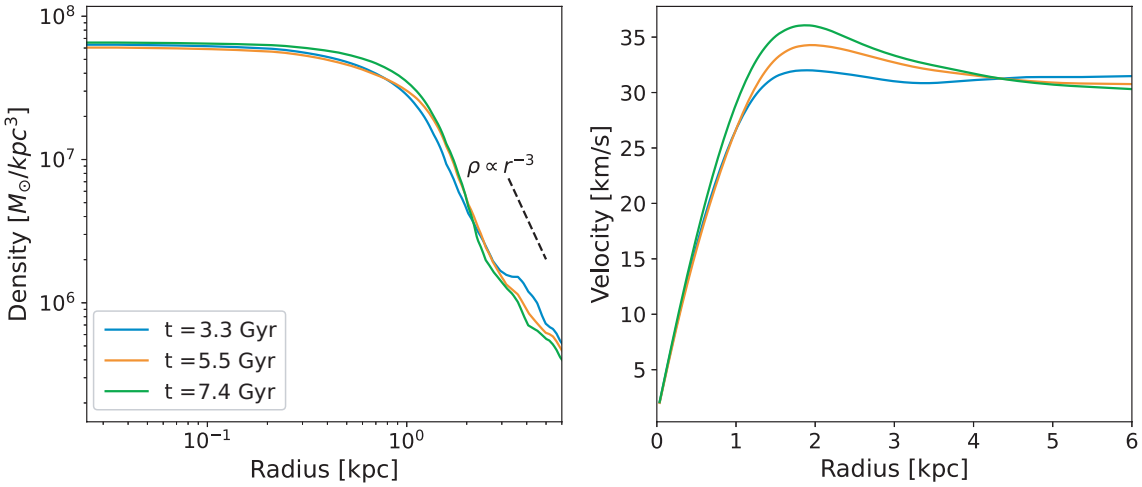

Figure 5.11: Three example profiles from a 3D simulation at different evolution times, with the earliest (blue curve) taken approximately 3 Gyr after the initial collapse. We use the time at which the initial collapse and formation of the core happens as the 'ground' time, $t = 0$ for the sake of simplicity. (left) The 1D shell averaged density profiles of these snapshots. (right) The computed velocity curves from the density profiles. One can witness the gradual transition from a velocity profile which exhibits no significant peak in velocity to one which has a clear and definable peak followed by a clear reduction in velocity at outer radii.

possible that galaxies which demonstrate an increase in velocity at outer radii when observed were formed from a sparser and more spread out density distribution. In such a case, the initial core and halo forms while mass is still being brought in from the outer regions. If correct, this could potentially be a highly relevant statement in understanding the state of the Universe. But, one should of course first revisit such findings, while allowing for bosonic feedback and other astrophysically relevant features.

Given the tools that we have thus developed, we now are able to approach and tackle the final goal of this chapter: to recreate a target halo whose inferred velocity profile agrees with observational data.

5.6 Creating UGCA444

The ability to simulation of 3D DM halos corresponding to real halos in our observational reach is something that will unlock incredible potential in our ability to understand the nature of dark matter. Specifically, for FDM, there are many observational signatures which appear in simulation, though they are not present in semi-analytical fitting formulae, *e.g.* the NFW profile does not possess the information of granules, though these may well be observationally relevant and significant. Though one may create arbitrary 3D simulations, it is difficult to assign the

importance of their characteristics to our Universe without inherent knowledge of important parameters such as the total mass, the boson mass and the self interaction strength. For this reason, we emphasise the importance of this section.

From the SPARC catalog, we select the galaxy UGCA444 due to multiple reasons: there is a large number of data points; the data points extend well beyond the core; the maximum velocity of the system is among the lower of the selection, meaning the total mass of the system is also lower. This is ultimately easier to simulate given our computational limitations. We target a simulation in which the box covers a range of -34 kpc to $+34$ kpc. We begin simulations using a 320^3 grid. The argument in favour of such a large box is that we wish for the order of magnitude ratio between the density of the central core and the density profile of the halo at the computational box edges to be as large as possible - ideally, we aim for 4 orders of magnitude, here. The reasoning behind this desired density ratio is to minimise the effects from the periodic boundaries, as mentioned previously in this chapter.

With this consideration in mind, we choose to alter our optimal SG-NFW profile for the galaxy UGCA444 from chapter 4 slightly. As mentioned in chapter 4, there is a broad range of r_h values which still produce velocity curves that agree with observational errorbars. For this reason, we tune r_h to reduce the extrapolated halo mass density at the computational box edges, and also decrease the total mass of the system in return for a reduced computational cost. This target SG-NFW profile can be seen in FIG. 5.12 as the black line in the (left) density plot, and the black line in the (right) velocity plot. Although the velocity profile does not fit quite as well to the observational data as our optimal fitting in chapter 4, it still sits very reasonably within errorbars. The remaining parameters for the SG-NFW profile are the same as those in the previous chapter for our best fit for UGCA444. Specifically, our target UGCA444 profile has parameters: $\rho_0 = 5.12\times10^7\, M_\odot/\text{kpc}^3$, $r_c = 1.04\,\text{kpc}$, $r_t = 1.43\,\text{kpc}$, and $M_{\text{tot}} = 5.33\times10^9 M_\odot$, and it is these parameters we aim for in our simulation.

As mentioned in the previous section, UGCA444's observational velocity data exhibits a continual growth in magnitude with an increase in radius. Therefore, we consider earlier snapshots in our simulations in which the system has not reached an approximate equilibrium.

The initial condition for this simulation which yielded radial velocity curves closest to observation can be found in FIG. 5.1, and the energy of the system is given in FIG. 5.2. We begin sampling snapshots from the initial collapse and formation of the core at ≈ 2 Gyr, by finding the time at which the spike in the energy components occurs, and then adding a cushion zone of approximately 1 Gyr for the system to settle from the collapse.

From this moment on, for each timestep, we compute the radial profile as detailed in the beginning of the chapter, and then find the corresponding velocity profule. Observational data is then overlaid with these profiles, and a range of snapshots is chosen which best fit within the

errorbars across almost an entire Gyr. These results are shown in FIG. 5.12. In this figure, we begin counting time from the moment of initial collapse and the formation of the soliton. The data clearly demonstrates that across the timespan of almost 1 Gyr, the density remains stable and sits well within errorbar bounds of the observational data. In both the density and velocity plots, the black line represents a SG-NFW fit to the data, as mentioned previously.

From the image, it is clear that the r^{-3} section of the NFW profile is retrieved, though the outer region of the velocity profile still suffers somewhat from the expected drop in magnitude following the peak, a feature we detail in the previous section.

The projected density plot (integrated along the z axis) in FIG. 5.12 shows the profile of one of the snapshots, and highlights what a small volume of the total dark halo this observational data manages to probe. The black circle in the inset of the projection plot represents the outer-most radius that the observational data contains, while the entirety of the inset represents the range plotted in the 1D density and velocity plots. Although the final observational data point is well outside of our expected soliton core, it is clear that the scientific community would benefit greatly from surveys which conduct sampling at larger radii for such dark matter dominated galaxies, perhaps additionally through alternative methods such as gravitational lensing. In the current sets of observational data, r_h largely remains a free parameter, and to impose constraints on this parameter for more accurate fitting and more conclusive replication of galaxies, we would require such surveys at larger radii.

Nevertheless, two things are clearly shown in the results presented in this chapter:

- The SG-NFW profiles which we are able to fit to the chosen catalog of SPARC galaxies indeed can be recreated via 3D simulations of self-interacting FDM with carefully chosen simulation parameters (total mass, box size) and are stable on relevant timescales.
- The velocity curve data from observation can also be recreated with 3D self-interacting FDM simulations.

The former is important as it lends significant credence to the concept of fitting semi-analytical profiles to observational data, while the latter carries weight in the fact that this is a first-of-its-kind proof-of-principle simulation which directly aims to represent and replicate a target galaxy in our Universe for which we have observational data through a full simulation of gravitational collapse given several, calculable and observable input conditions. Analysing and conducting similar investigations into observational data would be a powerful tool in either strengthening resolve in self interacting FDM, or altogether indicating that a different solution to the dark matter problem is necessary. The first step to be taken here is to repeat and target multiple galaxies from the SPARC dataset in hope of proving the robustness and importance of this approach. The implications and possibilities for future investigations are vast, some of

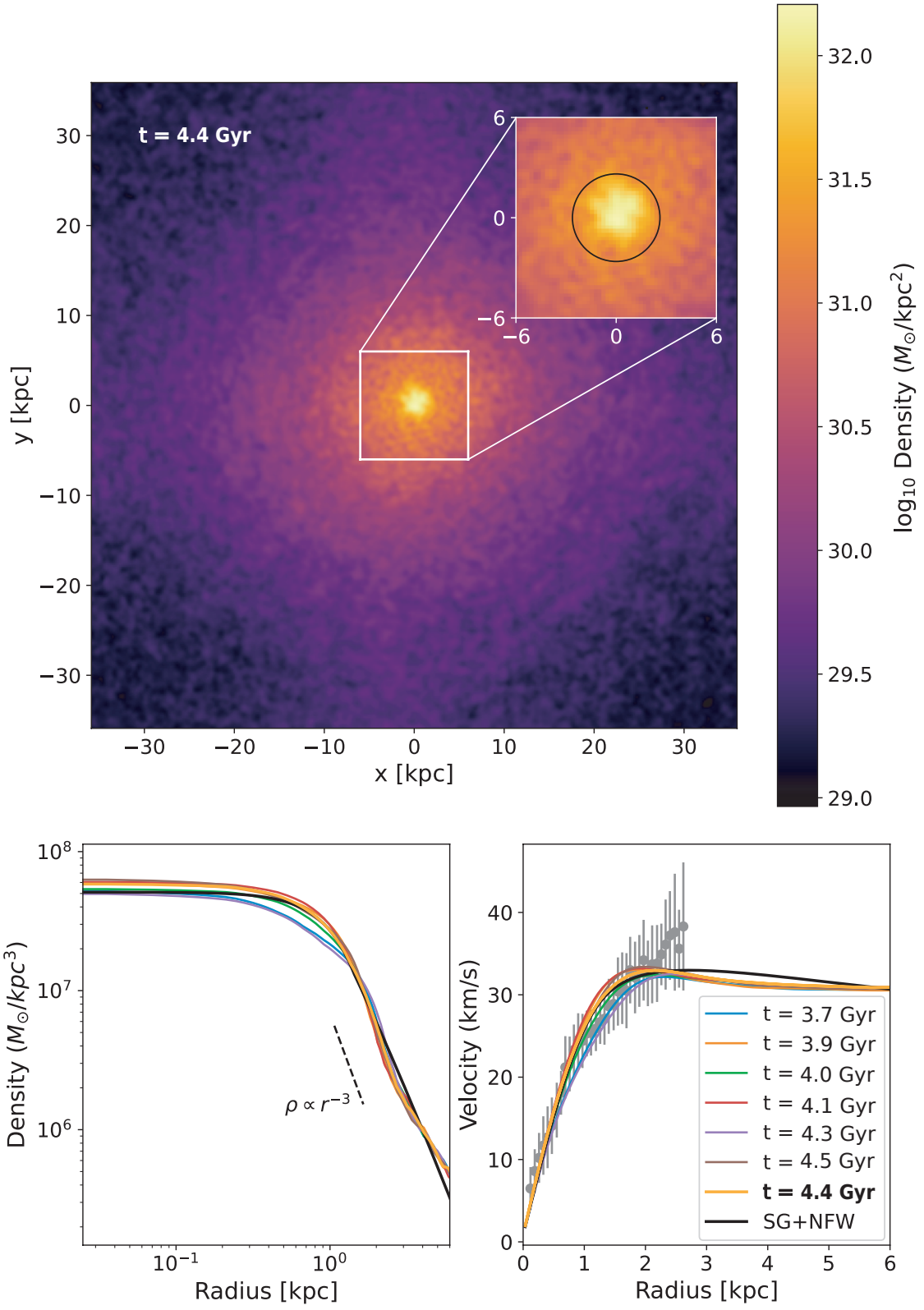

Figure 5.12: (Top) An integrated projection of a snapshot taken at time $t = 4.4$ Gyr after collapse. (Bottom left) The density profile from the shell averaged density of several time steps ranging from $t = 3.7$ Gyr to $t = 4.4$ Gyr. (Bottom right) The corresponding velocity curves from the aforementioned density profiles.

which we will discuss in the following chapter, and in the section for suggested avenues for future work in the concluding chapter.

6

Dynamic Behaviour in FDM Halos

The simplest (lowest-energy) excitation of the soliton core comes in the form of a radial oscillation. The rate of such an excitation depends on the total mass of the soliton, the mass of the constituent boson and—in the interacting case—the interaction strength [2]. Soliton core oscillations could in fact lead us to signals of FDM's existence in astronomical observations, as well as allow us to place constraints on the range of possible boson masses [38, 43], and they may play a part in gravitational heating of galaxies. It is also possible that core oscillations may drive dynamical behaviour in the entire halo structure due to interference [74].

In this chapter, we examine the dependence of the frequency of such small radial oscillations on the self-coupling strength parameter in terms of the dimensionless ratio Γ_g. This will allow us to overlay data from a variety of solitons on a universal curve.

The latter half of this chapter consists of preliminary work that looks into the orbital trajectories of test particles in a fully 3D FDM background. The effects of granules are made evident and the velocities of these test particles are compared to the integrated velocity curves from the 3D shell averaged radial profiles.

The solitons for which we conduct the oscillatory analysis are generated by applying imaginary time propagation to generate isolated ground state soliton cores. This is the first time such methods, borrowed from the cold atom literature, are used in a cosmological context. The novel shape parameters from previous chapters are then used to more accurately predict the

oscillation frequency from an analytical starting point. Finally, we conduct a first-of-its-kind controlled trajectory analysis of a test particle in the snapshot of a true simulated 3D fuzzy dark matter halo, and draw meaningful qualitative analysis regarding gravitational heating. We also comment qualitatively on implications for the inferred velocity curves by measuring the rotational velocity of test particles.

6.1 Isotropic oscillation

A proper study of the soliton's oscillations would involve a thorough analysis of its normal modes, though we leave this as a prospect for future work. Here, following [2, 50], we will employ a perturbative method for studying the radial oscillatory dynamics of the soliton, making the further assumptions that: (i) small oscillations can be described by making r_c, the parameter that sets the scale of the solitonic profile Eq. (3.1), time-dependent, i.e. $r_c \to r_c(t)$, and (ii) the resulting velocity field takes the isotropic form

$$\mathbf{u} = f(t)\,\mathbf{r}\,. \tag{6.1}$$

As we now show, these two assumptions can satisfy the continuity equation, Eq. (2.15), for a specific form of the function $f(t)$.

Although the form of the soliton profile $\rho(r)$ is not known for $g \neq 0$, we may make use of our ansatz $\rho(r) = \rho_0\varphi(r/r_c, \Gamma_g)$, further assuming that the profile becomes time dependent only via $r_c \to r_c(t)$. We thus obtain

$$\frac{\partial\rho}{\partial t} = -\frac{\partial \ln r_c}{\partial t}\left(\frac{\rho_0}{r_c}\varphi' r + 3\rho\right) \tag{6.2}$$

and

$$\nabla\cdot(\rho\mathbf{u}) = f(t)\left(\frac{\rho_0}{r_c}\varphi' r + 3\rho\right). \tag{6.3}$$

where φ' denotes a derivative w.r.t. the function's spatial argument. Clearly, the continuity equation is fulfilled if

$$f(t) = \frac{1}{r_c}\frac{\partial r_c}{\partial t} \tag{6.4}$$

and therefore describing the oscillation by assuming that the whole profile evolves with time via $r_c(t)$ and with the velocity profile

$$\mathbf{u} = \frac{1}{r_c}\frac{\partial r_c}{\partial t}\mathbf{r}\,, \tag{6.5}$$

is consistent witn mass conservation. This allows us to calculate the classical kinetic energy, Θ_C, as

$$\Theta_C = \frac{1}{2}\int \rho|\mathbf{u}|^2 d^3r, \tag{6.6}$$

$$= \frac{1}{2}\left(\frac{dr_c}{dt}\frac{1}{r_c}\right)^2 \left[4\pi\int_0^\infty \rho r^4 dr\right], \tag{6.7}$$

$$= \frac{1}{2}\alpha M\left(\frac{dr_c}{dt}\right)^2. \tag{6.8}$$

Therefore, solitons can exhibit oscillations which physically manifest as a uniform expansion and contraction of the soliton profile. The soliton mass M is constant in time and therefore the peak density must also experience oscillations as $\rho_0(t) \propto r_c^{-3}(t)$ - see Eq. (3.3).

6.2 Analytical Oscillation Frequencies

The total energy of the interacting system can be written as

$$E_{\text{tot}} = \Theta_C + \Theta_Q + W + U \tag{6.9}$$

$$= \frac{1}{2}\alpha M\left(\frac{dr_c}{dt}\right)^2 + \sigma\frac{\hbar^2}{m^2}\frac{M}{r_c^2} - \nu\frac{GM^2}{r_c} + \zeta\frac{gM^2}{2mr_c^3} \tag{6.10}$$

$$= \frac{1}{2}\alpha M\left(\frac{dr_c}{dt}\right)^2 + V(r_c)\,, \tag{6.11}$$

which can be thought of as an integral of the motion for the dynamical equation

$$\alpha M\frac{d^2r_c}{dt^2} = -\frac{dV}{dr_c}. \tag{6.12}$$

Hence, the fundamental, breathing oscillation mode of the soliton can be described by the one-dimensional motion of a non-relativistic, Newtonian particle moving in the potential V [2] defined above.

A static solution corresponds to a g-dependent equilibrium radius, r_c^*, satisfying

$$\left.\frac{dV}{dr_c}\right|_{r_c^*} = 0\,. \tag{6.13}$$

By performing a small perturbation about this equilibrium radius $r_c(t) = r_c^* + \varepsilon(t)$ in (6.12), we

find

$$\alpha M\ddot{\varepsilon}(t) + \left(6\sigma\frac{\hbar^2}{m^2}\frac{M}{r_c^4} - 2\nu\frac{GM^2}{r_c^3} + 12\zeta\frac{M^2 g}{2mr_c^5}\right)\varepsilon(t) = 0, \tag{6.14}$$

where, to avoid notational clutter, where we have dropped the $*$ superscript. At this point we remind the reader that, as $V(r_c)$ depends on g both explicitly and implicitly via the shape parameters $\sigma = \sigma(\Gamma_g)$, $\nu = \nu(\Gamma_g)$ and $\zeta = \zeta(\Gamma_g)$, such equilibrium value of r^* depends on g: in fact it corresponds to the g-dependent equilibrium value given by Eq. (3.24). We thus infer [2] a frequency

$$f = \frac{1}{2\pi}\sqrt{\frac{6\Theta_Q + 2W + 12U}{I}}\,, \tag{6.15}$$

where we remind the reader that $I = \alpha M r_c^2$ is the moment of inertia. Accounting for the interacting virial condition [Eq. (3.22)] and using the expressions for the shape parameters we can rewrite this as

$$f(g) = \sqrt{\frac{\sigma(\Gamma_g)}{2\,\alpha(\Gamma_g)\pi^2}\,\frac{\hbar^2}{m^2\,r_c^4(g)}\,\frac{1 + \left(\frac{3\,\zeta(\Gamma_g)}{2\,\nu(\Gamma)}\,\frac{1}{Gm\,r_c^2(g)}\right)g}{1 - \left(\frac{3\,\zeta(\Gamma_g)}{2\,\nu(\Gamma_g)}\,\frac{1}{Gm\,r_c^2(g)}\right)g}}\,. \tag{6.16}$$

Note that r_c is now a function of the self-coupling g. Such an expression, but with *constant* shape factors, has been previously analytically derived in Ref. [2, 50]. Here we generalize this to include the numerical differences hidden within the the dependence of the shape parameters on Γ_g.

In the $g \to 0$ limit and by making use of Eq. (3.42), we can write the oscillation frequency in a form which is solely dependent on the peak density of the soliton,

$$f(0) = \left(\frac{G\nu_0\eta_0}{\alpha_0\pi}\right)^{1/2}\rho_0^{1/2}, \tag{6.17}$$

with the shape parameters ν_0, η_0 and α_0 for the $\Gamma_g = 0$ empirical profile, Eq. (3.35), given in Table I. This form agrees with the $f \propto \rho_0^{1/2}$ relationship expressed in previous literature [39, 70, 71, 72, 43, 73]. Specifically, we find

$$f(0) = 11.4\left(\frac{\rho_0}{10^9 M_\odot \mathrm{kpc}^{-3}}\right)^{1/2}\mathrm{Gyr}^{-1}\,, \tag{6.18}$$

while in e.g. [39] the coefficient is 10.94, a value obtained from analysing oscillations of the central soliton in a simulated core-halo system. Very similar values are quoted in the literature [70, 71, 72, 43, 73]. The difference is very small and could be due to the fact that values quoted in the literature are mostly extracted from solitons embedded in halos and not

in isolation which may not be oscillating in their fundamental frequency only.

It is interesting to note that by looking at Eq. (3.41) and Eq. (6.18) we can compare our results to those from [2], finding that

$$r_{\rm emp} = 0.7149 r_{\rm Gauss}, \tag{6.19}$$

$$f_{\rm emp} = 1.0021 f_{\rm Gauss}. \tag{6.20}$$

As a result, and perhaps somewhat unexpectedly, although the radius parameters between the Gaussian profile and the empirical profile (3.35) are clearly distinct, the balancing of these and the various shape parameter values in these limiting cases appearing in Table 3.1 result in almost perfect cancellation, thus leading to practically the same predictions for the *frequency*. Therefore, our extended present work confirms that the Gaussian ansatz approach can be considered a remarkably robust approach for analysing the soliton's oscillation frequency.

6.3 Numerical Results for Non-Interacting Solitons

To numerically study the lowest-energy soliton oscillations we must perturb the obtained ground states. This can be very easily engineered in our numerical simulations using the following trick: instead of running our imaginary time propagation until full system equilibration has been achieved, we terminate such process somewhat earlier to allow for the otherwise almost perfect ground state solution to be left with a 'natural' built-in perturbation. Subsequently propagating such perturbation in the (real) time domain we can extract the frequency of such an oscillatory mode by performing a Fourier analysis of the dynamics of the peak density value.

According to Eq. (3.41) the radius, and therefore the peak density, are both functions of boson mass. We can therefore rewrite Eq. (6.17) in terms of the boson mass and soliton mass,

$$f(0) = \frac{1}{2\pi}\left(\frac{\nu_0^4}{8\alpha_0\sigma_0}\frac{G^4M^4m^6}{\hbar^6}\right)^{1/2}. \tag{6.21}$$

In order to compare results of the empirical and Gaussian profiles to our numerics, we evaluate the above frequency formula, Eq. (6.21), using the shape parameters obtained from the respective profiles. A detailed comparison between simulation data and the prediction from Eq. (6.21) is shown in FIG. 6.1 as a function of both (i) changing boson mass (within the range $10^{-22}\mathrm{eV/c^2} \leq m \leq 10^{-20}\mathrm{eV/c^2}$) [top plots] and (ii) changing soliton mass (within the range $10^6 M_\odot \leq M \leq 10^8 M_\odot$) [bottom plots]. This confirms the very good overall validity of Eq. (6.21) for the empirical (and Gaussian) analysis with our numerical data [FIG. 6.1(a)]. To better understand how these compare, and what the subtle differences between empirical and Gaussian

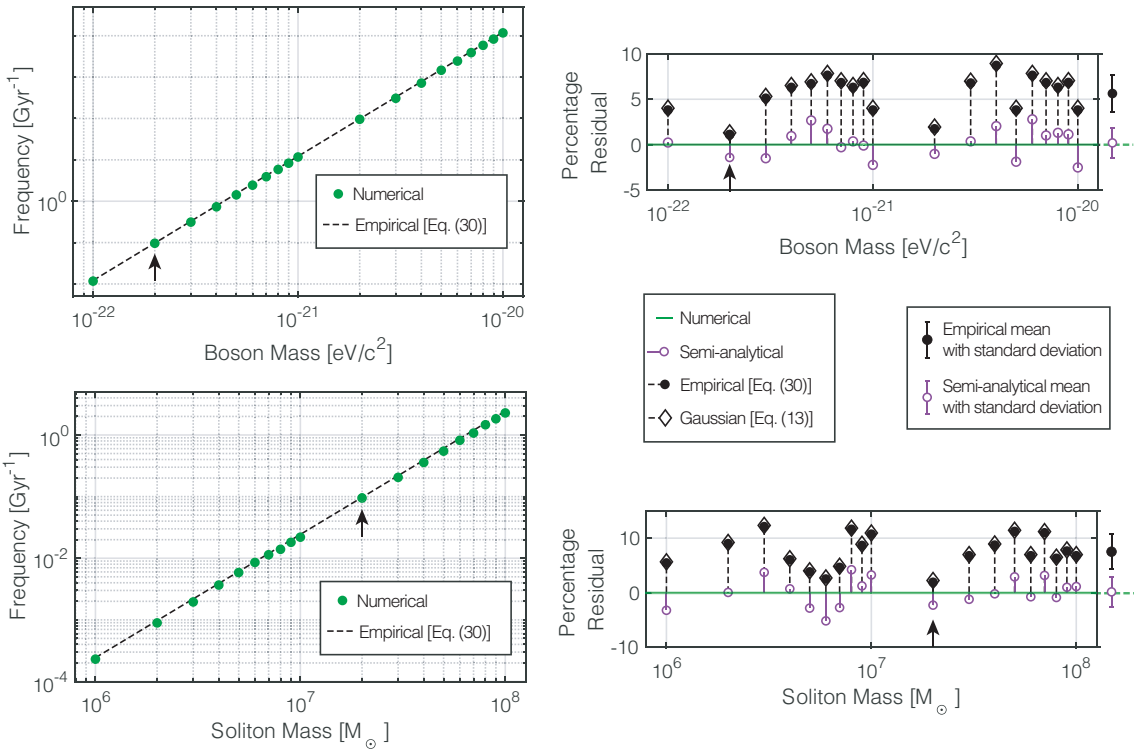

Figure 6.1: *Left:* (Top) The oscillation frequency for varying boson mass for a total soliton of mass $M_{\text{soliton}} = 2 \times 10^7$ M$_\odot$. (Bottom) The various results for oscillation frequency when the soliton mass is varied from a range of 10^6 to 10^8 M$_\odot$. The black arrow indicates a mutual point which is present in both simulation runs. The dashed line is plotted according to Eq. (6.21), in which the shape parameters are calculated from the relevant energy integrals of the empirical profile, Eq. (3.44). *Right:* A residual plot of the oscillation frequencies, calculated according to [(simulation − analytics)/simulation], for the case of (Top) varied boson mass and constant soliton mass, and (Bottom) varied soliton mass and constant boson mass. The zero line represents the simulation data. The filled black data points correspond to the residual between the simulation data and Eq. (6.21), with shape parameters from the energy integrals using the empirical profile. The black diamonds correspond to the same, but instead making use of the shape parameters from the Gaussian. The hollow purple circles use a numerical extraction of the shape parameters from each ground state solution to calculate the frequency. In either case, residuals are grounded on simulation data. To the right of each residual plot is a data point which represents the mean residual value for the case of frequency calculations from the empirical profile, Eq. (3.44), and the corresponding variance in the form of error bars. As can be seen from the two right sub-plots and discussed in the text, using the empirical or Gaussian profiles gives essentially identical results for the oscillation frequencies which are less accurate than those determined by using the shape parameters obtained from the numerical soliton profiles.

results (concealed in FIG. 6.1(a)) may be, FIG. 6.1(b) plots their scaled residual differences in each case.

This reveals that, despite a very good overall agreement with our numerical simulation data, such results for both empirical (filled black circles) and Gaussian (hollow diamonds) consistently overshoot the numerically-obtained frequency (green line). Motivated by our preceding detailed shape-parameter analysis, we thus proceed to calculate the shape parameters individually from each numerically generated ground state, and use these – rather than the shape parameters from the empirical profile – in Eq. (6.21): as expected, this semi-analytical procedure (open purple circles) yields a much better agreement with the oscillation frequency extracted from simulations. It is therefore clear that the calculation of the oscillation frequency of a soliton is in fact also sensitive (on the 10% level) to the shape parameters and therefore the shape of the profile.

6.3.1 Results for Interacting Solitons

The analytical prediction (6.16) for the oscillation frequency in the case of $g \neq 0$ can be written in terms of the dimensionless parameter Γ_g as

$$\begin{aligned} \frac{f(\Gamma_g)}{f(0)} &= \left(\frac{2}{1+\sqrt{1+15\,\mathcal{C}(\Gamma_g)}} \right)^2 \\ &\times \sqrt{1+\frac{15\,\mathcal{C}(\Gamma_g)}{1+\sqrt{1+15\,\mathcal{C}(\Gamma_g)}}} \end{aligned} \tag{6.22}$$

where we remind the reader that $\mathcal{C}(\Gamma_g) \equiv \frac{\zeta(\Gamma_g)\nu(\Gamma_g)}{\zeta(0)\nu(0)} \frac{\sigma^2(0)}{\sigma^2(\Gamma_g)}\,\Gamma_g$ - see Eq. (3.33). A comparison of the above formula, with the shape parameters obtained from numerical soliton profiles, to numerical simulations of oscillating solitons are shown in Fig 3.3(c).

Once again, as in the analysis of ρ_0 and r_c of the previous section, we can obtain the limiting values for f in the cases $\Gamma_g = 0$ and $\Gamma_g \to \infty$, by evaluating all shape factors $\{\zeta(\Gamma_g),\, \nu(\Gamma_g),\, \sigma(\Gamma_g)\}$ appearing in $\mathcal{C}(\Gamma_g)$ in terms of their non-interacting limits $\{\zeta(0),\, \nu(0),\, \sigma(0)\}$, or their strongly-interacting Thomas-Fermi limits $\{\zeta^{TF},\, \nu^{TF},\, \sigma^{TF}\}$. Such process gives us the corresponding non-interacting and Thomas-Fermi channels for the frequencies, respectively shown by the grey and dashed orange lines in Fig 3.3(c). Interestingly, in our numerical results the two channel limits experience a cross-over around $\Gamma_g \approx 1$, as can be seen in Fig 3.3(c)(i)-(iii) which show that the limit at the top of the channel is the non-interacting one for $\Gamma_g \lessapprox 1$ [Fig 3.3(c)(i)], while the Thomas-Fermi limit is found at the top for $\Gamma_g \gtrapprox 1$ [Fig 3.3(c)(iii)]. Our numerical data points always trace the upper of the allowed channels throughout the entire range of self interaction strengths.

All these results are obtained and analysed under conditions of isolated cores. However, when we consider cores embedded in halos, further interesting phenomena arise.

6.4 Core Growth

In our 3D simulations we observe an interesting phenomenon in the evolution of the cores and halos after collapse. We consider the initialisation time of a core-halo system as the time in which the core forms, and approximately 2 Gyr after the energy components exhibit a sharp spike. The system is evolved for up to 20 Gyrs after this event, depending on the time at which this initial collapse occurs[1]. For our simualted parameters, we find that there is still significant dynamical evolution on time scales longer than the age of the Universe. Primarily, high to mid energy simulations, clearly visible in the first seven plots of FIG. 6.2, exhibit a clear expansion in the halo. To display and analyse this, we conduct spherical mass integrals for radial shells of the 3D radial profile, and produce carpet plots to demonstrate how the integrated mass at each radial shell evolves with time for each simulated energy - these plots depict the time evolution (y-axis) for the mass integral value (colour axis) up to each radial shell (x-axis). If one were to draw a contour line for $M(r)/M_{3D} \approx 0.6$, equivalent to following the yellow colour on the carpet plots, they would find that the radius at which this mass ratio exists increases with time significantly, long after initial collapse. However, they would also find that the inner halo and core grow narrower in radius, becoming more compact. This effect is not clearly evident in the cases of low energy simulations due to the fact that the time evolution of such systems is much faster than high energy ones, and the initial density distributions are very localised. To confirm this in a more explicit manner, we plot the evolution of the peak density of each system, overlaid with the total spherical mass integral normalised by the total mass in the 3D computational box. These results are found in FIG. 6.3, where all higher energy simulations exhibit a clear growth in the ratio of $\rho_0(t)/\rho_0(0)$. At first consideration of such a growth in core peak density, one may assume that this growth is a consequence of mass entering from the corners of the 3D computational box, which is not accounted for by the spherical integral. However, the evolution of the spherical integral of the mass clearly identifies that this is not in fact the case, and that mass is rather *leaving* the spherical halo and migrating to the corners of the computational box.

It is clear, therefore, that a condensation process is occurring in which lower energy particle are migrating inwards, while high energy particles are migrating outwards. The highest of energy particles migrate towards the corners of the box to maximise their distance from the

[1] In some cases, due to the way the Gaussians are distributed, such a collapse occurs later in the dynamical evolution of the system.

core. This manifests as a clear simultaneous expansion of the halo and contraction of the core, on time-scales relevant to the age of the universe. This condensation process has significant impact on the validity of FDM as it implies that, as mentioned previously in this thesis, within the regimes probed, it is highly likely that many galaxies are not equilibrated at the current age of the Universe. This means that one would expect older galaxies to exhibit denser and more obvious cores. Additionally, it suggests that the velocity profiles of galaxies are not static on the scale of multiple Gyrs, and that significant evolution occurs, particularly in the inner parts of the halo. This effect has also been discussed in [105, 106, 89, 69], where they identify and comment on a clear growth of the core after setting up a core-halo system and propagating it dynamically. It is worth hypothesising here that much higher mass galaxies, such as that of the Milky Way, will exhibit dynamical evolution at smaller time scales. It is possible that the majority of this condensation process in these heavier galaxies has already occurred, though this demands further probing and simulation beyond our computational capacity. We note here that indeed this phenomenon occurs in both cases where randomly placed Gaussian mass distributions collapse to form the final structure, and in cases where a core-halo system is initiated by other means [69]. Given the disparity between the two methods, and the persistence of the condensation and growth of the core, one assumes that the effect would also be prominent in simulations initiated by means which are more tangible to the formation of cosmic dark matter structures in our Universe. However, to investigate this, one would need to consider the evolution of a system given realistic cosmological initial conditions. Such, more realistic, simulations may demonstrate that the growth of the core occurs at an even slower rate due to the unorganised initial distribution of mass requiring a longer timescale to reach a state of rapid evolution in which a dense core has formed. Therefore, we only hypothesise the possible impact of the dynamic behaviours discussed in this section on reconciliation with observation, and stress the necessity for in-depth further investigation into the topic to develop a fuller understanding of the dynamical processes occurring in FDM systems.

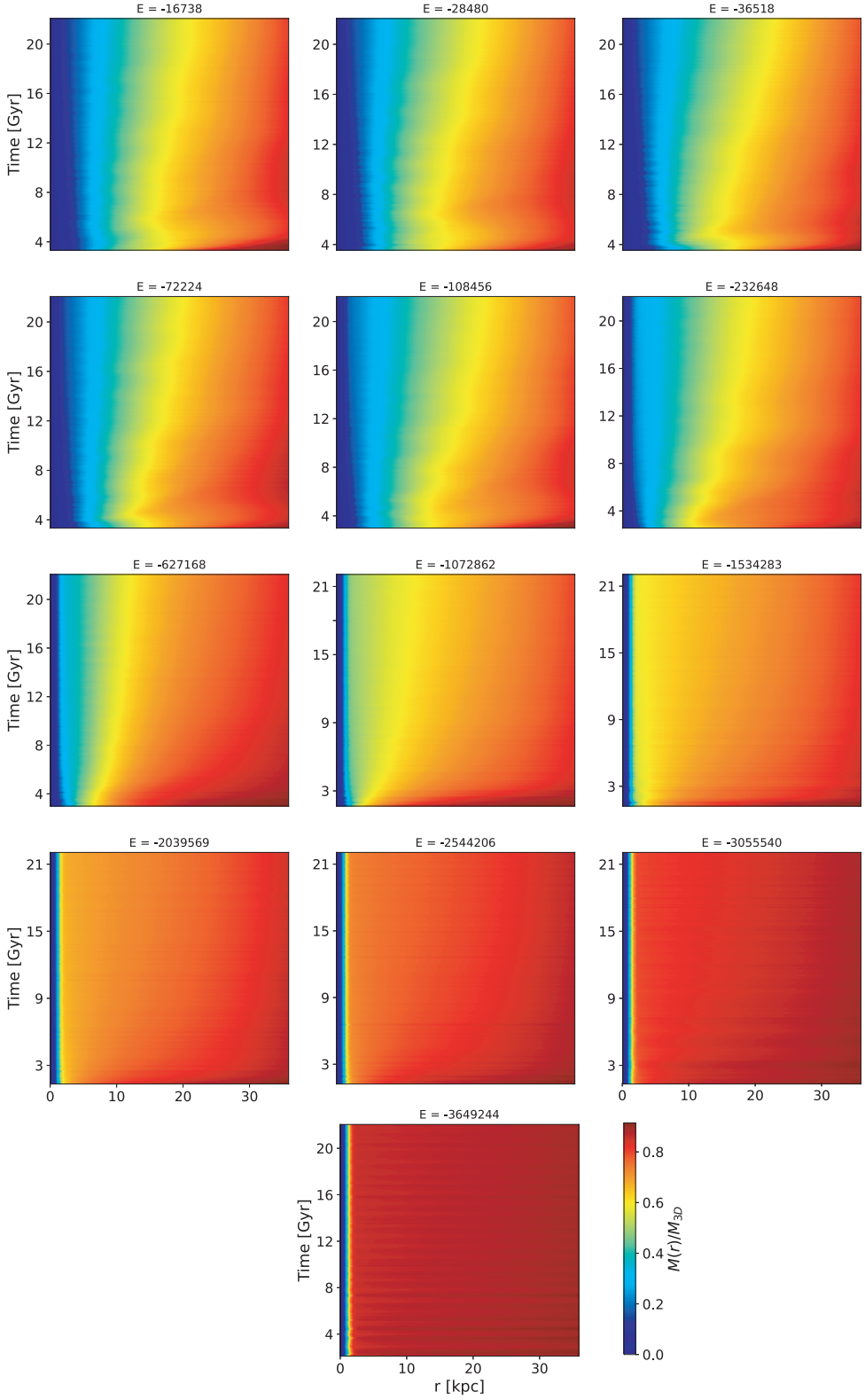

Figure 6.2: A set of carpet plots for each simulation in FIG. 5.6. Energy is in units of E_{ref}, given in Eq. (5.2). The spherically integrated mass is normalised by the total mass in the 3D computational box to show the effects of mass leaving the spherical halo into the corners of the box. In almost all cases, the core collapses and tightens while the halo expands.

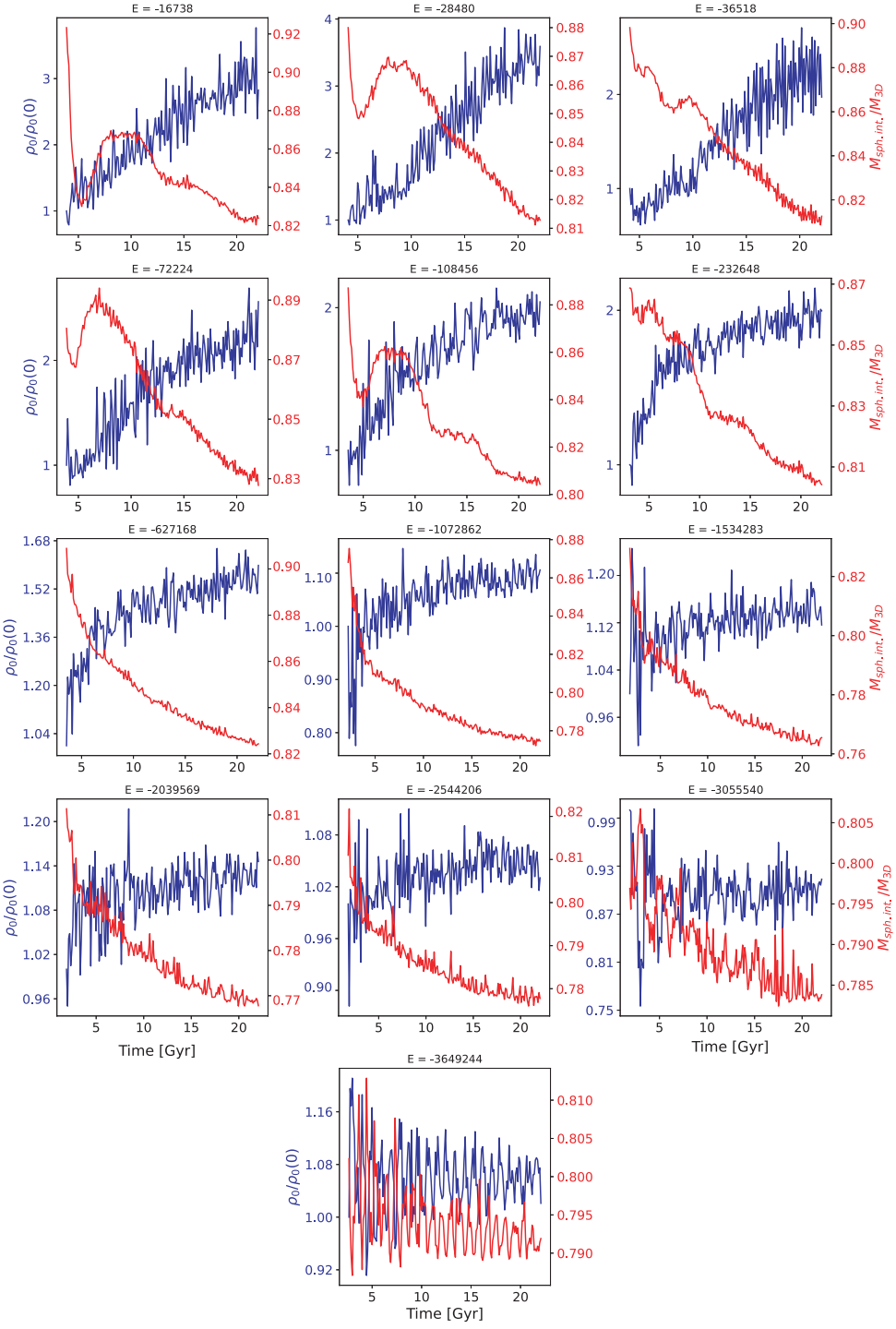

Figure 6.3: Plots showing how the peak density of the simulations from FIG. 5.6 evolve and increase with time. Also shown is the total spherically integrated mass normalised by the total mass in the 3D box. The blue lines correspond to the left $y-$axis, the normalised peak density, while red lines correspond to the normalised mass (right $y-$axis).

6.5 Velocity curves of dynamic halos via test particles

To make our findings self-consistent, we should verify that trajectories of test particles from the generated halo, when given the appropriate statistical consideration, recreate the rotation curves from which this halo was initially constructed. Here, we initiate this process by giving first considerations and tentative results that require further verification and very careful analysis. In particular, we note that while we discuss trajectories of individual test particles which are probably inaccurate reflections on the individual star level, we continue the first stages of such provisional discussion.

The computation of rotational velocity curves from 3D simulation data typically is obtained by first generating a 1-dimensional radial density profile by taking the shell average density at each discrete radius. However, this process removes the effects of granular under- and over-densities. These density fluctuations, or granules, may provide observational signatures in orbital trajectories by perturbing oribital velocities on a statistically significant level. To investigate this, we take a snapshot of a 3D galaxy. For completeness and ease of comparison, we consider the same data as in Section 5.6, meaning that the simulated halo we will analyse is one whose inferred velocity profile fits well to the observational data of the galaxy UGCA444. For further continuity, the snapshot we will consider is the one given in the top plot of FIG. 5.12, which is also highlighted by the yellow line in the density and velocity plots in the same figure. We will use a static background profile for this investigation, and will not allow the background density to evolve.

It is of crucial importance to stress that there are two possible ways to undertake this investigation, depending on the manner in which one re-centres the 3D simulation grid. Throughout this thesis, we have always re-centred the 3D grid such that the peak density is at the origin. This allows us to form neat 3D radial profiles which obey the rule that the peak density is at the centre. However, it may be more suitable to instead centre the grid on the centre of mass, such that it is instead found at the origin. We will conduct an identical investigation in both cases to demonstrate the difference.

The orbital simulation is initialised by first computing the force vector from the gravitational potential at each 3D grid point within the computational box, which is solved via the Poisson equation. We then place particles at a range of radii along the $z = 0$ plane, and give them a tangential velocity equal to the computed smoothed 3D velocity from the velocity curves. These particles are then propagated dynamically, and their velocities and positions are tracked in time. The important factor here is the fact that the particles are initiated with a velocity in the $x - y$ plane, and no z-component to their velocity. However, very quickly, the particles pick up a z-component which brings them out of the $x - y$ plane, as they are perturbed by density

fluctuations.

We expect these density fluctuations to have a significantly greater impact in the inner regions of the halo, and around the core, due to the higher over-density present. As one travels further from the core, the absolute density of the fluctuations grows smaller in line with the decrease of the halo's average density[2], and therefore the force component their gravitational attraction provides in comparison to the core and general average structure of the halo also decreases. Therefore, their perturbative effect on orbital trajectories should be less impactful. We would expect to see a narrower distribution of tangential velocities at larger radii due to less impactful perturbations in comparison to a significantly wider channel at lower radii.

Upon selecting an initial radius, r_i, to place a test particle at, we choose a random location on the circle defined by $x^2 + y^2 = r_i^2$, with an initial velocity in only the v_θ direction, equal to

$$v_\theta = \sqrt{\frac{GM_{sph}(r_i)}{r_i}} \tag{6.23}$$

where $M_{sph}(r_i)$ denotes the spherical integral of the shell averaged 3D density profile up to r_i. We then allocate the initial velocity across the x and y components such that the only velocity component in polar coordinates is v_θ, the tangential velocity. Propagating for several Gyr in a static FDM background, we begin to record the positions and velocities of particles after 1 Gyr. Each timestep of each particle after this point is considered a separate, independent, data point. The tangential velocity of each data point is computed and is used as a guide for the real velocity dispersion within our halo as a result of the surrounding dark matter background. We define the tangential velocity as

$$v_\top = \sqrt{v_x^2 + v_y^2 + v_z^2 - v_r^2} \tag{6.24}$$

where

$$v_r = \frac{x \cdot v_x + y \cdot v_y + z \cdot v_z}{\sqrt{x^2 + y^2 + z^2}}. \tag{6.25}$$

Given enough data points, we are able to form a statistical velocity curve from real particle trajectories. First, we generate radial bins, discretised identically to our 3D grid. We then assign snapshots of particles to these bins, such that any time a particle is found within the bin, it is placed into it as an independent data point. An analysis into each bin finds that the velocity dispersion per bin does not generally follow a Gaussian form, therefore we cannot consider standard deviations as our channel widths. In fact, in the case of many bins, the velocity

[2]Referring back to FIG. 5.9, one can see that the over-density of the granules is approximately consistent in comparison to the background halo for the radius at which they are located.

distributions are highly irregular. The resultant data is shown in FIG. 6.4. The dispersion of the tangential velocity for each radius is large, however the general shape of the tangential velocity dispersion clearly follows that of the observational data. Nevertheless, there are many data points at the inner radii ($r \leq 3$ kpc) that have very low tangential velocity. Without considering the limitations of our setup, it is difficult to draw meaningful conclusions, therefore we must now turn to these.

Most importantly, we should consider the manner in which we compute the force matrix. The 3D force matrix, which contain the information of the force on a particle given the static background gravitational potential at each coordinate, has the same discretisation and resolution as our 3D simulation grid. This matrix is computed once at the start of the simulation and does not need to be recomputed, due to the static nature of the background. Even if a particle is placed directly onto the $x-y$ plane, in a spherically symmetrical background where F_z should be equal to 0, it will still incur a minimal force component in the z direction. This, over time, can grow into an instability by offsetting what should otherwise be an orbit contained in the $x-y$ plane into a precessing orbit. To avoid this, we take the time averaged 1D density profile of the system, and use it to create a spherically symmetric, time averaged 3D density profile. We compute the potential and thus the force matrix for this profile, then subtract the value of the $x-y$ plane from that of the 3D density profile we are investigating. This removes the minor offset discussed from grid resolution, and reduces the numerical effects on the precession of orbit. In reality, this is a minor numerical patch for a lack of fine resolution on the grid, as well as the manner in which it is discretised. It is likely that this grid effect is negligible in comparison to the effects of the granular structure in a non-spherically symmetric case, but we implement this patch regardless.

Furthermore, in relation to the grid, we should consider the impact on low-radius orbits. At large r, the impact of the resolution is less than in the centre due to the fact that the particles travel across greater distances with a larger circumference. For this reason, their general trajectory is subject to the gravitational pull of all the mass within, which composes most of the force at each grid point. At small radii, this is no longer the case, and the difference in direction of force can be large and discontinuous between grid points. Indeed, a careful interpolation scheme would be beneficial here, though computationally expensive.

Additionally, we note that the majority of this wide dispersion in velocity occurs up to, and just after, $r = r_t$ (see dashed vertical line in FIG. 4.8).

To test disc galaxies (which is not our aim in this chapter, though we include this discussion for completeness), on more physical grounds a difference is the absence of a galactic disc in our simulations. These discs consist of baryonic matter and their gravitational pull provides a restoring force to objects which exit the galactic plane. The absence of this results in an absence

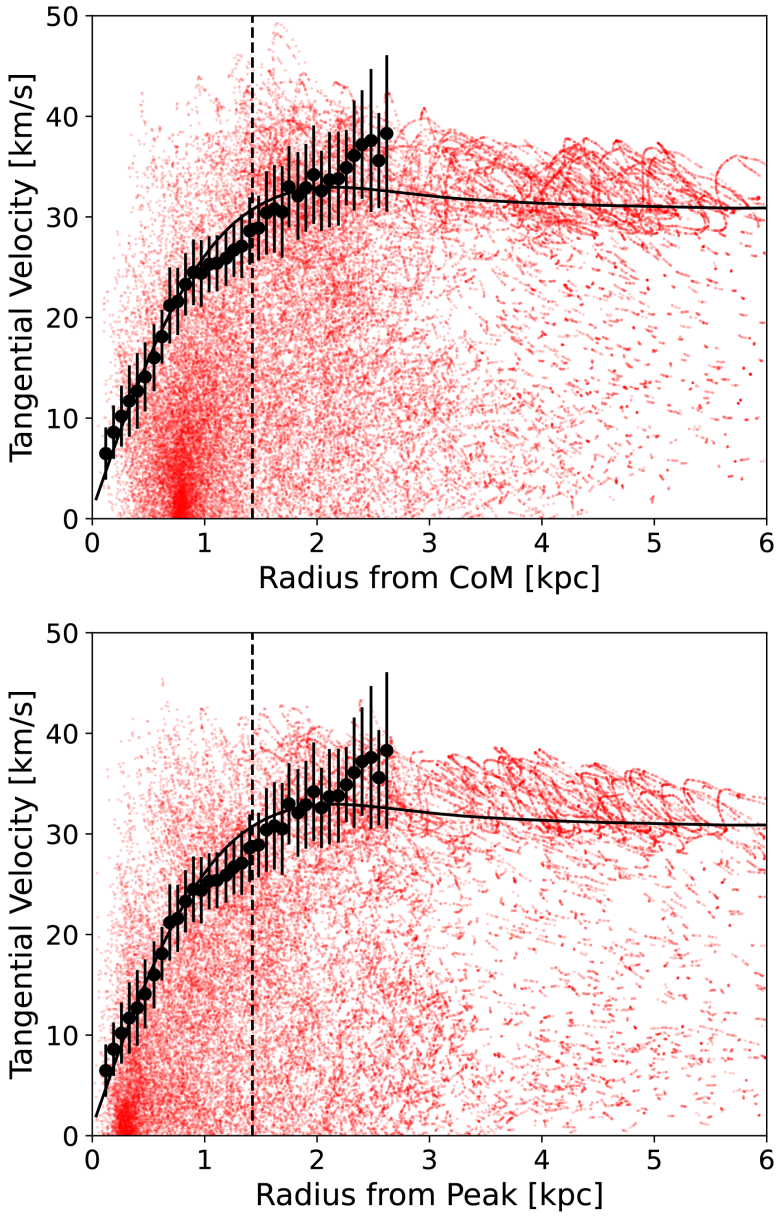

Figure 6.4: (Red data points) A randomly selected sample of data points, and their corresponding tangential velocities. (Black line) The SG-NFW fit used as a guide for the initiation of the simulation for UGCA444, as in FIG. 5.12. (Black errorbars) The observational data for the galaxy UGCA444. The top plot shows the results of the simulation when the grid is centred on the centre of mass, while the bottom plot shows the results when the centring is on the peak density.

of the restoring force. In such cases, test particles will eventually orbit in all directions around the central point, due to the lack of a preferred plane. For galaxies that do possess discs, the next step in bringing simulation closer to reality would be to add an additional gravitational potential to recreate the effects of a disc, artificially enforcing a 'restoring force' on test particles ejected from the plane. This would likely prevent particles from developing a significantly precessed orbit, which implies the $z-$component of velocity will be smaller. In this case, a larger share of the total magnitude of a particles velocity will be found in the $v_\top$ component, and smaller variance will exist in the tangential velocity of particles. The end result would be a narrower dispersion in our FIG. 6.4.

Finally, let us discuss the difference between the two plots in FIG. 6.4. We have briefly mentioned that one may consider to recentre the grid on either the centre of mass (CoM) or on the peak density. Although they are within 3 grid points of each other, they provide a significant difference in the final result of the inner region. Where it might seem logical to prefer the CoM approach, we must consider that particles in the centre of the halo are most subject to the core, which is indeed centred on the peak density. While, as one departs to a larger radius, the difference in choosing CoM or the peak density as the origin becomes smaller and less impactful. Therefore, the results are very similar at larger radii. Particles near the peak of the core are likely to orbit the local centre of mass, which is closer to the peak density than the global centre of mass.

We map the trajectories in the $z = 0$ plane for chosen test particles at different intervals and plot these in FIG. 6.5, where we only consider the simulation centred on the peak density. The particles at smaller radii 'knot' around the core, while those at larger radii hold an approximately constant displacement in the $z = 0$ plane from the centre, though they do travel in the z direction after some time, exhibiting a precession in orbit.

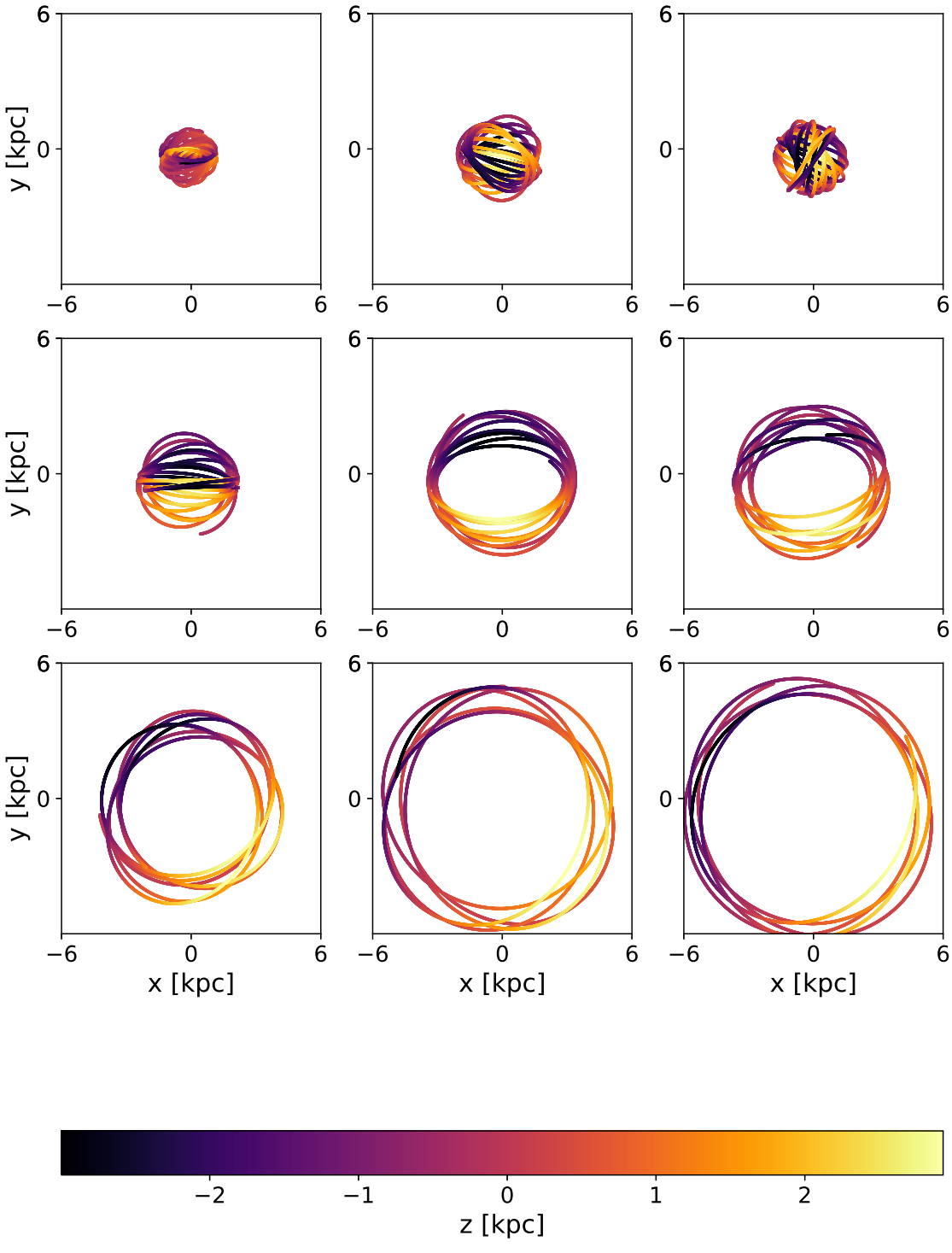

Figure 6.5: The trajectories of test particles at different radii. The z displacement is given by the colour of the particles. The particles at inner radii 'knot' over the core, while those at outer radii remain at an approximately constant radial distance on the xy plane.

6.6 Heating

We now briefly consider the effects of granules on the growth of the $z-$dispersion of the test particles, and note again that there is no restoring force owed to a planar disc in the system. In the absence of such a disc, we may still observe the effects of granules on the dispersion of test particles as they grow older. By tracking each test particle from its starting position and trajectory, we observe the $z-$component of its position, and trace it through time. We repeat this for all particles, and show the results in FIG. 6.6. It is clear that irrespective of the particle's location, it will undergo significant perturbation into a precessing orbit as it ages, leaving the $z = 0$ plane entirely. This data makes evident the fact that stars which form will inevitably be perturbed such that they have a larger $z-$component of velocity as they age. However, in the absence of a disc to provide restoring force, these particles do not return to the $z = 0$ plane. Additionally, the particles that migrate slowly into a precessed orbit are those found at the outer regions of the simulation, with the slowest orbital period. These test particles are subject to weaker perturbative forces due to the fact that the absolute magnitude of the density of the granules in their region is significantly smaller than that of the granules in the centre of the galaxy, surrounding the core.

One might hypothesise that in the presence of a disc, test particles would begin to oscillate about the $z = 0$ axis, while continuing on a general approximately circular orbit in the $z = 0$ plane. Statistically if one were to observe a large number of such particles in this case, they would find that older particles are dispersed at greater distances in the z direction than newer particles. Putting this into the context of stars, it becomes relevant to considering the age gradient of stars in disc galaxies such as the Milky Way [107]. Much work remains to be done on this topic, but these preliminary results hint at an interesting relationship which is due careful consideration. Suggestions of further work on the matter will follow the conclusion.

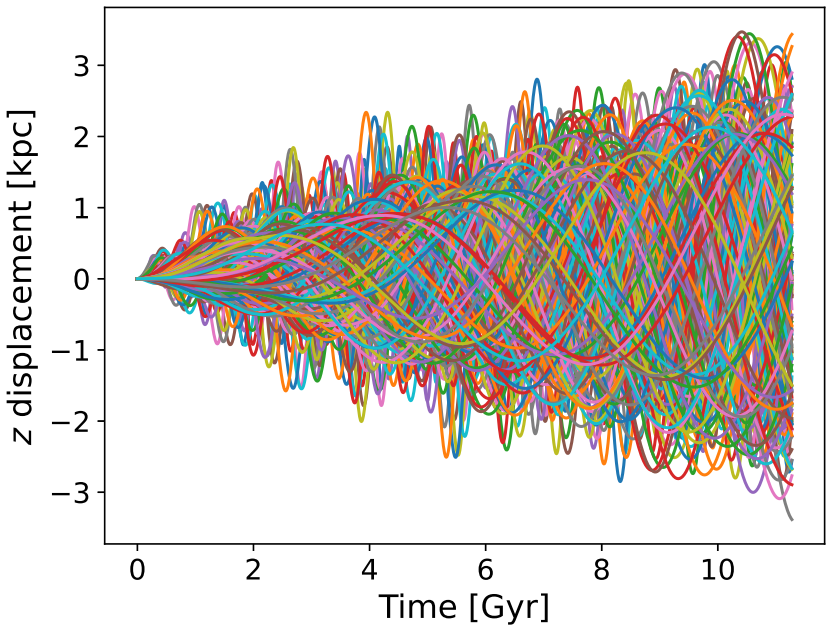

Figure 6.6: Each line traces the z coordinate a test particle takes across the length of the simulation. Particles migrate from the $z = 0$ plane into a precessed orbit as they age.

6.7 Interim Conclusion

In this chapter, we have analysed the dynamical features of isolated soliton cores and characterised these behaviours under variations of m and g. We then took a static 3D density field from our 3D simulation of UGCA444 from chapter 5, and observed the trajectories of propagated test particles at different radii. We studied the motion and velocity dispersion of these test particles on a preliminary level, reaffirming the necessity to perform a deeper and more careful statistical analysis on this data. Such analysis would include more rigorous statistical probing, such as sampling test particles according to the background density. We leave such notions for future work, but reiterate here that there is a wealth of information to be extracted from the analysis, both static and dynamic, of simulated FDM halos with observational signatures corresponding to those of astronomical observations, which we have presented systematically in the previous chapter, and preliminary in the latter half of the current chapter.

7

Conclusions and Future Work

7.1 Conclusion

In this thesis, we have discussed the Fuzzy Dark Matter (FDM) model as an explanation for the missing mass problem in observed galaxies, highlighting where FDM possesses strengths over the current leading cold dark matter model. Starting from defining the Gross-Pitaevskii-Poisson Equation (GPPE), we explain ways in which we can both analytically and numerically investigate the systems that form under the influence of gravity for ultralight bosons in the mass range of 10^{-22} eV/c^2 $-$ 10^{-20} eV/c^2, with the addition of repulsive boson-boson self interactions.

Operating under the assumptions that a FDM core-halo structure consists of a partially populated ground state (the soliton core) and a superposition of many excited states (the halo), in chapter 3, we initially turned focus to finding a way in which to accurately describe the core and its shape under the variation of fundamental parameters m and g. We firstly provided a generalised ansatz [Eq. (3.1)] which depends on the soliton parameters, ρ_0 and r_c, and the fundamental dimensionless self interaction parameter $\Gamma_g(g, m)$. Using this ansatz, we derived general forms of the time independent energy components for the soliton under the hypothesis that the ground state is static. By way of these components and the self-interacting virial relation in Eq. (3.22), we arrived at a relationship for the core radius under the influence of self interactions [Eq. (3.41], as seen in [2]. We then presented several other known profiles

used widely in the academic community to describe soliton cores, both non-interacting [23] and interacting [2], and discussed how these profiles do not have the implicit dependence on Γ_g. We discussed the relevance of this, stating that this parameter moderates the dimensionless shape of the soliton, manifesting in the extension of the flat inner part of the core and the sharper gradient drop in the core's tail as one increases the self interaction strength, tuning the profile into one that approaches the well known Thomas-Fermi profile. We analytically computed the values of these shape parameters for both the non-interacting empirical and Thomas-Fermi profiles. This allowed us to form an envelope for the functions r_c, ρ_0 (and later f), where we showed that numerical results for these parameters first agreed with the non-interacting limit of the envelope, and then transitioned towards the Thomas-Fermi limit of the envelope with an increase in Γ_g. However, this still did not provide us with accurate results for the soliton parameters in the moderately interacting regime. To provide a temporary 'patch' for this, we bestowed a Γ_g dependence on the shape parameters, (η, ν, σ, ζ, alpha), for the empirical profile [Eq. (3.35)] from [23]. These shape parameters are the solutions to the dimensionless integrals for the mass, the energy components, and the moment of inertia. We termed this the modified empirical profile. This allowed for more accurate computations of the soliton peak density, radius (and later frequency).

Using our modified shape parameters and our new dimensionless self-interacting parameter Γ_g, we uncovered a degeneracy under which soliton parameters ρ_0 and r_c are left invariant under changes in m and g along a contour curve.

The existence of the aforementioned degeneracy could have an impact on current constraints on the boson mass which are likely to change if the parameter space is extended to include g.[1] Indeed, various limitations have been placed upon the allowed range of the the boson mass by probing both cosmological scales *e.g.* [49, 91], as well as singular astronomical objects such as the star cluster orbiting the centre of Eridanus II [38, 43] or rotational curves and stellar kinematics [92, 93, 94, 65]. All these works, apart from [49], do not include a self-interaction and in some cases clear differences between theoretical fits and observational data were identified [94], while in others it was further evident that a single boson mass could not adequately fit theoretical curves to observational data [92, 65]. On the other hand, [3] reports that a non-zero value of the self-coupling, along with a single boson mass, can fit the rotation curves of the dark matter dominated galaxies in the SPARC database, providing for the first time positive support for FDM solitons with a non-zero value of the self-interaction from rotation curves. The degeneracies discussed here would be relevant for all the above studies which make inferences about the boson mass.[2] Clearly, all of the above are very preliminary

[1] Although the relative ranges of m and Γ exhibited in fig. 3.4 may imply that existing constraints on the boson mass will not be shifted by orders of magnitude, it is still the case that including the self-coupling may be relevant.

[2] In this work we discussed parameter degeneracies related to the compact FDM solitons. Similar degeneracies

observational investigations but provide strong motivation for precise, quantitative analysis of the model [76]. Steps have been taken to incorporate baryons into these models [72, 98], which would likely add an additional layer of complexity.

Although the agreement with numerics was indeed accurate, the dimensionless shape of the modified empirical profile was still invariant to changes in Γ_g, as the dependency was forced upon the shape parameters at a later stage. Motivated by this, we presented a new profile, the Super-Gaussian (SG) [Eq. (4.1)], which does in fact have this dependence. We expressed the limits of this profile, showing that in the limit of very strong self interactions, it too is unable to describe the sharp drop in outer core density, though it proves very promising in the range from non-interacting to strongly interacting systems.

In chapter 4, we built on these results and utilised a bimodal profile consisting of a marriage of the SG profile to the NFW profile to fit a selection of galaxies from the SPARC [1] dataset, assuming the absence of baryonic matter. This work was inspired by [3], which we expand by fitting only the core, and using the SG profile which is more accurate for the relevant g values. We first laid out two crucial conditions required to form physical SG-NFW profiles: the continuity condition requires the interface between the SG profile and the NFW profile, at transition radius r_t, to be continuous; the gradient condition requires the SG profile to have a steeper gradient than the NFW profile such that the SG profile is never artificially 'cut off'. The latter is important, as we state that the soliton core is the ground state around which excited states are superposed. Therefore, the ground state must be embedded in the NFW skirt. We made use of the degeneracy condition to expand our fits for the SPARC galaxies by extending them across the relevant contour curves in the $m-g$ parameter space, finding that a range of peak densities, corresponding to a range of soliton core masses, with different m and g values fit well to each galaxy. Each successful fit corresponded to a family of curves for different $m-g$ values along these contour lines. We utilised a Gaussian kernel density approximation, converting the m and g pairs which produced well-fitting curves into a dataset reflecting the density of allowed $m-g$ pairs in their parameter space, to find a range of acceptable values corresponding to our selection of galaxies from the SPARC catalog. That is to say, we suggested a two-dimensional $m-g$ space in which all pairs of m and g are likely to have the ability to form core-halo pairs whose velocity profiles accurately map to the chosen observational curves. By selecting the value of $m-g$ corresponding to the highest regional density of well-fit data points, we then performed a final iteration of our fit by fixing these parameters and increasing the resolution for the remaining parameters across which we search. The final output was a set of soliton-halo profiles which fit remarkably well across the chosen dataset, with the

can also exist on cosmological scales for FDM overdensity power spectra, see [96] which analyses a linearized hydrodynamical version of the hybrid condensate particle model of [96, 97].

exception of three galaxies, where the fits were not as good. However, even for these three, the magnitude of velocity and the approximate shape of the velocity curves was in agreement with the observational data. Such fits are likely to change under the consideration of baryonic matter, though we leave this for further investigation.

In chapter 5, we detailed our approach to simulating 3D FDM systems, discussing our initial condition set up. We first introduced a reference ground state energy, corresponding to the theoretical energy of a system if it was cooled to ground state. In such cases, a singular solitonic core forms in which the mass of the soliton is the total mass of the simulation. For our simulations, we allocated Gaussians randomly in a carefully chosen 3D box, computing the energy components. By generating a catalog of initial conditions, we were able to produce a set of results to analyse, noting the effects of the total system energy on the final distribution of mass between the core and the halo. We first identified that the radius of the core grows with an increase in mass, corresponding to the core's specific dimensionless self-interaction strength, Γ_g increasing with mass. This is a new result which is not found in previous analytical and empirical relationships between the core's total mass and radius. We were then able to form a simple and fascinating conclusion, suggesting that the ratio of core mass to total mass of the system was equal to the cube root of the ratio of the total energy of the system and its reference ground state energy. This still requires careful testing across a wide range of m and g to verify the consistency and range of our results. We then qualitatively analysed the effects of a change in energy on the size and number of granules in the halo, finding that as energy decreased and the system approached the ground state, the number of granules increased while their size decreased significantly. This is in contrast to typical statements in literature which suggest that the granules follow the size of the soliton core. Finally, we presented a novel simulation in which we recreated the approximate density profile of a SG-NFW fit, guided by the best fitting results from chapter 4 for the galaxy UGCA444. Our simulation demonstrated stability for ~ 1 Gyr, in which the computed 1D velocity profile sat within the error bars of the observational data. We therefore demonstrated here that the SG-NFW profiles are indeed stable and can be recreated via full 3D numerical simulations of the GPPE system, and also that the velocity curve data from observations can be recreated with such numerical simulations with stability on a relevant timescale. This opens the doors to conducting analysis on simulated halos with correspondence to observational galaxies in search of signatures one might hope to find via observation.

Finally, in chapter 6, we investigated the dynamical properties of the core and halo, as well as the effects of granules on the dynamics of test particles orbiting within the host halo. We laid the groundwork by identifying that the core exhibits an isotropic radial oscillation when excited, following the work in [2]. We then analysed the core oscillation frequency in the non-interacting case by comparing non-interacting analytical expectations to true oscillations from

spherically symmetric 1D simulations of perturbed non-interacting cores, finding that the soliton shape parameters play a key role in analytically predicting the correct frequency of oscillation. These results were extended to cover the repulsively self-interacting regime, confirming the analytically predicted form of the frequency, with the addition of correction terms in the shape parameters owing to a bestowed dependence on Γ_g, as in chapter. 3.

We then discussed the condensation effect found in 3D simulated core-halo systems, in which the core exhibits a growth in mass on time scales longer than the age of the universe. We analysed the dynamical evolution of the mass, finding that the core contracts while the halo expands. This self-cooling effect of the inner halo is confirmed by the migration of mass from the central area of the computational box towards the corners, with high energy particles wishing to maximise their distance from the core. This result corresponds to similar findings in [69, 75]. We discuss implications of this effect on the evolving velocity profiles of FDM halos, and tensions that may form with observational data.

We then demonstrated a simulated system in which we randomly placed test particles on a static FDM halo background of the system corresponding to the galaxy UGCA444, giving them an initial tangential velocity equal to the velocity computed from the 1D rotational curve of the corresponding 3D simulation snapshot. We tracked these particles and formed a preliminary statistical analysis on the distribution of tangential velocities of such test particles as they migrate between radial shells and are perturbed by the granular structure of the halo. We found that the velocity dispersion of these test particles was significantly wider than the error bars of the UGCA444 galaxy dataset. We discussed in detail the limitations of our simulation and the extent to which these findings may inform and inspire future work. We also discussed the emergence of precession in the test particle orbits, with them beginning on the $z = 0$ plane, and then migrating away from it.

This result led us to investigate the $z-$dispersion of test particles and how it evolves with time. We find that as test particles grow older, they are perturbed further by granules into a larger $z-$directional orbital path. We discuss that the implication of this may be strongly related to the age-gradient of stars in disc galaxies, where older stars are statistically found to be at a greater distance from the preferred galactic plane.

7.2 Prospects for Future Work

The aforementioned results leave many doors open for the prospect of future analysis, with much ground work laid here to guide and encourage the attempt at reconciliation of theoretical self interacting FDM to observational data and results. Here, we present several examples of possible avenues for future work.

In chapter 4, we demonstrated that the new SG-NFW bimodal profile can fit well to the selected galaxies from the SPARC [1] catalog, assuming absolute absence of baryonic matter. It thus follows that a logical next step would be to include baryonic components from the SPARC dataset for these galaxies, and to amend the results accordingly. Following this, an extension to the greater SPARC database, and an additional inclusion of other large scale surveys such as LITTLE THINGS [108, 109, 110] to see how the model fares. Conducting the investigation for a much larger data set of galactic rotational curves will hint at a more accurate m and g pairing, which in turn will demonstrate to what extent self interacting FDM can, or cannot, describe a statistically significant number of observed galaxies.

It thus follows that the recreation of UGCA444, presented in chapter 5, would benefit from being repeated with a larger grid and higher resolution with greater computational resources. It would therefore be important to secure access to a national supercomputer in order to conduct the simulations at the size, scale and resolution necessary to recreate galaxies of higher mass, while also further investigating the effects of different computational box sizes on the final formation. These results would shed light on the stability of FDM galaxy formations, demonstrating the duration for which the velocity curves from simulated data sit within, and agree with, the observational error bars for a much larger sample of galaxies. Related to the previous point, the results given in chapter 6 imply that a condensation mechanism results in consistent growth of the core on long timescales, which will likely play a significant effect on the stability of all profiles. Therefore, it is important to characterise such a growth formally and to investigate the implications of such a behaviour on the evolution of galactic FDM halos under real cosmological conditions.

Further expanding on the 3D simulations of chapter 5, another possible avenue of future work would involve generating a randomised catalog of soliton core formations, with randomisation of the total system mass, the total system energy, the boson mass and the self interaction strength, and the computational box size. This would lend credence to a universal result for the core-halo mass relation found in this chapter. We anticipate that results which are not significantly affected by the boundary conditions of the computational box will align well with the data, due to these parameters being scaled out of the relationship, though a much larger survey of results is required to give confidence to such a statement.

Most urgent of potential further work is a deeper and more statistically rigorous investigation of test particle trajectories in FDM halo backgrounds. This would enable us to verify the internal self consistency of our results, while also shedding further light on the unique signatures of FDM halos and their impact on astronomical observables. Our tentative results provide a good framework for future work in this direction, suggesting that with both the addition of more time and a deeper statistical model of the situation, many interesting results may be

uncovered.

Additionally, a simulation of a coupled system of self interacting FDM background and hydrodynamical baryonic simulations would allow for a deeper understanding of the effects of granules on the velocities of gas and stars in galaxies, building on the work in the latter half of chapter 6. Producing disc galaxies and elliptical galaxies, such simulations may point to important behaviours associated only with the granular nature of FDM, which is otherwise absent in CDM. An investigation into the age gradient of stars in simulated disc galaxies may shed light on the equivalent signature we see in the Milky Way [107], while an analysis of the velocity dispersion of simulated gas–fuelled by granule perturbations, which are a key aspect of the FDM paradigm–may inform us of a possible universal validity of the FDM model.

With the tools acquired to recreate observable galaxies, it would be interesting to attempt to reconcile other observational signatures, such as gravitational lensing, with those from simulated halos. A computation of the lensing effect of simulated halos, and the level of its agreement with observation, will point towards a direction either in favour of, or not in favour of, FDM.

Finally, the combination of FDM and CDM has been recently put forward in [96, 97, 111], and it would be interesting to revisit the studied features and galaxy reconstruction in such a setting, which lends itself directly to probing the condensate fraction for any given galaxy or cluster of galaxies.

It is clear that a still yet largely untapped wealth of opportunity for future research is present within this topic, and that FDM has many more years of careful investigation and analysis on behalf of the academic community ahead of it. We hope the work presented in this thesis–and all resulting publications, present and future–will both contribute to the understanding of this novel topic, while also laying the groundwork for deeper and more insightful future investigations.

References

[1] Lelli F, McGaugh S S and Schombert J M 2016 *The Astronomical Journal* **152** 157 xi, 3, 6, 7, 8, 44, 47, 52, 113, 116

[2] Chavanis P H 2011 *Physical Review D* **84** 043531 xii, xxi, 4, 5, 6, 7, 8, 13, 20, 21, 26, 27, 28, 29, 31, 32, 76, 91, 92, 93, 94, 95, 111, 112, 114

[3] Delgado V and Muñoz Mateo A 2022 *Monthly Notices of the Royal Astronomical Society* **518** 4064–4072 xv, 5, 6, 7, 41, 43, 44, 52, 61, 62, 112, 113

[4] Hubble E and Humason M L 1931 *The Astrophysical Journal* **74** 43 1

[5] Zwicky F 1933 *Helvetica Physica Acta* **6** 110–127 1

[6] Clausius R 1870 *The London, Edinburgh, and Dublin Philosophical Magazine and Journal of Science* **40** 122–127 (*Preprint* https://doi.org/10.1080/14786447008640370) 1

[7] Rubin V C and Ford W K 1970 *The Astrophysical Journal* **159** 379 1

[8] Freeman K C 1970 *The Astrophysical Journal* **160** 811 1

[9] Rogstad D H and Shostak G S 1972 *The Astrophysical Journal* **176** 315–321 1

[10] Jungman G, Kamionkowski M and Griest K 1996 *Physics Reports* **267** 195–373 2

[11] Hannestad S, Mirizzi A, Raffelt G G and Wong Y Y 2010 *Journal of Cosmology and Astroparticle Physics* **2010** 001 2

[12] Peebles P J E 1982 *The Astrophysical Journal Letters* **263** L1–L5 2

[13] Bond J R, Szalay A S and Turner M S 1982 *Phys. Rev. Lett.* **48**(23) 1636–1639 2

[14] Blumenthal G R, Pagels H and Primack J R 1982 *Nature* **299** 37–38 2

[15] Blumenthal G R, Faber S M, Primack J R and Rees M J 1984 *Nature* **311** 517–525 2

[16] Weinberg D H, Bullock J S, Governato F, Kuzio de Naray R and Peter A H G 2015 *Proceedings of the National Academy of Science* **112** 12249–12255 2, 4

[17] Bullock J S and Boylan-Kolchin M 2017 *Annual Review of Astronomy and Astrophysics* **55** 343–387 2, 4

[18] Del Popolo A and Le Delliou M 2017 *Galaxies* **5** 17 2, 4

[19] Macciò A V, Paduroiu S, Anderhalden D, Schneider A and Moore B 2012 *Monthly Notices of the Royal Astronomical Society* **424** 1105–1112 2, 4

[20] Navarro J F, Frenk C S and White S D M 1996 *The Astrophysical Journal Letters* **462** 563 (*Preprint* astro-ph/9508025) 2, 43, 50

[21] Del Popolo A and Pace F 2016 *Astrophysics and Space Science* **361** 162 3

[22] Hu W, Barkana R and Gruzinov A 2000 *Physical Review Letters* **85** 1158–1161 3

[23] Schive H Y, Chiueh T and Broadhurst T 2014 *Nature Physics* **10** 496–499 4, 6, 7, 19, 27, 29, 30, 43, 112

[24] Mocz P, Vogelsberger M, Robles V H, Zavala J, Boylan-Kolchin M, Fialkov A and Hernquist L 2017 *Monthly Notices of the Royal Astronomical Society* **471** 4559–4570 4, 6, 17

[25] May S and Springel V 2021 *Monthly Notices of the Royal Astronomical Society* **506** 2603–2618 4, 57

[26] Mocz P, Fialkov A, Vogelsberger M, Becerra F, Amin M A, Bose S, Boylan-Kolchin M, Chavanis P H, Hernquist L, Lancaster L, Marinacci F, Robles V H and Zavala J 2019 *Physical Review Letters* **123** 141301 4

[27] Mocz P, Fialkov A, Vogelsberger M, Becerra F, Shen X, Robles V H, Amin M A, Zavala J, Boylan-Kolchin M, Bose S, Marinacci F, Chavanis P H, Lancaster L and Hernquist L 2020 *Monthly Notices of the Royal Astronomical Society* **494** 2027–2044 4, 17

[28] Banerjee S, Bera S and Mota D F 2020 *Journal of Cosmology and Astroparticle Physics* **2020** 034 4

[29] Mina M, Mota D F and Winther H A 2022 *Astronomy & Astrophysics* **662** A29 4

[30] Rindler-Daller T and Shapiro P R 2014 *Modern Physics Letters A* **29** 4, 27

[31] Amruth A, Broadhurst T, Lim J, Oguri M, Smoot G F, Diego J M, Leung E, Emami R, Li J, Chiueh T, Schive H Y, Yeung M C H and Li S K 2023 *Nature Astronomy* 1–12 4

[32] Marsh D J E 2016 *Physics Reports* **643** 1–79 4

[33] Hui L 2021 *Annual Review of Astronomy and Astrophysics* **59** 247–289 4

[34] Ferreira E G M 2021 *The Astronomy and Astrophysics Review* **29** 7 4

[35] Li X, Hui L and Yavetz T D 2021 *Physical Review D* **103** 023508 4, 27

[36] Hui L 2021 *Annual Review of Astronomy and Astrophysics* **59** 247–289 4

[37] Woo T P and Chiueh T 2009 *The Astrophysical Journal* **697** 850 4

[38] Marsh D J and Niemeyer J C 2019 *Physical Review Letters* **123** 051103 4, 7, 27, 40, 91, 112

[39] Veltmaat J, Niemeyer J C and Schwabe B 2018 *Physical Review D* **98** 043509 4, 8, 94

[40] Glennon N and Prescod-Weinstein C 2021 *Physical Review D* **104** 083532 4

[41] Chavanis P H and Delfini L 2011 *Physical Review D* **84** 043532 4, 5, 16

[42] Church B V, Mocz P and Ostriker J P 2019 *Monthly Notices of the Royal Astronomical Society* **485** 2861–2876 4

[43] Chiang B T, Schive H Y and Chiueh T 2021 *Physical Review D* **103** 103019 4, 6, 7, 8, 27, 40, 91, 94, 112

[44] Schive H Y, Liao M H, Woo T P, Wong S K, Chiueh T, Broadhurst T and Hwang W Y 2014 *Physical Review Letters* **113** 261302 4, 8, 27, 30

[45] Amorisco N C and Loeb A 2016 *Monthly Notices of the Royal Astronomical Society: Letters* **459** L51–L55 4

[46] Rindler-Daller T and Shapiro P R 2012 *Monthly Notices of the Royal Astronomical Society* **422** 135–161 5

[47] Li B, Rindler-Daller T and Shapiro P R 2014 *Physical Review D - Particles, Fields, Gravitation and Cosmology* **89** 083536 5

[48] Li B, Shapiro P R and Rindler-Daller T 2017 *Physical Review D* **96** 063505 5

[49] Desjacques V, Kehagias A and Riotto A 2018 *Physical Review D* **97** 023529 5, 40, 41, 112

[50] Chavanis P H 2021 *Physical Review D* **103** 123551 5, 6, 20, 30, 37, 92, 94

[51] Hartman S T, Winther H A and Mota D F 2022 *Journal of Cosmology and Astroparticle Physics* **2022** 005 5

[52] Hartman S T H, Winther H A and Mota D F 2022 *Astronomy & Astrophysics* **666** A95 5

[53] Mocz P, Fialkov A, Vogelsberger M, Boylan-Kolchin M, Chavanis P H, Amin M A, Bose S, Dome T, Hernquist L, Lancaster L, Notis M, Painter C, Robles V H and Zavala J 2023 *Monthly Notices of the Royal Astronomical Society* **521** 2608–2615 5

[54] Chakrabarti S, Dave B, Dutta K and Goswami G 2022 *Journal of Cosmology and Astroparticle Physics* **2022** 074 5

[55] Dave B and Goswami G 2023 *Journal of Cosmology and Astroparticle Physics* **2023** 015 5

[56] Dawoodbhoy T, Shapiro P R and Rindler-Daller T 2021 *Monthly Notices of the Royal Astronomical Society* **506** 2418–2444 5

[57] Shapiro P R, Dawoodbhoy T and Rindler-Daller T 2021 *Monthly Notices of the Royal Astronomical Society* **509** 145–173 5

[58] Rindler-Daller T 2023 *Frontiers in Astronomy and Space Sciences* **10** 142 5, 6, 20

[59] Chavanis P H 2020 *Universe* **6** 226 5

[60] Chavanis P H 2016 *Physical Review D* **94** 083007 5

[61] Moss I G 2024 (*Preprint* 2407.13243) 5

[62] Meinert J and Hofmann R 2021 *Universe* **7** 5

[63] Bañares Hernández A, Castillo A, Martin Camalich J and Iorio G 2023 *Astron. Astrophys.* **676** A63 (*Preprint* 2304.05793) 5, 8, 43

[64] Bañares Hernández A, Castillo A, Martin Camalich J and Iorio G 2023 *Astron. Astrophys.* **676** A63 (*Preprint* 2304.05793) 5, 8, 43

[65] Khelashvili M, Rudakovskyi A and Hossenfelder S 2023 *Monthly Notices of the Royal Astronomical Society* **523** 3393–3405 5, 40, 41, 43, 63, 112

[66] Chan J H H, Schive H Y, Woo T P and Chiueh T 2018 *Monthly Notices of the Royal Astronomical Society* **478** 2686–2699 6

[67] Minguzzi A, Succi S, Toschi F, Tosi M and Vignolo P 2004 *Physics Reports* **395** 223–355 7

[68] Dmitriev A S, Levkov D G, Panin A G, Pushnaya E K and Tkachev I I 2021 *Physical Review D* **104** 023504 7

[69] Álvarez-Rios I, Bernal T, Chavanis P H and Guzmán F S 2024 *Physical Review D* **110**(6) 063502 8, 9, 65, 71, 99, 115

[70] Guzmán F S 2019 *Physical Review D* **99** 083513 8, 94

[71] Schive H Y, Chiueh T and Broadhurst T 2020 *Physical Review Letters* **124** 201301 8, 94

[72] Veltmaat J, Schwabe B and Niemeyer J C 2020 *Physical Review D* **101** 083518 8, 27, 41, 94, 113

[73] Chowdhury D D, Bosch F C v d, Robles V H, Dokkum P v, Schive H Y, Chiueh T and Broadhurst T 2021 *The Astrophysical Journal* **916** 27 8, 27, 94

[74] Chowdhury D D, van den Bosch F C, van Dokkum P, Robles V H, Schive H Y and Chiueh T 2023 *The Astrophysical Journal* **949** 68 9, 91

[75] Lin S C, Schive H Y, Wong S K and Chiueh T 2018 *Physical Review D* **97**(10) 103523 9, 67, 71, 115

[76] Indjin M, Liu I K, Proukakis N P and Rigopoulos G 2024 *Physical Review D* **109**(10) 103518 9, 41, 113

[77] Indjin M, Liu I k G, Proukakis N P and Rigopoulos G 2024 *In preparation* 9

[78] Indjin M, Liu I k G, Proukakis N P and Rigopoulos G 2024 *In preparation* 10, 28

[79] Kiessling M K H 2003 *Advances in Applied Mathematics.* **31** 132–149 (*Preprint* astro-ph/9910247) 13

[80] Liu I K, Proukakis N P and Rigopoulos G 2023 *Monthly Notices of the Royal Astronomical Society* **521** 3625–3647 13, 27, 74

[81] Membrado M, Pacheco A F and Sañudo J 1989 *Physical Review A* **39** 4207 14

[82] Guzman F S and Urena-Lopez L A 2006 *The Astrophysical Journal* **645** 814–819 (*Preprint* astro-ph/0603613) 16

[83] Schwabe B, Niemeyer J C and Engels J F 2016 *Physical Review D* **94**(4) 043513 17

[84] Zagorac J L, Sands I, Padmanabhan N and Easther R 2022 *Physical Review D* **105**(10) 103506 27, 67

[85] Lee J w and Koh I g 1996 *Physical Review D* **53** 2236 28

[86] Goodman J 2000 *New Astronomy* **5** 103–107 28

[87] Arbey A, Lesgourgues J and Salati P 2003 *Physical Review D* **68** 023511 28

[88] Böhmer C G and Harko T 2007 *Journal of Cosmology and Astroparticle Physics* **2007** 025 28

[89] Chen J, Du X, Lentz E W, Marsh D J and Niemeyer J C 2021 *Physical Review D* **104** 1–15 28, 99

[90] Chavanis P H 2019 *Physical Review D* **100**(12) 123506 37

[91] Rogers K K and Peiris H V 2021 *Physical Review Letters.* **126** 071302 40, 112

[92] Bar N, Blas D, Blum K and Sibiryakov S 2018 *Physical Review D* **98**(8) 083027 40, 41, 74, 112

[93] Maleki A, Baghram S and Rahvar S 2020 *Physical Review D* **101**(10) 103504 40, 112

[94] Bañares-Hernández, Andrés, Castillo, Andrés, Martin Camalich, Jorge and Iorio, Giuliano 2023 *Astronomy & Astrophysics* **676** A63 40, 41, 112

[95] Álvarez Rios I and Guzmán F S 2022 *Monthly Notices of the Royal Astronomical Society* **518** 3838–3849 40

[96] Proukakis N P, Rigopoulos G and Soto A 2024 *Physical Review D* **110**(2) 023504 41, 113, 117

[97] Proukakis N P, Rigopoulos G and Soto A 2023 *Physical Review D* **108** 083513 (*Preprint* 2303.02049) 41, 113, 117

[98] Álvarez Rios I and Guzmán F S 2023 *Physics Letters B* **843** 137984 41, 113

[99] Chan H Y J, Ferreira E G M, May S, Hayashi K and Chiba M 2022 *Monthly Notices of the Royal Astronomical Society* **511** 943–952 57

[100] Taruya A and Saga S 2022 *Physical Review D* **106**(10) 103532 57

[101] Kawai H, Kamada A, Kamada K and Yoshida N 2024 *Physical Review D* **110**(2) 023519 57

[102] Barnes D G and de Blok W J G 2001 **122** 825–829 (*Preprint* astro-ph/0107474) 63

[103] Kamphuis P, Peletier R F, van der Kruit P C and Heald G H 2011 *Monthly Notices of the Royal Astronomical Society* **414** 3444–3457 (*Preprint* https://academic.oup.com/mnras/article-pdf/414/4/3444/18712856/mnras0414-3444.pdf) 63

[104] Álvarez-Rios I, Guzmán F S and Shapiro P R 2023 *Physical Review D* **107**(12) 123524 65

[105] Levkov D G, Panin A G and Tkachev I I 2018 *Physical Review Letters* **121** 99

[106] Eggemeier B and Niemeyer J C 2019 *Physical Review D* **100**(6) 063528 99

[107] Casagrande L, Silva Aguirre V, Schlesinger K J, Stello D, Huber D, Serenelli A M, Schönrich R, Cassisi S, Pietrinferni A, Hodgkin S, Milone A P, Feltzing S and Asplund M 2015 *Monthly Notices of the Royal Astronomical Society* **455** 987–1007 (*Preprint* https://academic.oup.com/mnras/article-pdf/455/1/987/3081353/stv2320.pdf) 108, 117

[108] Walter F, Brinks E, de Blok W J G, Bigiel F, Kennicutt R C, Thornley M D and Leroy A 2008 *The Astronomical Journal* **136** 2563 116

[109] de Blok W J G, Walter F, Brinks E, Trachternach C, Oh S H and Kennicutt R C 2008 *The Astronomical Journal* **136** 2648 116

[110] Oh S H, de Blok W J G, Walter F, Brinks E and Kennicutt R C 2008 *The Astronomical Journal* **136** 2761 116

[111] Proukakis N P, Rigopoulos G and Soto A 2024 (*Preprint* 2407.08860) 117